SAND2007-7683P

Precision Electron Flow Measurements in a Disk Transmission Line

by

Jeremy Paul Martin

B.S, University of Missouri-Columbia, 2000
M.S, University of Missouri-Columbia, 2002

DISSERTATION

Submitted in Partial Fulfillment of the
Requirements for the Degree of

Doctor of Philosophy
Engineering

The University of New Mexico

Albuquerque, New Mexico

December, 2007

Acknowledgments

The work for this dissertation was conducted at Sandia National Laboratories[1].

[1]Sandia is a multiprogram laboratory operated by Sandia Corporation, a Lockheed Martin Company, for the United States Department of Energy's National Nuclear Security Administration under contract DE-AC04-94AL85000.

Precision Electron Flow Measurements in a Disk Transmission Line

by

Jeremy Paul Martin

ABSTRACT OF DISSERTATION

Submitted in Partial Fulfillment of the
Requirements for the Degree of

Doctor of Philosophy
Engineering

The University of New Mexico

Albuquerque, New Mexico

December, 2007

Contents

List of Figures

List of Tables

Chapter 1

Introduction

The efficient transport of significant electrical power densities originating from large pulsed-power drivers is a critical requirement in operating high power particle accelerators and intense radiation sources. Typically, these devices must operate in vacuum, while the initial pulse is developed externally within transformer oil and de-ionized water sections. As a result, an insulating interface is essential in separating the vacuum transmission line, directly feeding the load, from that of the liquid dielectric section of line emanating from the pulse generator. The vacuum section of line is thus contained between the insulator stack and the load as illustrated in figure 1.1. The electric field generated between the conductors of the transmission line in these applications can easily approach field strengths on the order of 20-100 MV/m, which greatly reduces the effectiveness of material insulation. Although the cathode in a vacuum line will freely emit electrons when subjected to such electric stress, the self-magnetic field of the transmission line current is capable of inhibiting the electrons from reaching the anode within the duration of the power pulse under appropriate conditions. This device, known as a magnetically insulated transmission line (MITL), is crucial for the efficient delivery of high power densities in excess of 10^{14} W/m^2 [2].

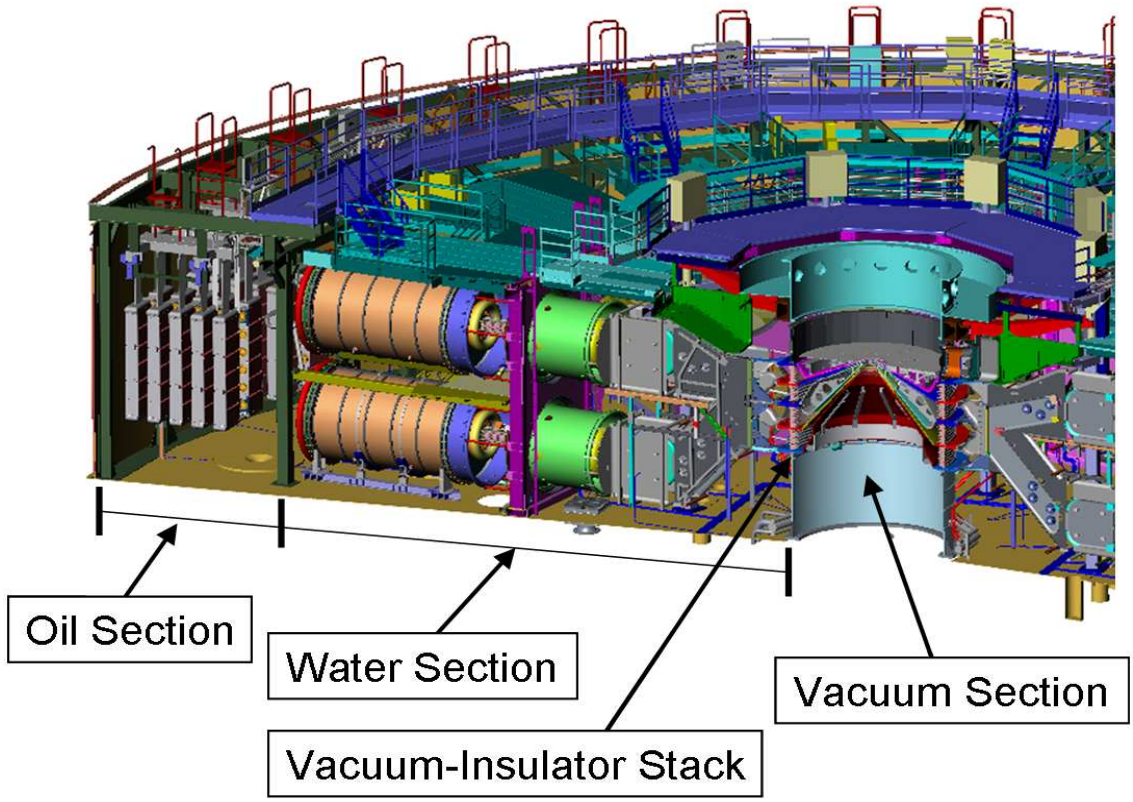

Figure 1.1: The ZR accelerator located at Sandia National Laboratories. It utilizes four conical MITLs to channel the pulsed power distributed between its ? modules into a z-pinch load which is located at the epicenter of the vacuum section.

For a large enough power pulse being transferred to the load, the associated electrical field strength across the gap of the transmission line will initiate a plasma which covers the negatively charged electrode. This surface plasma provides a source of electron emission with virtually no electric field present at the cathode, which is characteristic of a space-charge-limited-emitter [3]. Efficiency of the line is reduced when electrons emitted from the cathode are capable of streaming to the anode, shunting the transmission line. The MITL's ability to provide an insulated path for the energy flow stems from the interaction between the magnetic flux density, produced by the current pulse, and the electrons which are accelerated across the

gap due to the electric field[1]. During this period of insulation, the vast majority of the electrons are unable to reach the anode and are held in a close trajectory along the cathode allowing for TEM wave propagation. Because the electron pressure is much less than the electric field pressure [4], the electrons experience an average velocity that is dominated by an $\vec{E} \times \vec{B}$ drift. The orthogonality between the electric field and the magnetic flux density guides the electrons toward the load in the direction of power flow as shown in figure 1.2. The total current flowing in the anode, I_a, is thus divided in the return path between the current flowing in the cathode, I_c, and the current flowing in the vacuum electron flow, I_e. This electron flow creates a conducting channel, in the form of an electron sheath, which resides within the vacuum between the anode and cathode.

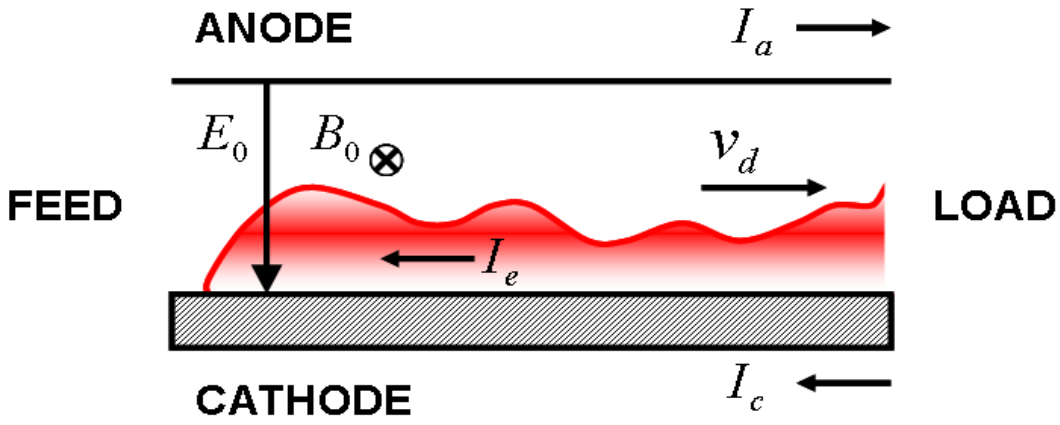

Figure 1.2: General parallel plate MITL structure. The crossed electric and magnetic fields result in a sheath of electrons along the cathode which possess an average drift velocity, v_d, in the direction of power flow, (i.e. toward the load). This collection of drifting electrons defines the electron flow present in the MITL.

[1]The physics of magnetic insulation will be discussed in greater detail in Chapter 2.

The gap spacing between the anode and cathode, A-K gap, of a MITL is an important design parameter which is constrained by the self-inductance of the line, energy deposition into the anode [5], and the expansion of the MITL-cathode-plasma [6, 7]. While the MITL's efficiency is directly related to its inductively stored energy, closure of the A-K gap due to energy deposition into the anode by field emitted electrons can result in a substantial loss of energy. Prior to magnetic insulation, field-emitted electrons from the cathode are free to transit the gap and heat the anode. Substantial electron energy deposition can occur near the load resulting in the formation of an anode plasma. The ions produced by this plasma tend to accelerate the closure of the A-K gap by means of an avalanche breakdown [**?**]. As a result, in an ideal system, the electron flow at the load is minimized while maintaining a low inductance as to not suffer a decrease in system efficiency. While this trade-off is difficult to realize in a transmission line of constant gap spacing, a tapered line or conical disk configuration allows for an inductive profile to be built directly into the geometry of the electrodes while limiting the concentration of the electron flow along the cathode. The characterization of the electron flow in low-impedance driven loads, utilizing radially decreasing gaps, is useful in the design of z-pinch driven high energy density physics experiments and is one of the key motivations for this work.

The methods and design criterion established for the construction of the MITLs used in previous z-pinch drivers at Sandia National Laboratories have always been of an empirical nature [8]. The gap profiles for these designs consist of three separate sections for merging the power flow of multiple lines into a single load. These sections consist of a "flared" portion of line which attaches to a vacuum insulator stack, an outer MITL which employees a radially decreasing gap, and an inner MITL of constant gap spacing, figure 1.3. The earliest designs, PROTO-II and SATURN, required that the radial section be of a constant impedance that contributed to the establishment of magnetic insulation at 2/3 of the peak current. Later designs, PBFA-Z and ZR, were designed to achieve a nearly constant loss of

vacuum flow throughout the upper 2/3 of the load current. This was accomplished through the adjustment of several computer simulated models which assumed that the electrons emitted from the cathode surface were not re-trapped and that the MITL experienced cathode-plasma-expansion at a rate of 2.5 μs/cm [1]. Under these assumptions the optimal profile of the electron current would be radially uniform, consistent with a zero re-trapping rate. Recent particle-in-cell (PIC) simulations of the PBFA-Z vacuum section, however, suggest that re-trapping of the electron flow near the MITL's post-hole convolute does exist and results in considerably less electron current than predicted from the original design [9].

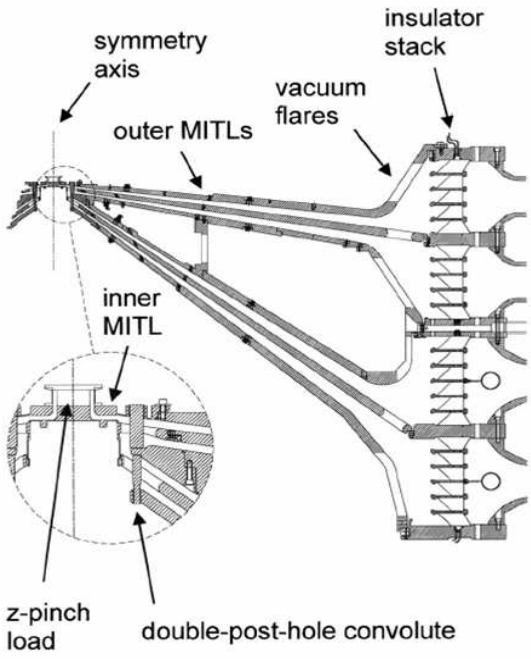

Figure 1.3: Vacuum section of PBFA-Z. [1].

The purpose of this dissertation is to develop and test a particularly ambitious design methodology centered round the geometrical encoding of non-zero re-trapping rates within radial MITL gaps. This will allow for the reduction of the electron flow near the load while lowering the line inductance with a decrease in the gap spacing. The re-trapping rate is defined by the fractional change in the radial electron flow; it is determined through the inductive profile of the gap and thus can be set by the curvature of the MITL's electrodes. PIC calculation, which have been very successful in predicting the electron flow within the vacuum section of the PBFA-Z and ZR accelerators [10, 11], will be used extensively in the investigation of this proposed model. High voltage PIC simulations, (i.e., $\geq$ 1 MV), wil determine the validity of the model while lower voltage tests will be verified through experiment. The self-insulated, low-impedance disk transmission line used in these experiments is shown in figure 1.4. The azimuthal cross-section for this design is illustrated in figure 1.5.

Figure 1.4: Disk MITL hardware.

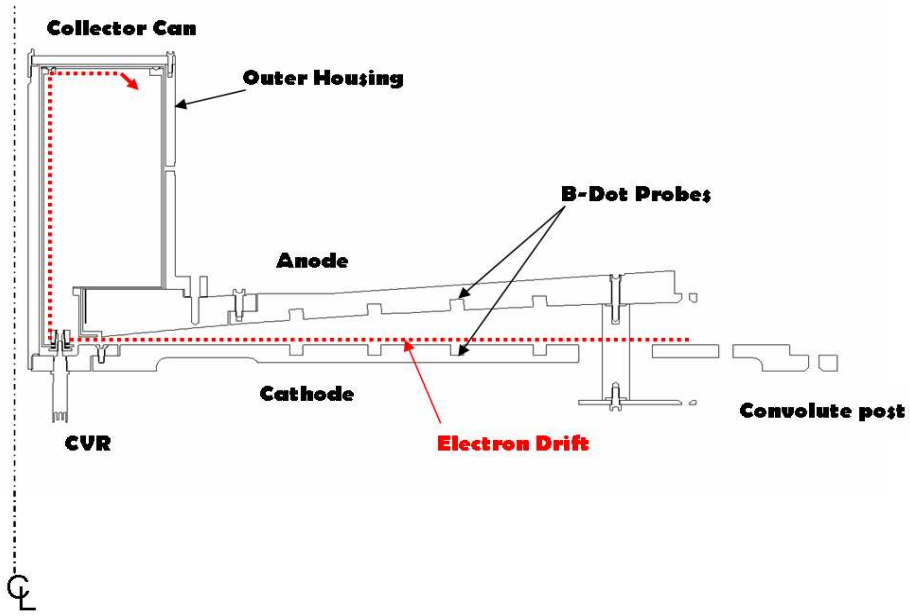

Figure 1.5: Azimuthal cross-section of radial disk MITL and load profile.

The electron flow will be monitored within the line through the subtraction of current monitor signals which are distributed along the anode and cathode as is typically done in practice. To facilitate in the resolution of strongly-insulated flows, which are often found in z-pinch drivers, an additional diagnostic has been developed [12], which will allow for the direct measurement of the electron current at the load. By dramatically expanding the gap size in the load region (collector can), the vacuum impedance of the load is increased, resulting in an instability in the electron flow [13]. Exploiting this turbulence allows for current viewing resistors (CVRs) to be placed through the cathode just inside the base of the collector can and directly measure the electron current, figure 1.5. This not only provides data with which to better gauge the validity of the computer simulated results, but provides an additional diagnostic to be directly implemented on large pulsed power drivers like ZR[2].

[2]Refurbished PBFA-Z, z-pinch driver, located at Sandia National Laboratories.

Initial experiments were conducted on an under-insulated system so that typical MITL diagnostics[3] could be used to supplement the data recorded by the CVRs in the load. Once the total current in the MITL was determined for a 10 kV reference signal, large signal B-dot probes were calibrated for several position varying radially outward to determine local current densities and potential locations for energy loss in the transmission line. The position of these diagnostics coincide with a portion of the several hundred local diagnostics placed throughout the simulation geometry for data comparison.

The remainder of this dissertation is outlined as follows: In chapter 2, an overview of the self-magnetic insulation process will be examined from the outset. To simplify matters, the physics of a single electron emitted into the transmission line gap will be considered, providing a clear picture of charged particle dynamics within perpendicular electric and magnetic fields. Extending the scope to many charged particles, a brief summary of popular analytical models will be given. The equations needed for our analysis will be developed using pressure balance theory and finally, the geometry of the experimental setup will be determined by studying the rate of change in electron flow and its effects on the impedance profile of the system. Chapter 3 will provide the details of the experimental setup for the lower voltage testing. This will include the MITL hardware, the diagnostics being used, as well as the pulse power driver. The PIC code simulation used in this experiment will be QUICKSILVER[4] and will be covered in chapter 4. The simulation results will be provided in chapter 5 and will compare several different re-trapping rates of the electron flow for high and low voltage pulses. The experimental results are covered in chapter 6 and provide a comparison with the low voltage simulations. Conclusions are drawn from the experimental and simulated results in chapter 7. Finally the text is rounded off by appendices covering some of the necessary derivations.

[3]These diagnostics will be discussed in further detail in Chapter 3.
[4]Developed at Sandia National Laboratories.

Chapter 2

Theory of Self-Magnetically Insulated Transmission Lines

Within a vacuum transmission line, explosive electron emission (EEE) from the cathode will initiate amid sufficiently large electric field strengths. It has been experimentally observed, that these electric field stresses result in the formation of a plasma layer along the cathode within a few nanoseconds, subsequently defining a space-charge-limited electron emitter [14]. The threshold for this electronic emission has been found to be material dependent and sensitive to the pulse width (FWHM) of the applied line voltage [?]. While plasma formation has been detected for field strengths below 100 kV/cm for velvet covered electrodes [15, 16], untreated metallic surfaces have been found to typically emit above 200 kV/cm [?].

The mechanism driving EEE is still not completely understood. At the field strengths mentioned above, it is clear that the potential barrier width of the cathode is diminished accounting for the introduction of electrons into the transmission line gap due to the quantum mechanical tunneling effect. In general, and in agreement with the Fowler-Norheim equation [17], the fields considered here are not substantial enough for this to account for the electron emission observed. It has been proposed, however, that this emission is capable of initiating a complex process resulting in the

local heating and vaporization of surrounding material due to local field enhancement and microscopic protrusions [18] along the cathode and dielectric inclusions [19] within its surface. This rapid ionization of localized surface material could lead to an explosive thermionic emission of electrons distributed along the cathode.

The dynamics of an electron after emission is strongly influenced by the perpendicular electric and magnetic fields present within the line due to the voltage waveform from the power pulse. Once electrons have been liberated from the cathode surface, they are driven across the anode-cathode gap due to the electric field. For sufficiently high current, electrons are turned away from reaching the anode surface and are said to be insulated. The average height of the insulated electrons' orbits define the boundary of the MITL's electron space charge. The electrons confined to this electronic sheath experience a net drift velocity in the direction of power flow due to the crossed fields. This average electron drift defines the MITL's electron flow current, which along with losses in the line, make up the measured difference between the anode and cathode currents.

2.1 Evolution of self-magnetic insulation

Generally, the evolution of self-magnetic insulation in an infinite length transmission line proceeds as follows [20]: Prior to electron emission, the MITL will only draw a vacuum displacement current from the power pulse, which is initially traveling at the speed of light through the vacuum medium. As the amplitude of the pulse rises appreciably, the cathode will begin freely emitting electrons. The electric field present between the anode and cathode (A-K gap) causes these electrons to "stream" toward the anode. If the electrons are capable of bridging the A-K gap to recombine with the anode, the transmission line is effectively shunted by the transverse electron flow, as shown in figure 2.1a. This conducting channel is referred to as the "loss front"

and propagates down the line at velocities much lower than the speed of light due to the inertia of the electrons crossing the gap [2]. The fraction of the pulse traveling ahead of the loss front is known as the precursor and continues propagating at the speed of light. The discrepancy between the velocities of the precursor and the main portion of the pulse, which is restrained by the loss front, results in a broadening of the power pulse over time as shown in figure 2.2.

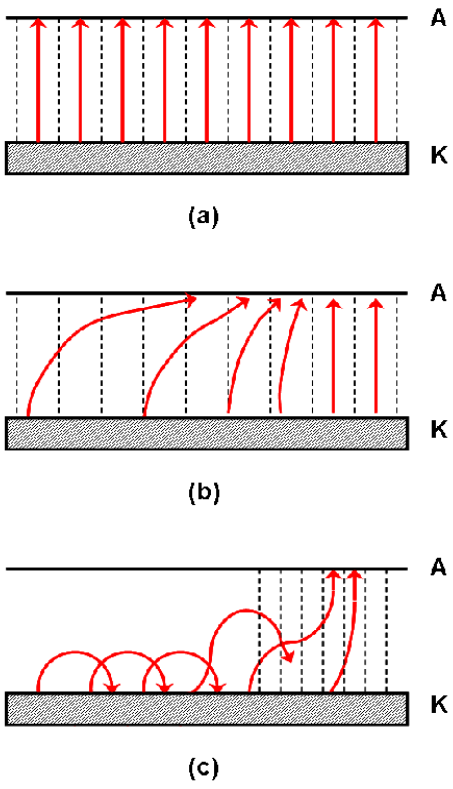

Figure 2.1: Evolution of self-magnetic insulation. Dashed lines represent displacement current while solid lines represent electron current.

As electrons are conducted through the loss front they increase the amount of current drawn by the MITL, subsequently strengthening the amount of magnetic flux density upstream of the loss front. When the current is large enough, the magnetic

force will start to deflect the electrons away from the anode and toward the direction of power flow, decreasing the width of the loss front as in figure 2.1b. As more loss current is conducted across the gap, larger sections of the line become insulated and the impedance of the line decreases until it reaches its self-limiting value, figure 2.1c, which is the operational vacuum impedance of the line due to the electron space charge [21].

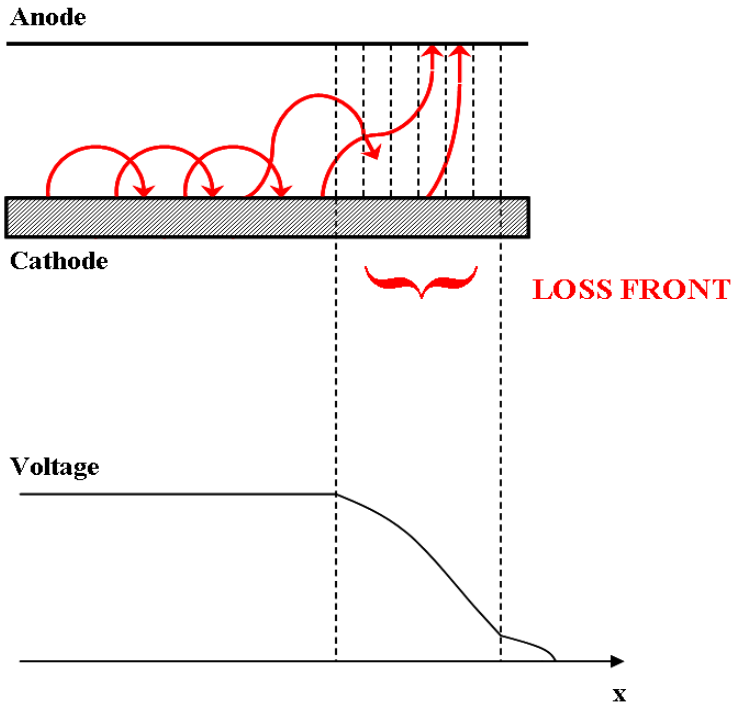

Figure 2.2: Pulse broadening at a time of significant magnetic insulation.

The current drawn by a finite length MITL will consist of the load current in addition to the current conducted through the loss front. Prior to the loss front reaching the load, insulated sections of the MITL operate at a self-limited impedance. Once the pulse has reached the load the MITL will continue to run at this impedance as long as the load impedance is sufficiently larger than the self-limited impedance.

If the load impedance is smaller, then a re-trapping wave propagates against the direction of power flow, pulling a portion of the electrons from the space charge layer and returning them to the cathode. This re-trapping wave consequently compresses the space charge layer closer to the cathode thus raising the operational impedance of the MITL to a value much closer to the vacuum line impedance [22].

2.2 Single Electron Dynamics

The motion of electrons within the crossed electric and magnetic fields associated with the power pulse is the central mechanism behind self-insulating lines. It is therefore instructive to first consider the dynamics of a single electron within the MITL's A-K gap during this interval of time. Because the electron's cyclotron frequency is inversely proportional to its mass, it can complete hundreds of orbits before there is any appreciable change in the voltage and line current.[1] Thus to simplify matters, it is a good approximation to carry out the following analysis with constant fields.

To start with, let us consider an infinite planar geometry as illustrated by figure 2.3. The application of a large electric potential across this gap defines an electric field, $\vec{E}$, in the -$\hat{x}$ direction. The current on the line has an associated magnetic flux density, $\vec{B}$, directed into the page toward the -$\hat{y}$ direction, perpendicular to the electric field. Neglecting the contributions of free electrons to the fields, assume that the electron is initialized on the negatively charged conductor and is at rest, i.e. zero kinetic energy. The electric field, which is normal to the conductor, begins to accelerate the electron toward the anode. Soon after, the magnetic field acts on the relative motion of the electron at right angles, deflecting it away from the anode

[1] Within a magnetic flux density of 1T, the electron's orbital frequency is roughly 28 GHz.

according to the relativistic[2] Lorentz force,

$$\frac{d}{dt}(\gamma m_e \vec{v}) = -e(\vec{E} + \vec{v} \times \vec{B}), \tag{2.1}$$

where m_e is the electron rest mass, $\vec{v}$ is the electron velocity, and $\gamma = (1 - v^2/c^2)^{-1/2}$ is the relativistic factor. We say that the electron is insulated when enough magnetic force is applied to bend its trajectory back toward the cathode before striking the anode. This causes the electron to adhere to a cycloidal path and experience an average drift towards the load of the transmission line as illustrated in figure 2.3. In the absence of an electric field the electron will experience a stationary circular orbit defined by the Larmor radius, $r_L = v_\perp/\omega_c$, where $\omega_c = eB/m_e$ is the cyclotron frequency. The average drift experienced by the electron can be determined by setting the left hand side of equation 2.1 equal to zero and solving for the velocity [23],

$$\vec{v_d} = \frac{\vec{E} \times \vec{B}}{B^2}. \tag{2.2}$$

When $\vec{E}$ and $\vec{B}$ are perpendicular to each other, the electron drift velocity is just simply given by, $v_d = E/B$.

We can define the critical magnetic field, B_{crit}, as the necessary field strength required such that the electron's orbit is equal to the length of the A-K gap. If viewed from a frame of reference that is equal to the electron drift velocity, $v = E/B$, this is equivalent to stating that self-insulation restricts the Larmor radius to be less than half the distance across the gap [14]. Utilizing d'Alembert's principle of least

[2]The relativistic term becomes significant for $V_o \geq m_e c^2/e = 0.511$ MV.

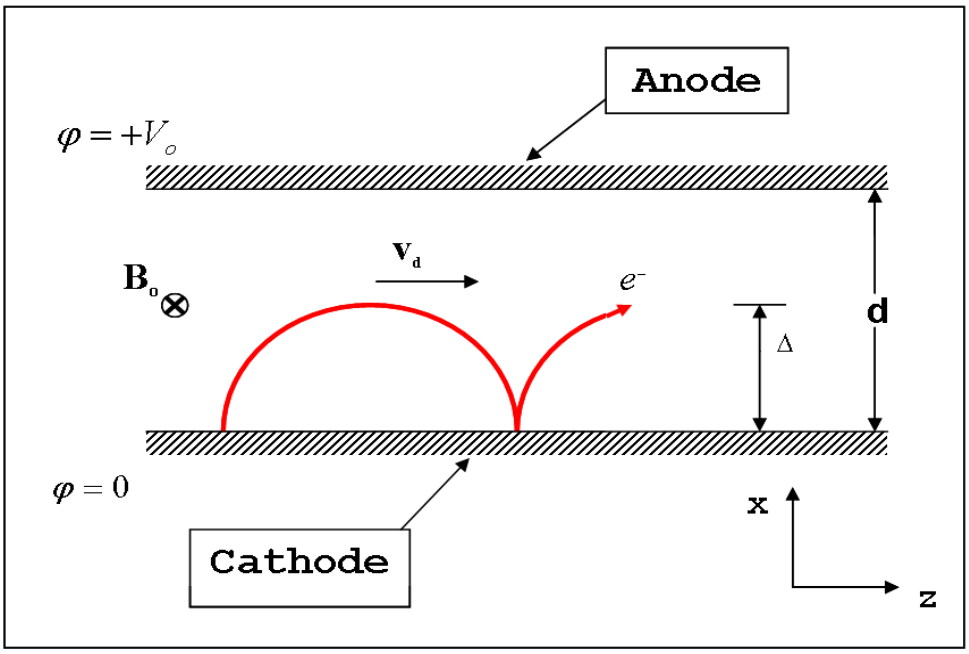

Figure 2.3: Motion of electron in crossed electric and magnetic fields under a stationary frame of reference.

action we can determine the Lagrangian for a single electron in an electromagnetic field [23],

$$Ł = -m_e c^2 \sqrt{1 - \frac{v^2}{c^2}} - e\vec{v} \cdot \vec{A} + eV_o, \tag{2.3}$$

where c is the speed of light in vacuum. The angular canonical momentum is defined as $p_{c,i} = \delta L / \delta v_i$, and for this particular case is given by

$$p_{c,z} = \gamma m_e v_z - eA_z, \tag{2.4}$$

where $\vec{A}$ is the magnetic potential. If we assume that equilibrium has been achieved in the gap, then the total energy of the electrons is conserved. Furthermore, because

all the forces in the direction of the electron drift are uniform, the angular canonical momentum in this direction is conserved as well. Thus, the conservation of energy and canonical momentum in the $\hat{z}$ direction can be expressed by the following equations,

Conservation of energy:

$$\gamma = 1 + \frac{eV_o}{m_e c^2}, \tag{2.5}$$

Conservation of momentum:

$$v_z = \frac{eA_z}{m_e \gamma}. \tag{2.6}$$

Applying the appropriate boundary conditions, i.e. zero magnetic potential and kinetic energy at the cathode, a critical magnetic field can be established [14],

$$B_{crit} = \frac{1}{g}\sqrt{\frac{V_o m_e}{e}(\gamma + 1)}. \tag{2.7}$$

where g is the gap spacing between the anode and cathode. Figure 2.4 illustrates the relationship between the applied voltage across the gap and the minimum magnetic flux density that is necessary for insulation. It is apparent that the magnetic fields required are quite modest for high-voltage allowing for self-insulation in the applications mentioned above.

We can express the critical magnetic flux density another way,

$$B_{crit} = B_o\sqrt{\frac{\gamma + 1}{\gamma - 1}}. \tag{2.8}$$

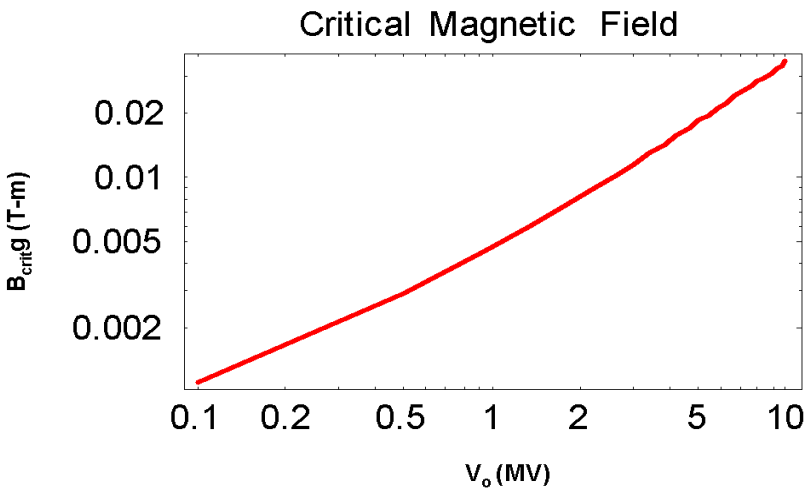

Figure 2.4: $B_{crit}g$ vs. V_o for a planar MITL.

Here $B_o = V_o/cg$ is the magnetic flux density generated by the displacement current in an infinite length MITL. The minimum current that a MITL needs to draw in order to achieve B_{crit} is known as the critical current. The critical impedance of the line can be defined as the potential across the line divided by the critical current. The critical impedance in the single particle case is analogous to the concept of self-limited impedance discussed above [24]. For an infinite planar transmission line, the characteristic impedance is approximately [25]

$$Z_o \approx \sqrt{\frac{\mu_o}{\epsilon_o}}\frac{g}{w}, \tag{2.9}$$

where w is the width of the line and μ_o and ϵ_o are the permeability and permittivity of free space respectively. The ratio of the critical impedance to the characteristic impedance is a function of the applied voltage and is plotted in figure 2.5. Because the relativistic factor in equation 2.8 is never less than unity means that the magnetic flux density generated by the displacement current in an infinite length MITL will always be less than the critical value. Therefore, the characteristic impedance of the

vacuum line will never reach the critical impedance in an infinite line. Insulation can only occur when several electrons are present to conduct through a loss front, supplementing the current drawn by the MITL.

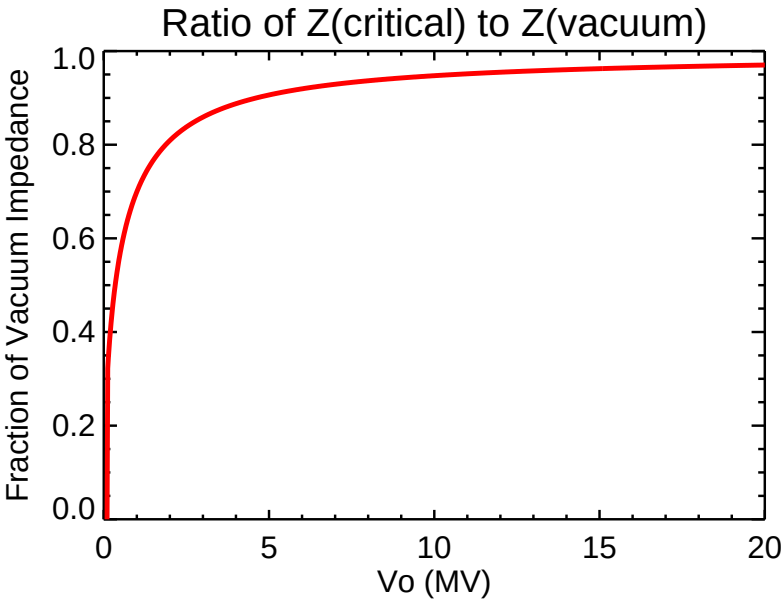

Figure 2.5: Ratio of critical impedance to vacuum characteristic impedance in an infinite MITL under single particle analysis. The critical impedance was defined as the ratio of the line voltage and the critical current. The critical current was approximated using Ampere's Law. This analysis does not take into account the electron space charge present on the cathode.

2.3 Relativistic Electron Flows

While single charged particle dynamics in crossed electric and magnetic fields is helpful in visualizing the individual trajectories of the electrons emitted from the cathode, a complete theory must account for the collective effects of multiple charged particles in the gap. In order to extract a precise description of self-magnetic insulation, a closed set of three-dimensional, time-dependent, partial differential equations is required. These equations are necessary to couple the effects of the electromagnetic forces on the charged particles with the dynamics of the electromagnetic fields involved and the distribution of charge density, which describes the formation of the plasma sheath along the conductor during electron emission. This formulation quickly becomes intractable and generally can only be solved using numerical simulations.

Several analytical models of relativistic electron flows have been developed [3, 26, 27, 28, 29, 30, 4, 31, 32, 13, 33, 34] in an attempt to produce equations of practical value. Fortunately, several characteristics of magnetically insulated flow can be examined by employing appropriate simplifying assumptions.

2.3.1 Quasi-laminar Flow

In the quasi-laminar model [27, 28, 29], the single electron case is extended to several electrons traveling in identical cycloidal orbits distributed along the cathode as illustrated in Figure 2.4a. Due to the relatively small velocities that the electrons experience during emission compared to when they are accelerated through the A-K gap, these flows can be approximated using the same conservation of energy and canonical momentum arguments [28] used above in equations 2.5 - 2.6. Ion emission from the anode is ignored and the relativistic form of the Child-Langmuir law [35] is invoked to account for the space-charge limited nature of the cathode. The potential

between the conductors can be derived using Poisson's equation thus defining a self-consistent set of equations for the electron motion.

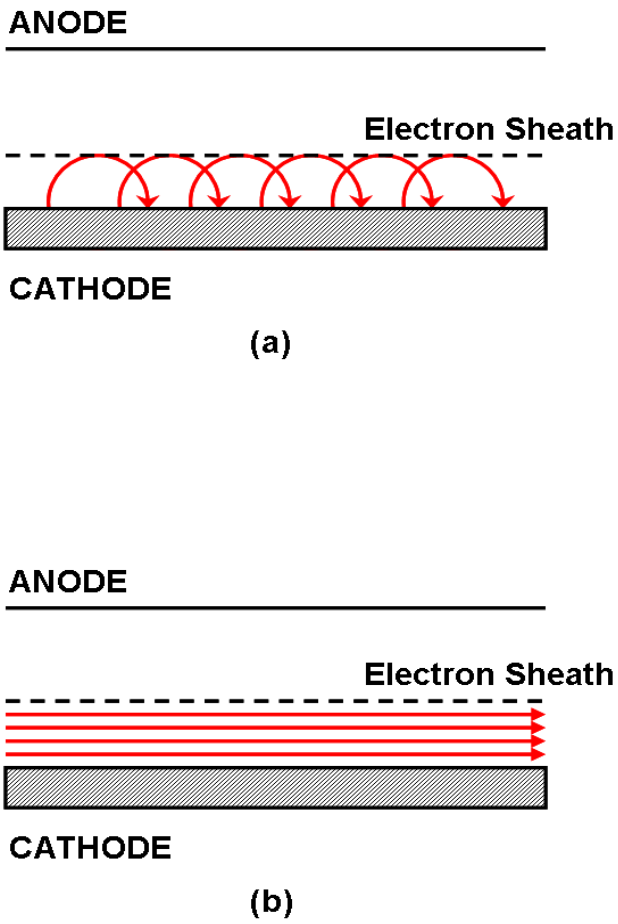

Figure 2.6: (a) Quasi-laminar relativistic electron flow model. (b) Parapotential relativistic electron flow model.

2.3.2 Parapotential Electron Flow

Even though single charged particle dynamics points to cycloidal orbits in the electron flows, numerical simulations show that the trajectories begin moving in straight lines further and further away from the beginning of the MITL. Because the electric and magnetic forces are dominant in relativistic electron flows, the electrons move along equipotential surfaces, which in this case is the cathode. The parapotential model, therefore, generates a self-consistent equilibrium solution for electron flows which exhibit the simplest particle orbits: straight and traveling parallel to the electrodes, Figure 2.4b. Several authors have investigated laminar flows [3, 26][6-7], and show them to be characterized by a conservation of the total electron energy and canonical momentum as was the case in the quasi-laminar model. The analytical solutions of the flow of electron beams along equipotential surfaces are relativistic generalizations of the Brillouin flow [3].

The previous models all greatly depend on the relative trajectories of the electrons within the sheath. Several valuable attributes of electron flow can be investigated, independent of the electron orbits, through experimentally supported assumptions and simple electric/magnetic pressure balance arguments [4, 31, 32][12-14]. The conclusions drawn from these papers will be summarized in the following section.

2.4 Pressure Balance Theory

It has been experimentally observed that MITLs are an efficient conduit of electrical power [36]. Furthermore, experiments support the supposition that the cathode of a magnetically insulated line is a space-charge-limited (SCL) electron emitter, allowing us to treat the entire cathode as a single equipotential surface [32]. It has

been demonstrated that a fundamental understanding of the electron flow in a MITL can be derived under these two assumptions and simple pressure-balance arguments arising from electrodynamics and the conservation of momentum [4].

2.4.1 Line Voltage

To facilitate the development of a pressure-balance theory, the following additional assumptions have been proposed as a result of the above experimental observations [4]: (1) the anode current density is much less than that predicted for SCL ion emission, (2) the electron pressure is negligible compared to the magnetic pressure at the anode and (3) electrons are emitted from the cathode surface with zero kinetic energy. This would suggest that the height of the electron flow across the A-K gap is regulated through a pressure balance attributable to the electric and magnetic fields. If we assume that an equilibrium in the line has been achieved, such that the electron flow is confined to a sheath adjacent to the cathode and traveling parallel to the electrodes without being accelerated in the direction of either, the field pressures at the anode and cathode will be equal,

$$\frac{B_a^2}{2\mu_o} - \frac{\epsilon_o E_a^2}{2} = \frac{B_c^2}{2\mu_o}. \tag{2.10}$$

Here B_c is the magnetic field at the cathode, B_a and E_a are the magnetic and electric fields at the anode respectively, and SCL emission from the cathode has been assumed (i.e. $E_c = 0$). By solving the pressure-balance relation in terms of the electric field at the anode and integrating across the A-K gap, an equation for the line voltage is readily obtained,

$$E_a g = \frac{g}{\sqrt{\mu_o \epsilon_o}} \sqrt{B_a^2 - B_c^2}, \tag{2.11}$$

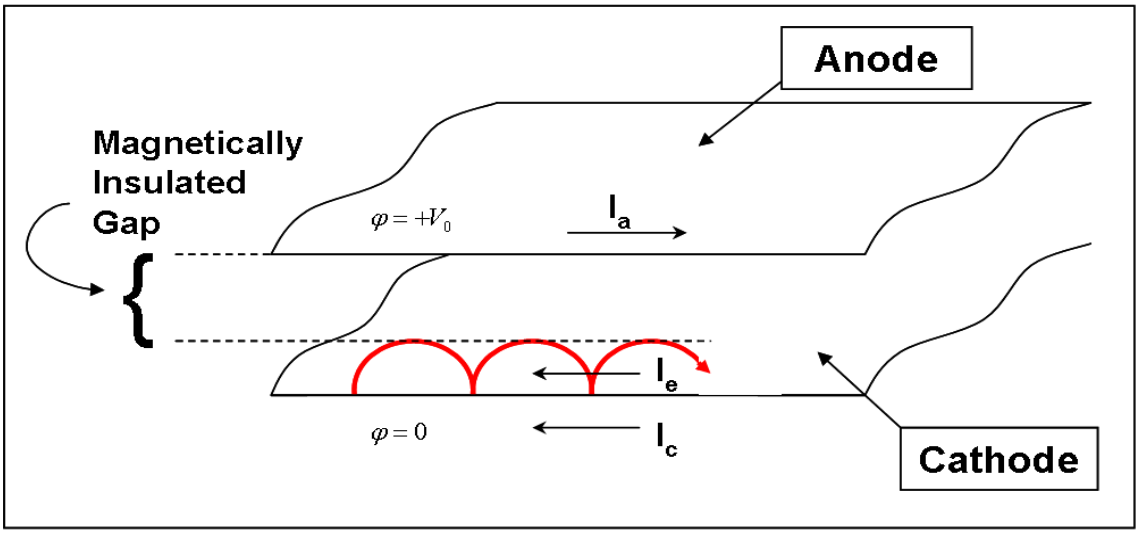

Figure 2.7: Section of magnetically insulated transmission line used to define the anode, cathode, and electron sheath currents respectively.

where g is the distance of the gap spacing.

For a planar MITL, figure 2.7, Ampere's law allows us to express the magnetic flux at the anode and cathode in terms of their respective line current. If we assume that the ratio of the line width, w, to the gap spacing is small enough to neglect fringing effects at the edges of the transmission line then the magnetic fields at the anode and cathode are given by

$$\begin{aligned} |B_a| &= \frac{\mu_o I_a}{w}, \\ |B_c| &= \frac{\mu_o I_c}{w}, \end{aligned} \tag{2.12}$$

where I_a and I_c are the anode and cathode currents respectively. Substituting expressions 2.12 into equation 2.11 gives the line voltage in terms of the line currents,

$$E_a g = Z_o \sqrt{I_a^2 - I_c^2}, \tag{2.13}$$

Here Z_o is the vacuum line impedance given in equation 2.9. This expression continues to hold for a uniform planar disk transmission line where the width, w, is expressed as a circumference in cylindrical coordinates.

If we set the potential at the cathode equal to zero, expression 2.13 gives the voltage across the entire A-K gap. In reality, however, the accumulation of space charge along the cathode will diminish the effective gap length, thus decreasing the line voltage by an amount

$$V = E_a g - V_s, \tag{2.14}$$

where V_s is the potential at the edge of the electron sheath. This quantity is sometimes referred to as the *space charge correction*. For highly insulated MITLs this space charge term is rather small and is negligible for first order approximations of the line voltage. When the space charge layer is of appreciable size, the distribution of the electron density across the gap becomes an important factor.

If the space charge density is assumed to be uniform across the electron layer, a specific expression for the line voltage including space charge correction can be obtained as follows [22]: Solving Poisson's equation across the A-K gap in terms of a constant charge density, ρ_c, gives the following expression for the electric field as a function of the gap spacing,

$$E(g) = -\rho_c g / \epsilon_o \tag{2.15}$$

The energy associated with the acceleration of an electron across the A-K gap by the electric field is a conserved quantity and is equal to the electron's total kinetic energy. If the electron's radial velocity is approximated[3] by $v_r(g) = eB_c g/m_e$, where $B_c = Z_o I_c/(cg)$ from equation 2.10, the following equation for the transverse velocity is obtained,

$$v_z(g) = g\sqrt{\frac{e\rho_c}{m_e\epsilon_o} - \frac{e\epsilon_o Z_o {I_c}^2}{m_e c g}} \tag{2.16}$$

For a real solution to exist, the charge density must be restricted to the following inequality

$$\rho_c \geq \frac{e\epsilon_o Z_o^2 I_c^2}{m_e c^2 g^2}. \tag{2.17}$$

Miller and Mendel [31] use the lower limit of this inequality to derive the following voltage at the edge of the electron sheath

$$V_s = \frac{m_e c^2}{2e}\left(\frac{I_a^2}{I_c^2} - 1\right), \tag{2.18}$$

where the potential at the edge of sheath is assumed to be of the form $V_s = \epsilon_o E_a^2/(2\rho_c)$ for a constant charge density along with a substitution of equations 2.13 and 2.17. Finally, combining equations 2.13, 2.14, and 2.18 gives the line voltage in terms of I_a and I_c,

$$V = Z_o\sqrt{I_a^2 - I_c^2} - \frac{m_e c^2}{2e}\left(\frac{I_a^2}{I_c^2} - 1\right). \tag{2.19}$$

[3]The Lorentz force equation under the assumption of space-charge-emission, i.e. $E_c = 0$.

Contours of the voltage calculated in the above expression appear in figure 2.8. This plot can be extremely useful in approximating the electron flow when the line impedance, electric potential, and total current are known. Each point along a contour gives a possible, however, not necessarily unique combination of anode and cathode currents which satisfy equation 2.19. The asymptotic limits bounding the voltage contours from the left and right represents the two possible extremes for magnetically insulated flow. The left asymptote is known as the *saturated flow* solution and corresponds to the minimum cathode current necessary for insulation. As the cathode current approaches this limit, the electron flow approaches the width of the MITL's A-K gap. The asymptote bounding the contour from the right represents the other extreme where the electron flow is tightly bounded to the cathode. This solution is often referred to as *super-insulated flow*. The minimum of each voltage contour is unique and corresponds to the electron flow which minimizes the total current during insulation. It was originally postulated that MITLs tend to operate at this minimum-current flow because this solution tends to occur within a very close proximity to the flow calculated using minimum energy considerations [21, 4]. Thus it was thought that the dashed line for minimum-current flow in figure 2.8 represented the self-limited flow at which a MITL operates behind the loss front. This was later brought into question with the study of electron flow impedance [13, 33]. Recently, PIC simulations have shown that self-limited flow actually occurs just to the left of the minimum-current flow in the saturated region [22].

2.4.2 Average Electron Drift

In addition to the line voltage, the mean drift velocity of the electrons within the plasma sheath can be derived in terms of the anode and cathode current. Using Poisson's equation to write the electric field strength at the anode, equation 2.13, in

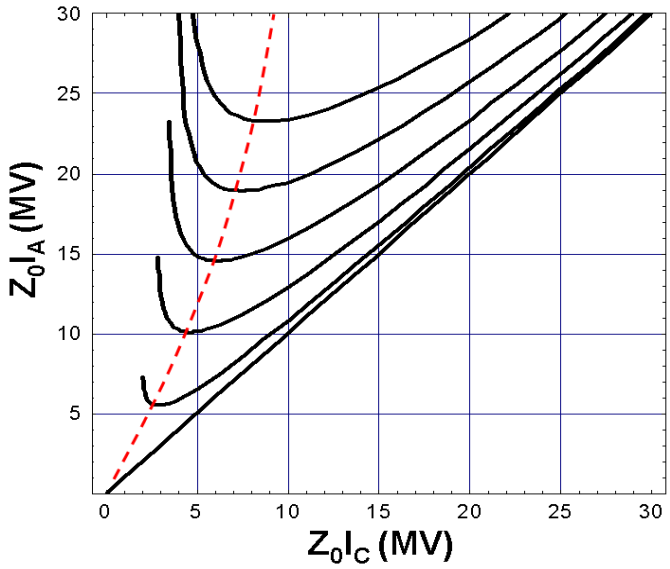

Figure 2.8: Voltage contours in the (Z_oI_a-Z_oI_c) plane for 1-D, planar, self-magnetically insulated equilibrium. Each contour, from bottom to top, represents a line voltage of 4 MV - 20 MV respectively.

terms of charge per unit area, σ,

$$E_a = \frac{\sigma}{\epsilon_o} = \frac{Z_o}{g}\sqrt{I_a^2 - I_c^2}. \tag{2.20}$$

The average electron drift velocity, $\bar{v}$, multiplied by the charge per unit area and the width, w, gives an expression for the electron flow,

$$I_e = \sigma w \bar{v} = I_a - I_c. \tag{2.21}$$

Substituting equation 2.20 into equation 2.21 yields an equation for the electron mean drift velocity,

$$\bar{v} = c\sqrt{(I_a - I_c)/(I_a + I_c)} \tag{2.22}$$

2.5 Precision Electron Flow Measurements

Typically, the electron flow in pulsed power systems with low impedance loads is measured as the difference between the anode and cathode current. For over-insulated systems where the difference between the anode and cathode current can be minimal,

$$\frac{I_a - I_c}{I_a} \leq 0.01,$$

resolving the electron current through the use of typical diagnostic equipment becomes problematic. A new method for extracting precise electron flow measurements has been proposed [12], which allows for the direct measurement of the electron current flow providing a better gauge for the validity of the computer simulated results.

The proposed measurements are being conducted on a radial disk MITL whose general cross-section is illustrated in figure 2.9. This geometry differs from previous examples, in that the gap spacing is no longer uniform but varies with radial position. It has been shown in previous works, utilizing flow impedance modeling[4] [13, 33, 34], that the electron sheath can become unstable as it travels into sections of the MITL where the line impedance is increasing appreciably. In a region of increasing line impedance, a reduction in the electric field strength leads to a decrease in the mean drift velocity of the electrons. The resulting build up of excess charge introduces

[4]This will be covered in section 2.6

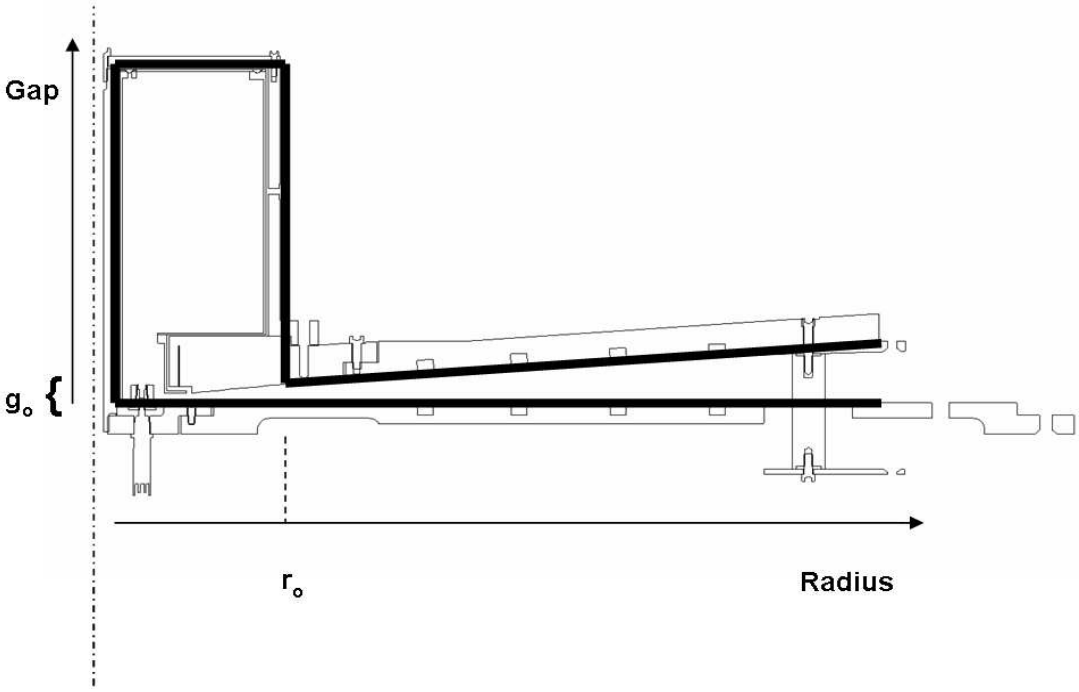

Figure 2.9: "Schematic of the magnetically insulated transmission line and load profile".

an axial electric field component which pushes against the electrons flowing into the region. This electric force reduces the electrons' canonical momentum until they are no longer insulated. This allows the electrons to be trapped in the collector can region upon passing through the smallest part of the gap located at r_o. The reduction in the electric field strength means that there will be more electrons drifting into the collector can than are required to shield the cathode. The excess electrons in this region can only reach the anode by creating a large enough electric field, due to space charge, to overcome the magnetic flux in the load region.

The cross-sectional geometry shown in figure 2.9 allows for the direct measurement of the electron current. The smallest part of the gap, g_o, occurs at the radial distance r_o. As power flows into the MITL from the right it is experiencing constant decreasing

line impedance which causes a steady increase in the electron mean drift velocity as the electrons flow across the cathode toward the left[5]. At the load, however, there is a cavity (electron collector) which rapidly increases the line impedance at that point. As the electrons flow into the cavity they become unstable and are trapped inside the can. A current viewing resistor is placed on the cathode near the entrance of the can to effectively "count" the electrons passing by. The electron collector is designed to take advantage of the electron turbulence created by the enlarged vacuum impedance of the load region. A separate electrode surrounds the collector and carries the anode current. The electron collector encloses 97% of the magnetic flux in the load region. When the flowing electrons enter the collector, this separate electrode appears like the anode surface and subsequently captures the electrons when they transition this gap. Because of the reduced electric field in the enlarged region of the load, the mean electron drift velocity decreases. This causes a build-up of space charge until enough electric field is created to allow the electrons to transit the magnetic flux and reach the anode.

2.5.1 Theoretical Model

In order to design a MITL whose electron flow is radially variant requires that electrons are capable of being re-trapped by the field-emitting surface. It has been shown that electrons which continually gain total energy will be returned to the cathode [37]. This is possible if the betatron acceleration, a gain in energy due to an increasing magnetic field[6] [38], is greater than the energy lost. The electron can lose energy through synchrotron radiation, which for a particle orbiting within orthogonal

[5]This velocity is due to the $\vec{E} \times \vec{B}$ drift. As the radius decreases, $|\vec{E}|$ increases with a reduction in the gap spacing and $|\vec{B}|$ falls off as $1/r$.

[6]At $r = 0.2$ m, an electron 1 mm above the cathode will experience an increase of 100 eV/cm as it drifts toward the load.

electric and magnetic fields scales as the square of the electric field strength[7]. By utilizing a MITL with a radially changing A-K gap, an inductive profile can be established which determines how the magnetic flux is distributed along the line and the rate at which the electric field strength will be modified due to a change in the gap spacing. It is therefore advantageous to examine the rate of the electron flow with regard to the line inductance.

Consider a MITL possessing an inductive load geometry. The lumped inductance at any radial position, r, can be defined as the lumped inductance at the load and an integral of the distributed transmission line inductance,

$$L(r) = L_o + \frac{1}{c}\int_{r_o}^{r} Z dr'. \tag{2.23}$$

The voltage at any radial position, r, is proportional to the rate of change in the anode current by the lumped inductance in 2.23,

$$V = L(r)\frac{dI_a}{dt}. \tag{2.24}$$

The MITL line voltage in terms of the anode and cathode currents was developed above in equation 2.19,

$$V = Z\sqrt{I_a^2 - I_c^2} - \frac{m_e c^2}{2e}\left(\frac{I_a^2}{I_c^2} - 1\right).$$

[7]At $E = 1$ MV/cm this is approximately $420 \cdot 10^{-6}$ eV per electron over a 40 ns power pulse

If the anode current is considered to be much greater than the electron current then the above expression can be simplified

$$\begin{aligned} V &= Z\sqrt{I_a^2 - (I_a - I_e)^2} - \frac{m_e c^2}{2e}\left(\frac{I_a^2}{(I_a - I_e)^2} - 1\right), \\ V &\approx Z\sqrt{2I_a I_e}, \\ I_e &\approx \frac{V^2}{2I_a Z^2}. \end{aligned} \tag{2.25}$$

This expression for the electron current can then be related to the total inductance by substituting 2.24 into 2.25,

$$I_e \approx \frac{L(r)^2(\dot{I}_a)^2}{2I_a Z^2} = \frac{(\dot{I}_a)^2}{2c^2 I_a}\left(\frac{L}{\dot{L}}\right)^2, \tag{2.26}$$

where the distributed vacuum line impedance was expressed in terms of the lumped inductance given in equation 2.23. Here " $\dot{}$ " and " $\ddot{}$ " denote the first and second time derivatives respectively.

The radial change in electron flow is then given by

$$\frac{\delta I_e}{\delta r} = \frac{(\dot{I}_a)^2}{c^2 I_a}\left[\frac{L}{\dot{L}} - \frac{L^2\ddot{L}}{\dot{L}^3}\right]. \tag{2.27}$$

Dividing expression 2.27 by the total electron flow yields the fractional change in electron current or "re-trapping parameter", which will be defined as

$$\beta = \frac{1}{I_e}\frac{\delta I_e}{\delta r} = 2\frac{\dot{L}^2 - \ddot{L}L}{L\dot{L}}. \tag{2.28}$$

The general solution of this differential equation is given by

$$L(r) = C_2 \exp\left[-\frac{2C_1}{\beta}\exp\left[-\frac{\beta}{2}(r - r_o)\right]\right], \tag{2.29}$$

where C_1 and C_2 are constants of integration, and the inductance can be expressed as a function of the electron flow rate.

Constant Electron Flow:

For constant electron flow, $\beta = 0$, the singularity in equation 2.29 can be avoided by substituting this value directly into the differential equation above, 2.28. This produces the following expression for the inductance

$$\begin{aligned} \dot{L}^2 &= \ddot{L}L, \\ L(r) &= C_2 \exp[C_1(r - r_o)]. \end{aligned} \tag{2.30}$$

The inductance at $r = r_o$ is the lumped load inductance, $C_2 = L_o$, and the derivative at $r = r_o$ results in $C_1 = \dfrac{Z(r_o)}{L_o c}$. The numerator of C_1 is just the vacuum line impedance for a radial disk transmission line, $Z(r_o) = \dfrac{60 g_o}{r_o}$. The impedance profile for a constant radial electron flow is given by,

$$\begin{aligned} Z(r) &= cL\dot{(}r) \\ &= c(C_2 C_1 \exp[C_1(r - ro)]). \end{aligned} \tag{2.31}$$

Substituting the constants of integration back into expression 2.31 generates an equation for the vacuum line impedance as a function of r,

$$Z(r) = \frac{60 g_o}{r_o} \exp\left[\frac{60 g_o (r - r_o)}{L_o r_o c}\right], \tag{2.32}$$

where g_o is the minimum gap distance and c is the speed of light in vacuum.

Reducing Electron Flow:

When there is appreciable change in the electron flow versus radius, i.e. $\beta = 1$, the general solution must be used. Utilizing the same boundary conditions as in the constant electron flow case, the constants of integration are as follows:

$$\begin{aligned} C_1 &= \frac{Z(r_o)}{L_o c}, \\ C_2 &= L_o \exp \frac{2Z(r_o)}{L_o c}. \end{aligned} \tag{2.33}$$

The vacuum line impedance for reducing electron flow, β=1, with the above constants of integration results in the following expression,

$$Z(r) = \frac{60 g_o}{r_o} \exp\left[\frac{120 g_o}{c L_o r_o} - \frac{120 g_o}{c L_o r_o} \exp\left[-\frac{1}{2}(r - r_o)\right] - \frac{1}{2}(r - r_o)\right]. \tag{2.34}$$

2.5.2 Geometry Calculations

The equations in section 2.5.1 provide an excellent approximation for the geometrical profiles in an over-insulated system[8]. For the radial disk transmission line experiment, an under insulated system would be more advantageous. This would allow the difference between the anode and cathode currents to be accurately measured, providing further comparison for the electron flow current directly recorded by the CVR. In order to design an exact geometrical profile for a particular flow rate, the gap spacing vs. radius must be extracted from equation 2.19 using computational methods[9]. To provide an initialization for the root-solvers, which are needed in the computational analysis of the non-linear equations, the over-insulated approximation will be used in the initial design of the gap profiles below.

Using voltage and current calculations on an experimentally measured power pulse through the system generates the radial gap spacing profile for a particular electron flow rate. Several other parameters such as maximum gap spacing and load inductance, were chosen to satisfy structural constraints due to the existing pulsed-power hardware while maintaining a resolvable difference between the electrode currents.

In general, the gap spacing is related to the vacuum line impedance by the following expression,

$$g(r) = \frac{Z(r)r}{60}. \tag{2.35}$$

[8]Over-insulated MITLs, as found in the Saturn and the ZR experiments at Sandia National Laboratories, are characterized by sheath thicknesses which are a very small fraction of the gap spacing

[9]This will be discussed further in Chapter 3 along with the hardware specifications used in this experiment.

Constant Electron Flow:

For the case of constant electron flow, $\beta = 0$, the vacuum line impedance given in 2.32 is substituted into equation 2.35 to yield an expression for the radial gap spacing,

$$g_{const}(r) = \frac{g_o r}{r_o} \exp \frac{60 g_o (r - r_o)}{L_o r_o c}. \tag{2.36}$$

This calculated geometric profile is constrained by three main variables: the minimum gap spacing, the radial position at which this minimum occurs, and the load inductance. The maximum gap spacing for this experiment was constrained to 32.6 mm. The minimum gap was set at a radial distance of 50 mm and is fixed by the chosen β and the maximum gap spacing. Two different collector cans were designed to provide load inductances of 50 nH and 33.9 nH. The geometric profile for the constant electron flow with $L_o = 50$ nH is shown in figure 2.10.

The equations in section 2.5.1 are set by the approximation of electron flow current given in 2.25. It can be shown experimentally that the time change in anode current is approximately constant during insulation [12]. Using data supplied by an experimentally measured forward wave from the pulse power driver, the anode current was approximately 290 kA over an interval of 20 ns. This data was substituted back into the voltage waveform equation, 2.25, along with the profile constraints from above yielding,

$$\begin{aligned} V(r) &= L_o \exp \frac{60 g_o (r - r_o)}{L_o c r_o} \\ &= 7.68 \times 10^5 \exp 0.25(r - 0.05). \end{aligned} \tag{2.37}$$

Using the anode current data supplied by an experimentally measured forward

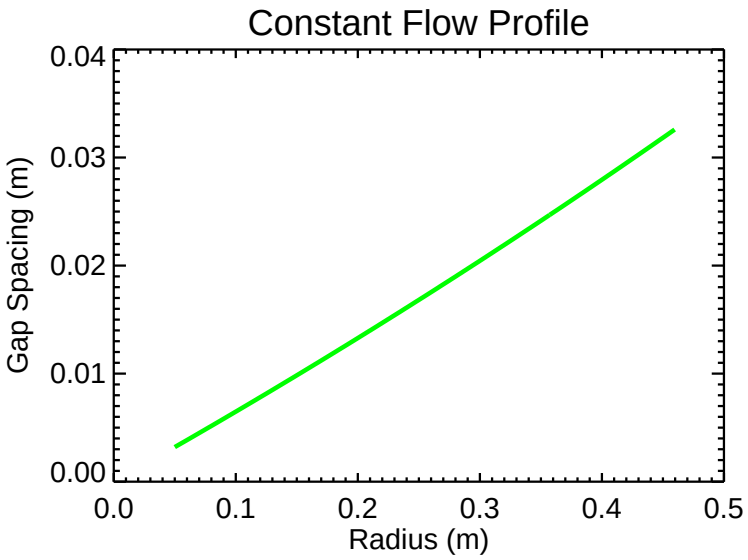

Figure 2.10: MITL gap spacing vs. radius ($\beta = 0$).

wave from the pulse power driver, an expression for the voltage waveform can be substituted back into 2.25 to determine the electron flow in the MITL. The plot of the radial electron flow is given in figure 2.11. As expected, the electron flow is constant and independent of radial location. The impedance profile for this flow rate is illustrated in figure 2.12. Because the feed voltage is approximately constant over the 20ns pulse, the vacuum impedance remains nearly level only rising marginally with increasing radius.

Reducing Electron Flow:

For a reducing electron flow, $\beta = 1$, the geometric profile must be determined from the general solution of equation 2.28. Just as in the case of constant electron flow, the gap spacing can be determined from equation 2.35,

$$g_{reducing}(r) = \frac{g_o r}{r_o} \exp\left[\frac{120 g_o}{c L_o r_o} - \frac{120 g_o}{c L_o r_o} \exp\left[-\frac{1}{2}(r - r_o)\right] - \frac{1}{2}(r - r_o)\right]. \quad (2.38)$$

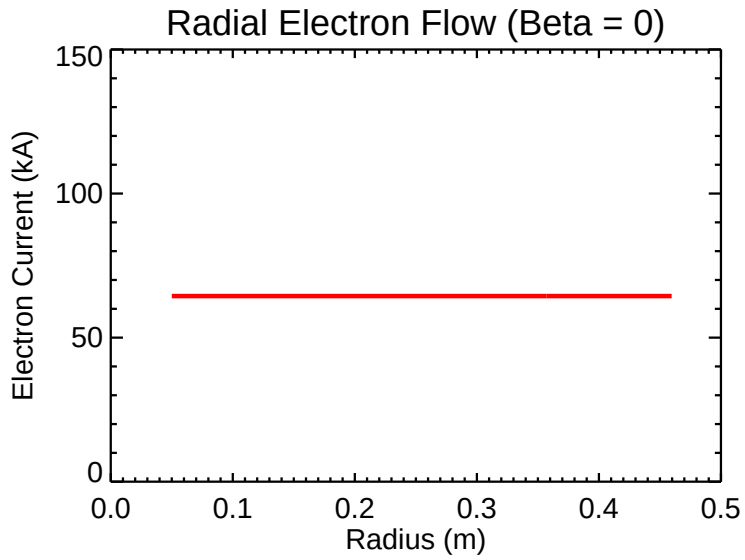

Figure 2.11: Electron flow current vs. radius ($\beta = 0$).

Using the same experimental data, profile constraints, and equation 2.25, the gap profile and reducing electron flow current can be plotted as shown in figures 2.13 and 2.14 respectively. The concave curvature of the gap spacing in this case is more pronounced than the constant flow profile. The electron current is shown to increase with radius and is therefore reducing in the direction of power flow. The corresponding impedance profile for the reducing electron flow is shown in figure 2.15. Once again, the voltage is approximately constant over the pulse duration leading to a steady radial impedance that slightly decreases with radius. As β continues to increase, the vacuum line impedance will continue to decrease over the radial span of the transmission line to where these systems are not physically realizable.

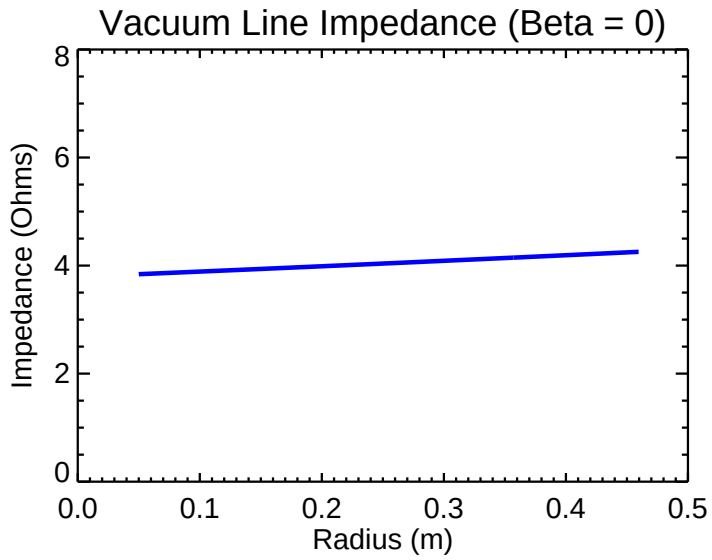

Figure 2.12: Impedance profile for constant electron flow, $\beta = 0$.

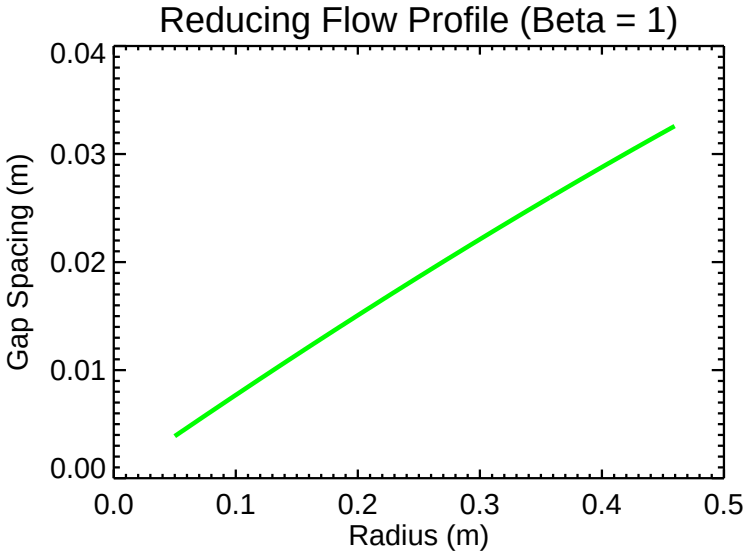

Figure 2.13: MITL gap spacing vs. radius ($\beta = 1$).

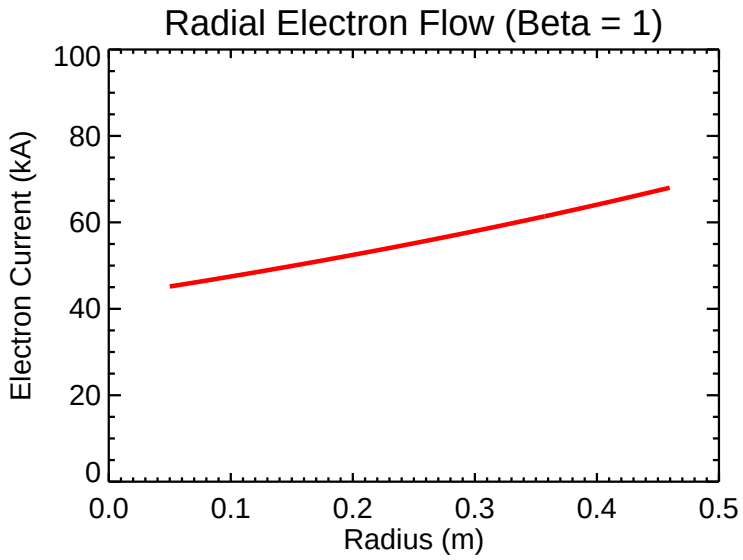

Figure 2.14: Electron flow current vs. radius ($\beta = 1$).

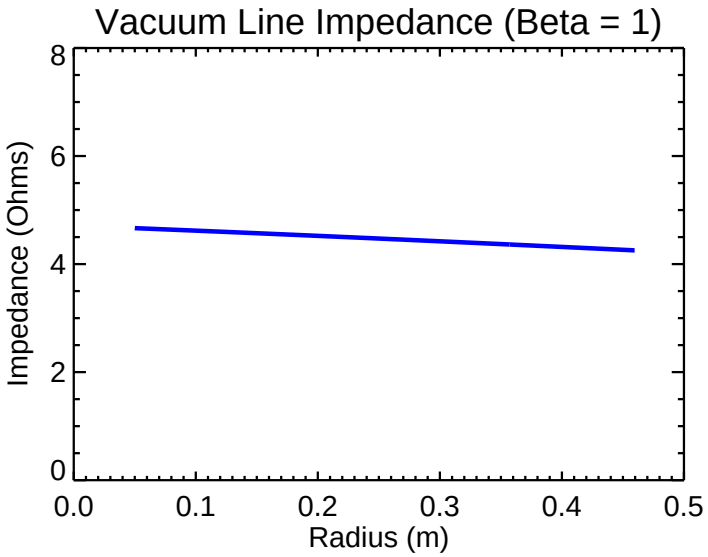

Figure 2.15: Impedance profile for reducing electron flow, $\beta = 1$.

2.6 Flow Impedance Modeling

Due to the electron space-charge throughout an insulated transmission line, an operational line impedance is difficult to define. While an impedance profile can be calculated under certain assumptions[10], a useful generalization for studying the dynamics of the radial electron flow would be more informative. A parameter based upon the centroid positions of the space-charge distribution and current density relative to the anode allows for a dynamic representation of the insulation process. These "flow impedances" offer a direct comparison to the vacuum impedance of the line in the absence of space-charge.

The electric flow impedance, Z_f, represents the operational line impedance of the MITL. It is defined as the separation between the anode and the mean position of the cathode space-charge in terms of the vacuum line impedance. For the radial disk MITL shown in figure 2.16, the A-K gap has been divided into two segments, g_1 and g_2, at a radius of $r_f \simeq 0.33$ m. The vacuum line impedance at this radius is defined across the entire gap, $g_f = g_1 + g_2$, according to $Z_v(r_f) = \dfrac{60 g_f}{r_f}$. The electric flow impedance is defined by the separation between the charge centroid and the anode, g_2, and is given by

$$Z_f(r_f) = \frac{60(g_f - g_1)}{r_f}. \tag{2.39}$$

In general, the electric flow impedance in a radial disk MITL is a function of the anode current and the total azimuthal charge for a given gap spacing, g. If Q_a and Q_c are taken to be the total enclosed charge on the anode and cathode respectively, then the anode potential can be expressed in terms of the flow impedance [13],

[10] In section 2.5.1 this is done for a MITL assuming over-insulated flow such that $I_a \gg I_e$.

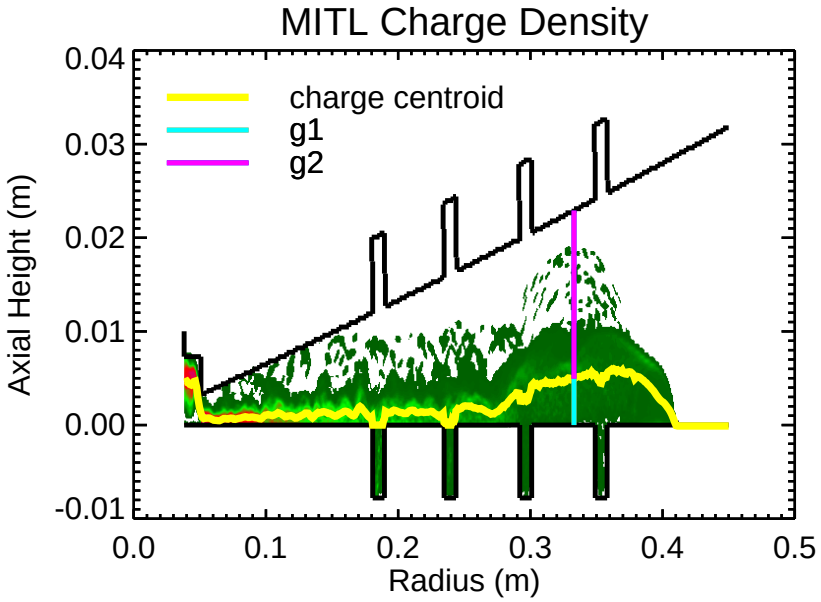

Figure 2.16: MITL charge density prior to full insulation. The centroid of the charge distribution is shown. At $r_f \simeq 0.33$ the total gap spacing, g_f, is partitioned into two segments, g_1 and g_2. The electric flow impedance is defined as the vacuum line impedance with the gap spacing equivalent of g_2.

$$V_a = Z_f c Q_a + (Z_v - Z_f) c Q_c. \tag{2.40}$$

In the case of space-charge-limited-emission, figure 2.16, the charge along the cathode can be represented by a thin charge layer existing at the centroid of the charge distribution in the gap such that $Q_c = 0$. This contributes to a simplified form [11] for the electric flow impedance, which can be expressed in terms of anode potential and the line currents [39, 13],

$$Z_f = \frac{V}{cQ_a} = \frac{V}{\sqrt{I_a^2 - I_c^2}}. \tag{2.41}$$

[11] Low-pressure relativistic electron flows, where $I_a^2 - c^2 Q_a^2 \simeq I_c^2 - c^2 Q_c^2$.

At a particular radius, r_o, the vacuum impedance of a radial disk is given by, $Z_v(r_o) = \dfrac{60 g_o}{r_o}$, where g_o is the distance between the anode and cathode at that position. We can therefore develop a change of variable to relate a given gap distance across the transmission line to the corresponding impedance,

$$G = \frac{1}{2\pi}\sqrt{\frac{\mu_o}{\epsilon_o}}\frac{g}{r} \approx 60\frac{g}{r}. \tag{2.42}$$

The centroid of the space-charge across the transmission line is defined by ratio of the first moment of its distribution to that of the zeroth moment,

$$\frac{\int_{Q_c}^{Q_a} g dQ}{\int_{Q_c}^{Q_a} dQ} = g_o - g_c, \tag{2.43}$$

where g is the spacing in the $\hat{z}$ direction, g_c is the distance between the charge centroid and the anode, and Q is the charge per unit length across the gap. If g is replaced with G, to incorporate the change in variable, the centroid would be located at $Z_v - Z_f$ where distance is now in units of impedance.

A typical voltage profile in terms of the variable G is given in figure 2.17. The slope of the line voltage is equal to $cQ(G)$ and is tangent to lines representing the charge on the anode, Q_a, and cathode, Q_c. In this example, the slope of $cQ_c = 0$ because of the space-charge-limited-emission. At the intersection of the two tangent lines, the potential is equal to the difference between the vacuum line impedance and the electric flow impedance.

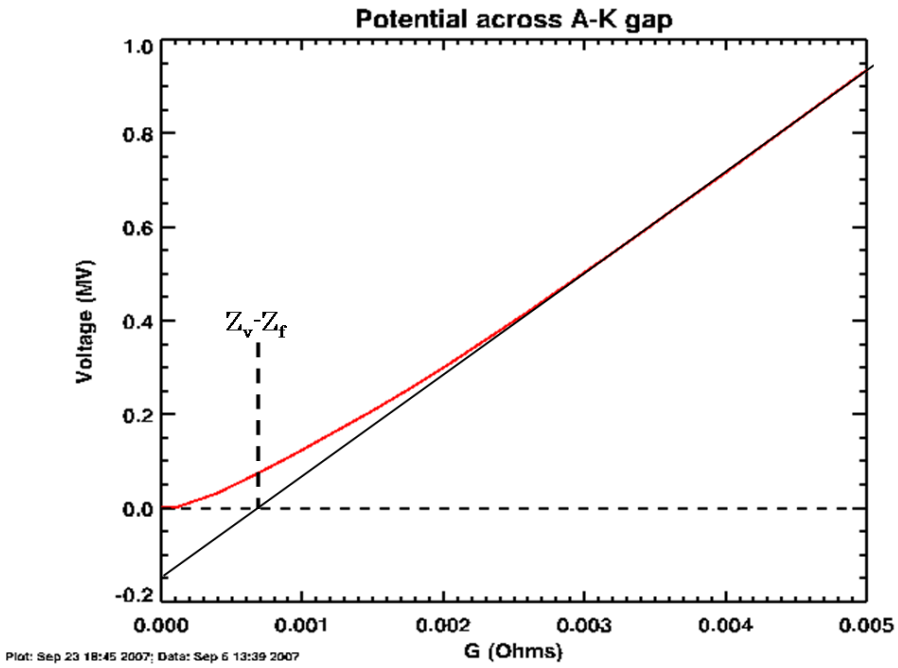

Figure 2.17: Voltage profile across the A-K gap of a typical radial disk line at high insulation. Space-charge-limited emission has driven the electric field at the cathode to zero.

A second flow impedance can be defined from the centroid of the current density within the transmission line gap. This impedance is known as the magnetic flow impedance, Z_m, and is determined by the separation between the anode and the mean position of the current density of the electron flow [13],

$$cA_a = Z_m I_a + (Z_v - Z_m) I_c, \tag{2.44}$$

where A_a is the magnetic vector potential at the anode. Because the average electron velocity is much higher near the anode the current will be larger near the top edge of the sheath. Thus, the location of the current density centroid will typically be closer to the anode than the centroid of the charge density, as shown in figure 2.18,

such that

$$0 < Z_m \leq Z_f < Z_v. \tag{2.45}$$

Usually, the values of the two flow impedances are relatively close and equality holds when the charge distribution can be approximated by a single layer of zero thickness.

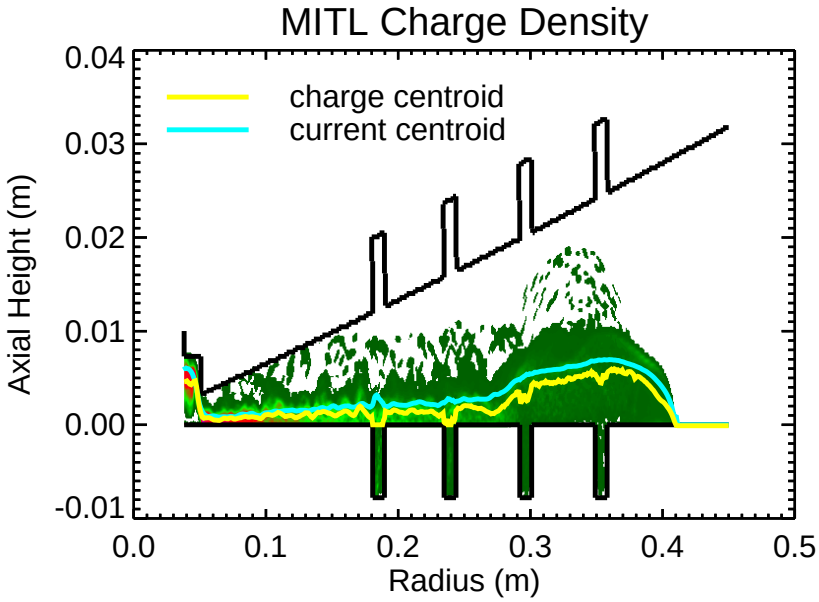

Figure 2.18: MITL charge density prior to full insulation. The centroids of the charge distribution and current distribution are both shown. The centroid of the current distribution is closer to the anode than that of the charge distribution.

If we consider the electron charge density and the magnitude of the magnetic field to be constant in a narrow region near the cathode, the same arguments for the uniform density which was derived in section 2.4.1 hold, where $\rho_c = -e\epsilon_o B_c^2/m_e$. Assuming azimuthal symmetry, the change in the total charge profile across the gap can be expressed as,

$$\begin{aligned} c(\frac{dQ}{dg})_{cathode} &= 2\pi r g c \rho_c \\ &= 2\pi r g c \frac{-e\epsilon_o B_c^2}{m_e} \\ &= \sqrt{\frac{\mu_o}{\epsilon_o}} \frac{g}{2\pi r} \frac{-eI_c^2}{m_e c^2}, \end{aligned} \tag{2.46}$$

Using the change in variables defined in equation 2.42,

$$c\left(\frac{dQ}{dG}\right)_{G=0} = \frac{I_c^2}{m_e c^2/e}. \tag{2.47}$$

This is valid for all G such that $0 < G < G_s$, where G_s is the impedance at the edge of the electron sheath. For $G > G_s$ the change in the charge with respect to impedance is equal to zero. If we substitute expression 2.47 into the centroid distribution and incorporate the appropriate change in variables, then the electric flow impedance can be expressed as,

$$Z_f = \frac{Z_v + [Z_v^2 - 2(m_e c^2/e)(V_a/I_c^2)]^{1/2}}{2} \tag{2.48}$$

When the equation for electric flow impedance given in 2.41 is substituted into this expression, the line voltage is shown to be equivalent to the pressure-balance formulation above, (i.e. equation 2.19).

Chapter 3

Experimental Setup

The radial dependence of the MITL gap spacing is directly related to the inductance profile of the transmission line and subsequently the electron re-trapping rate, β. For fractional flow rates that are approximately constant this parameter is nearly zero. For $\beta > 0$, the fractional flow rate describes a reduction in the electron flow as the radius decreases. A large enough discrepancy in this fractional change of equilibrium flow is necessary to obtain an empirical indication of which operating regime provides greater stability. The experiments supporting this dissertation were conducted using three separate anode geometries. The gap spacing profiles were set for the case of near constant electron flow, $\beta = 0$, and two separate cases of significant electron flow reduction, $\beta > 1$. In addition to studying variations in anode geometry, additives to the cathode surface were incorporated to examine the line voltage threshold necessary for explosive electron emission. This allowed for an increase in electron density at a lower power threshold subsequently decreasing the time required for magnetic insulation to occur.

3.1 Hardware

The MITL hardware consists of two metallic, radial disk electrodes; each containing twelve large signal B-dot probe diagnostics and centered round an electron can as illustrated in figure 3.1. Because the electron current flow is constrained against the cathode, the simulation data from this surface is of critical importance. To avoid stair-stepping in the PIC code MITL simulation[1], a flat cathode disk was incorporated into the gap spacing profile. The anode is shown to have a slightly curved surface which fully characterizes the radial dependence of the gap[2] used to set the MITL vacuum impedance for a particular electron flow rate. The collector can is situated in the middle of the anode and provides the inductive load cavity

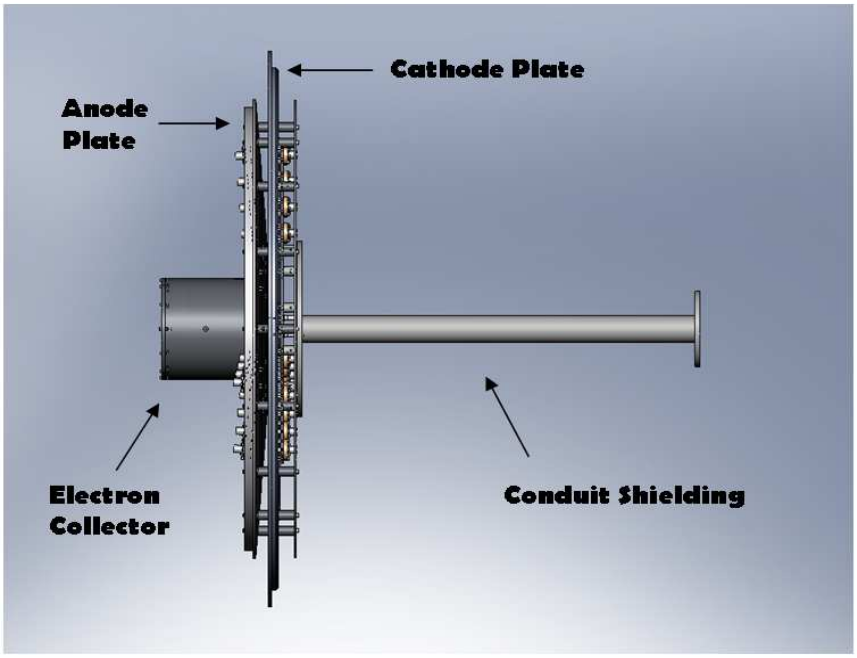

Figure 3.1: Side profile of MITL hardware.

[1]This is covered in greater detail in Chapter 4.
[2]Chapter 2, section 2.5.2

necessary to trap the electrons below the minimal radius. A section of copper piping is shown connected to the cathode providing a shielded conduit to run the signal cables from the cathode's current monitors out to the data acquisition system.

Anode Profiles:

Due to the physical constraints imposed by the pre-existing pulse-driver hardware the radius of the anode and cathode plates are fixed as well as the maximum distance between them. Since the maximum gap spacing between the electrodes is constant, the minimum gap for each anode profile will vary. The curvature for each profile was determined from the exact pressure-balance formulation of MITL line voltage, equation 2.19. Because of the nonlinear relationship between the gap spacing and the anode current, points along the curved surface had to be extracted using a root-solving algorithm which was based on Newton's Method[3]. The computational analysis developed previously, in section 2.5.2, provided the initial approximation needed for the root-solvers to converge. An azimuthal cross-section illustrating the anode curvature is given in figure 3.2. Each profile has a maximum gap spacing of approximately 0.033 m located at a radius of 0.45 m. The gap spacing minimum is located 0.05 m from the center of the load which defines the inner edge of the electron collector's base. The curvature of the anode for smaller radii is defined by an anode insert plate positioned underneath the electron can which sets the minimum height of the gap. Because the load inductance is held constant for each experiment, the minimum gap distance along with the curvature in the anode plate sets the profile for a particular electron flow rate. A summary of the anode profiles computed for this experiment are given on the following page in table 3.1.

[3]An iterative algorithm where an initial estimate is chosen that is reasonably close to the function's root and then updated with the x-intercept of the function's tangent.

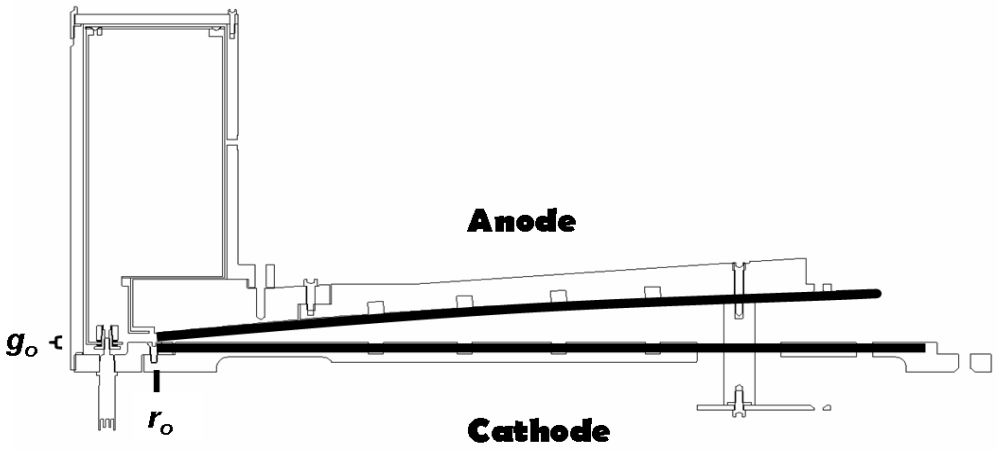

Figure 3.2: Azimuthal cross-section of MITL hardware.

Anode Profile	L_o**(nH)**	g_o**(m)**	**Comments**
$\beta = 0$	50	0.0032	Constant electron flow
$\beta = 1$	50	0.0039	Reducing electron flow
$\beta = 3.7$	50	0.006	Reducing electron flow

Table 3.1: Anode gap profiles used in experiment. In each case the minimum gap spacing occurs at $r_o = 0.05$ m and the maximum gap spacing is approximately 0.0326 m at a radial distance of 0.45 m. A reduction in load inductance results in an increase in β. For the 33.9 nH load each β is increased by approximately 0.2.

Collector Can:

The lumped inductance of the load, L_o, is a key component in determining the curvature of the anode's gap spacing profile. For this experiment two separate inductive loads of 50 nH and 33.9 nH were utilized. Each load was designed to maintain the physical constraints imposed by the hardware of the pulsed-power driver and to provide the necessary inductance relative to the diagnostic shielding conduit[4]. The change in inductance was set by the length of the outer housing of the load cavity, which resulted in a larger electron re-trapping rate, β, for lower inductive loads. This allowed for slight modifications of the electron flow in the disk. Each geometry of the electron can was set by the distributed coaxial load inductance,

$$L_{dist} = \frac{\mu_o}{2\pi} \ln \frac{r_{out}}{r_{in}}, \tag{3.1}$$

where r_{out} and r_{in} are the outer and inner radii of the coaxial geometry respectively and μ_o is the permeability of free space. The height of the can is set by the sum of each section's distributed inductance. Figure 3.3 shows the cross-section of the 50 nH load geometry whose general dimensions are given in table 3.2.

In order to trap the electrons within the load region, the inner-collector can must be held at a "floating potential" such that the electrons are not immediately returned to the anode. Figure 3.4 provides a cut-away cross section of the entire load region. The inner collector, which encloses the vast majority of the load volume, is connected directly to the current-viewing resistor contained at the base by a center spool which supports the can by connecting to the inner collector lid. A gap of 0.09 inches is maintained around the collector to insulate it from the anode. A center rod provides the return path from the cathode to the outer housing of the load which is directly connected to the anode plate.

[4]Discussed in section 3.2

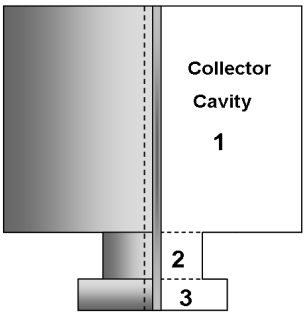

Figure 3.3: Cross-section of load inductance. Center spool is shown and defines the inner radius of the coaxial geometry. In order to calculate the total inductance the load has been divided into three pieces: 1 - Collector Region, 2 - Throat, 3 - Base.

Load Section	r_{in}**(m)**	r_{out}**(m)**	**Length(m)**	**Inductance(nH)**
Collector	0.008	0.095	0.071	34.74
Throat	0.008	0.051	0.037	11.81
Base	0.008	0.038	0.007	5.49
Total				49.5

Table 3.2: Dimensions of electron collector can as calculated from a lumped coaxial load inductance model. The dimensions of the throat region include the bottom cavity which houses the CVR diagnostics.

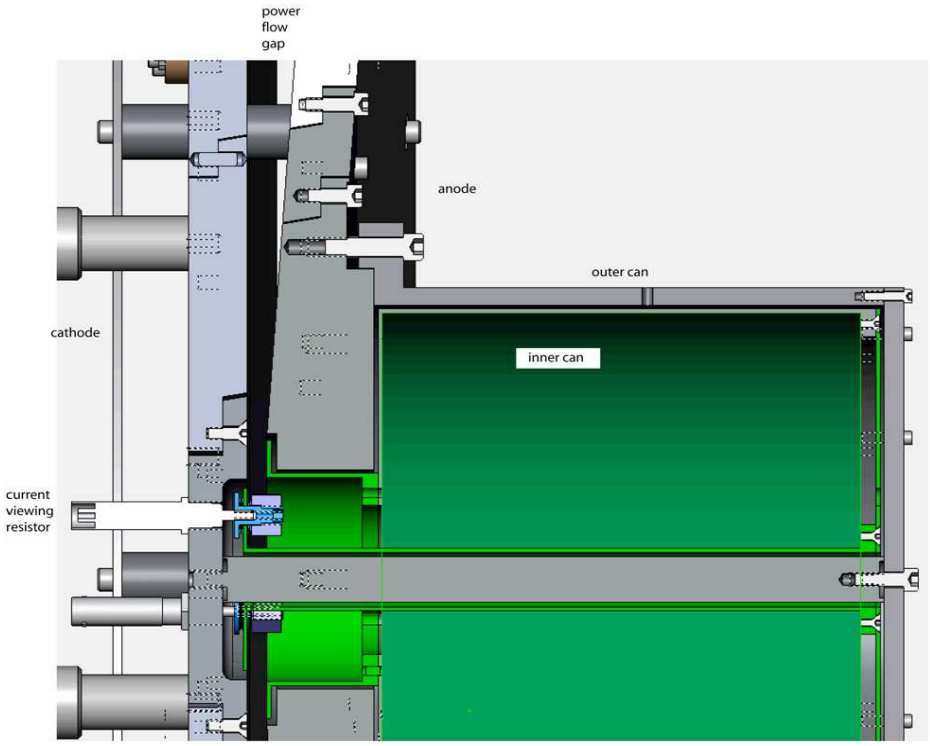

Figure 3.4: Cross-sectional cut-away of the load region. The collector can is the inner cavity and maintains a 0.09 inch gap separation from the wall of the outer housing. The collector can is attached to a center spool which defines its inner diameter. The center rod which attaches the outer housing directly to the cathode is insulated from the center spool by a 0.09 inch gap.

Initial shots demonstrated problems with shorting between the inner and outer can as a result of alignment issues with the pulsed-power driver hardware and flexing of the collector parts. To alleviate this problem, later shots were conducted with only a partial can, consisting of just the center rod and inner collector lid, as shown in figure 3.5. This increased the amount of time before the shorting of the load but decreased the amount of electron flow the CVR could record. Simulations were used to predict the distribution of charge within the load cavity, section 5.5. Knowing how much charge is collected on each surface of the load provides a gauge for the percentage of the total electron current that could be registered by the CVR.

Figure 3.5: Cross-sectional cut-away of the revised load. The inner collector consists of the center rod, the inner collector can lid, and the base plate which supports the CVR diagnostics.

3.2 Pulsed-Power Driver

The radial disk MITL was installed into Sandia National Laboratories' Tesla machine[5], figure 3.6, and driven by its plasma switch triggering section known as T2. Tesla's triggering section is capable of supplying an 800 kV forward wave to a 2 Ω line. This will provide the MITL with 500 kA within a 50 ns pulse width FWHM. The pulse power driver is connected to the cathode, which resides within vacuum, via four coaxial de-ionized water lines through an insulator stack. The location of the MITL hardware within the system is illustrated in figures 3.7, 3.8,

[5]Pulsed-power driver for the Triggered Plasma Opening Switch (TPOS) located in Tech Area IV

and 3.9. The cathode is negatively charged by the four water lines. The cathode completes the circuit through a connector rod that runs from the top of the electron collector can to the base. A parallel branch of the circuit runs from the bottom of the cathode down the conduit pipe which houses the diagnostic signal cables. Prior to magnetic insulation, early in the power pulse, less than $\sim$ 3ns, all of the current is conducted down the conduit shielding which is connected to the negatively charged cathode. Later, the comparatively small lumped inductance of the electron collector can drives the current through the connector rod and back through the anode. This setup allows for the placement of B-dot probes along the cathode. Neglecting losses that are not due to electron emission the anode current will be equal to the cathode current during this time interval just prior to insulation.

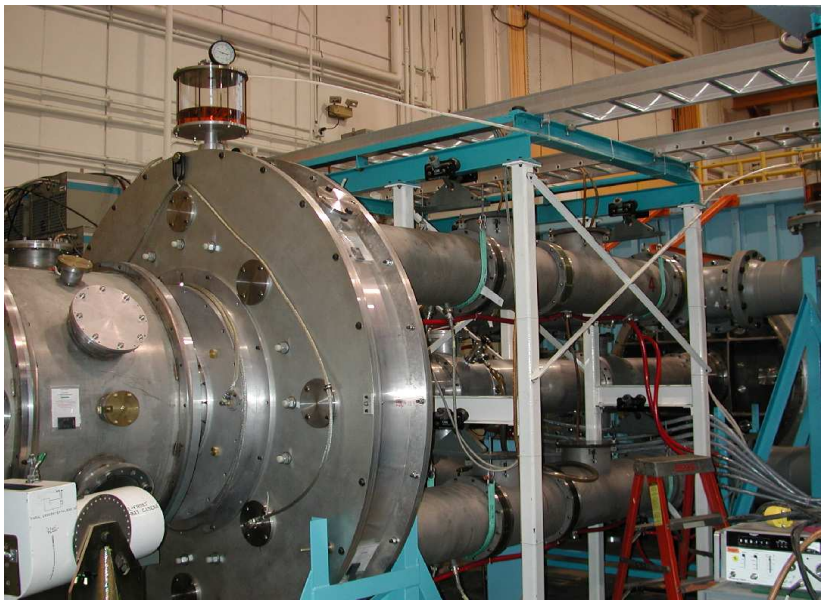

Figure 3.6: Load section of Tesla pulser. MITL hardware is contained within the vacuum section which is at the center of the insulator stack disk. Four pulse-forming water lines supply the power pulse to the MITL.

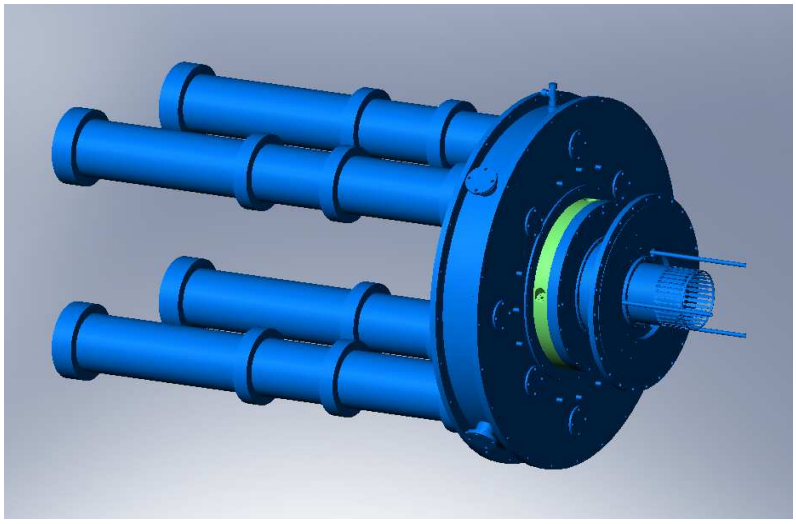

Figure 3.7: Load section of Tesla pulser. MITL hardware is contained within the vacuum section which is at the center of the insulator stack disk. Four pulse-forming water lines supply the power pulse to the MITL.

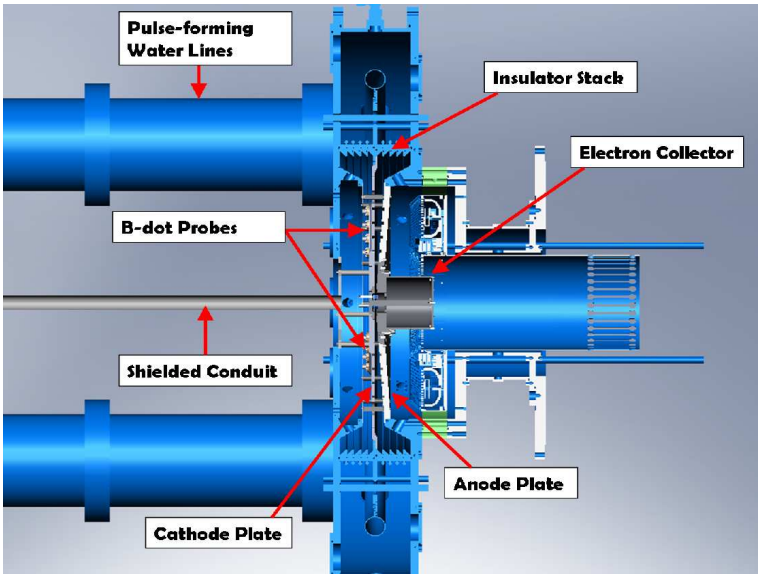

Figure 3.8: Cut-away section of Tesla's insulator stack. Center pipe not shown.

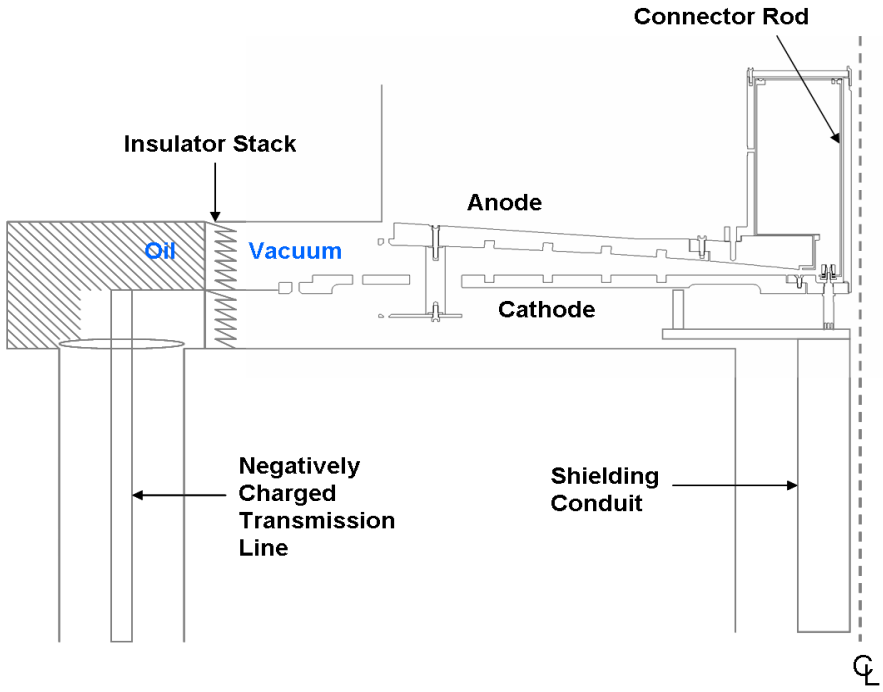

Figure 3.9: Quarter cross-section of MITL setup.

3.3 Diagnostics

Initial electron current measurements for the constant and reducing flow geometries, covered in section 2.5.2, demonstrated the need to resolve a ten percent difference in the anode and cathode disk currents. With this in mind, the data acquisition system was carefully designed for the greatest possible accuracy. To reduce electrical noise, the signals from the current monitors were transmitted through high-quality Heliax 50 Ω foam-flex cables. Foam-flex cables are designed with a solid corrugated outer Cu conductor and a low-loss polyethylene foam dielectric core to drastically reduce attenuation along the line. The Cu jacket provided protection from radio frequency interference as the signals were transmitted to the data acquisition system

which was housed in a separate shielded enclosure as shown in figure 3.10. The shielded enclosure has 30 input signal ports, a RF filter for the incoming power, and provides ample air circulation to prevent overheating of the equipment. The data acquisition system consisted of seven 1 GHz bandwidth digitizers each possessing four channels and capable of 5 gigasamples/sec. This allowed for 28 diagnostic signals to be recorded during the experiment.

The current monitors utilized in this experiment consist of current-viewing resistors (CVRs) and large signal B-dot (magnetic induction) probes. The CVRs were located near the center of the disk, within the base of the electron collector can, and recorded the electron current at the entrance to the load cavity. The B-dot probes were distributed along the radial extent of the MITL and characterized the localized current densities along the disk. Figure 3.11 illustrates the distribution of diagnostics along the bottom of the cathode plate. An identical distribution of B-dot probes were installed along the anode plate but slightly rotated with respect to the cathode monitors. This was done to smooth out any azimuthal variations that might occur along the MITL. The specific locations of the current monitors used in this experiment are summarized in table 3.3.

Early experiments revealed the potential for field emission from the current monitors along the cathode due to non-uniformities in the surface plasma. The emitted electrons resulted in current monitor signals which were higher than the cathode current and thus underestimated the electron flow. As a result, additional current monitors were placed in circular holes and distributed between the concentric grooves of the cathode as shown in figure 3.12. To reduce the field enhancement at the edge of the current monitors these holes were constructed with rounded edges and covered in polyamide tape, figure 3.13.

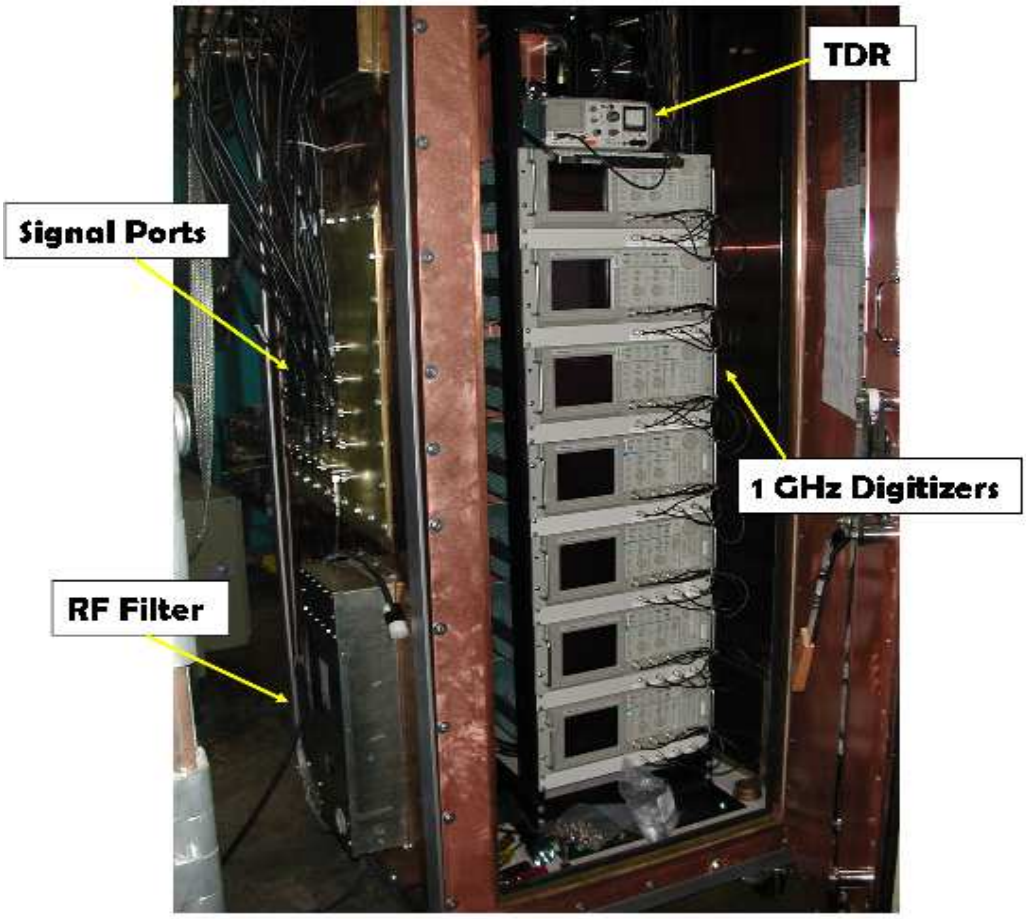

Figure 3.10: Shielded enclosure for data acquisition. Consists of seven 1 GHz digitizers and a time domain reflectometer (TDR) cable tester for measuring cable transit times.

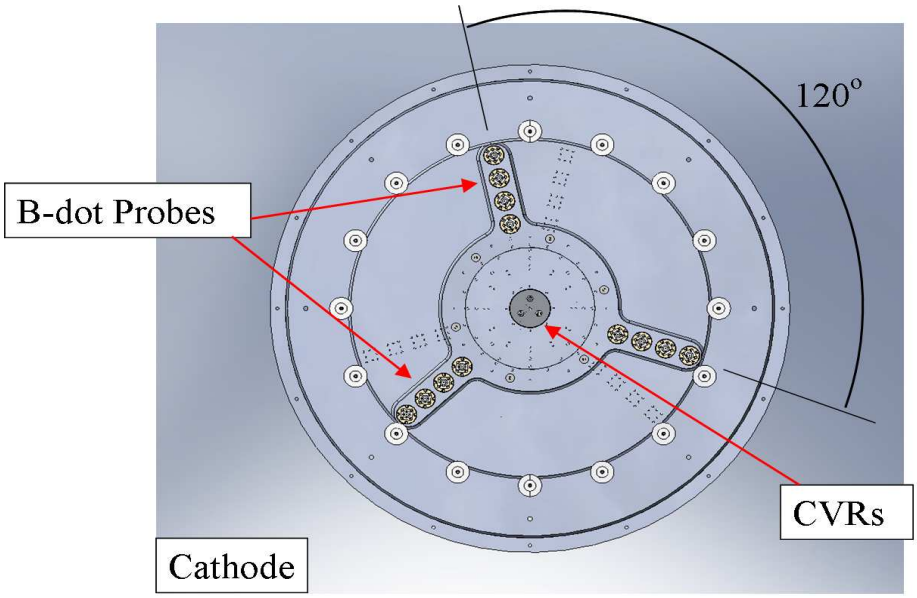

Figure 3.11: Cathode plate. B-dot diagnostics are distributed along four concentric circles. Within each circle there are three probes separated by a 120 degrees.

Diagnostic	radii(m)	Inductance(nH)	Angles(deg)
Anode B-dot	0.186, 0.240, 0.297, 0.354	53.0, 53.7, 54.5, 55.2	110, 230, 350
Cathode B-dot	0.186, 0.240, 0.297, 0.354	53.0, 53.7, 54.5, 55.2	100, 220, 340

Table 3.3: B-dot locations for each electrode. Each location is measured r meters from the center of the disk and θ degrees from the top of the plate shown in figure 3.11. The inductance is the lumped line inductance at each radial location.

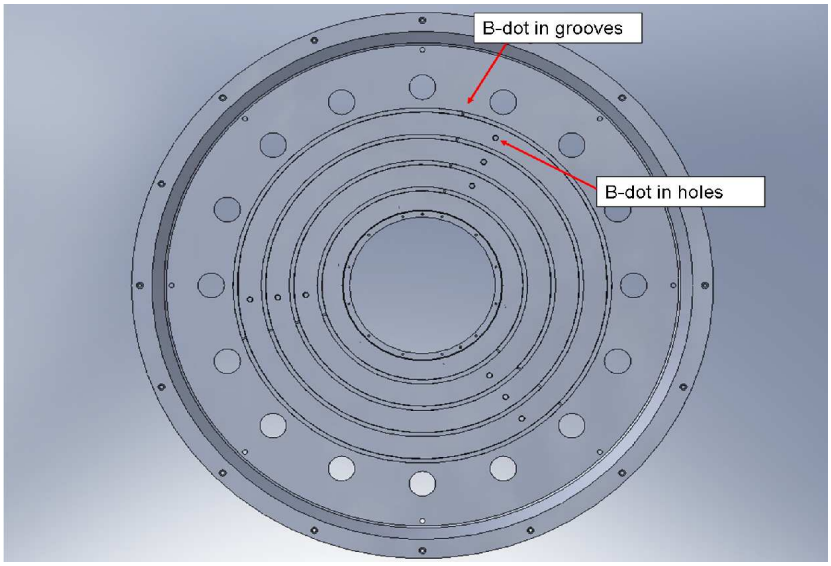

Figure 3.12: Cathode surface of A-K gap. B-dots located in grooves and holes.

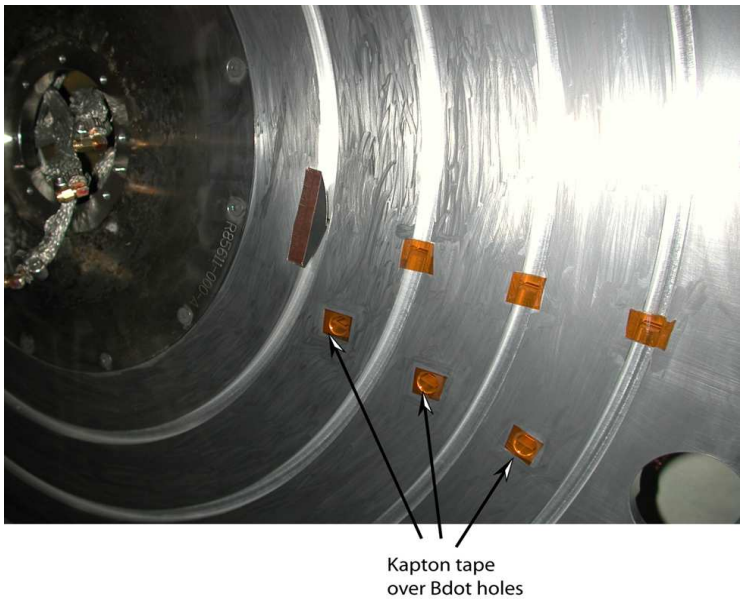

Figure 3.13: Polyamide tape used to cover B-dots on field emitting cathode.

Current-Viewing Resistors:

Local current densities can be inferred by measuring the voltage drop across a series resistor of known value. This current-viewing resistor is characterized by a small series resistance, R_s, and very low series inductance, L_s. If the inductance of the path to ground is large compared to L_s then the majority of the current will flow through the CVR for times scales on the order of $\tau \ll L/R_s$. Figure 3.14 shows the single CVR setup used for calibration. During an experimental shot, three CVRs were used through a similar base plate with resistances of 9.81 mΩ, 9.74 mΩ, and 9.89 mΩ.

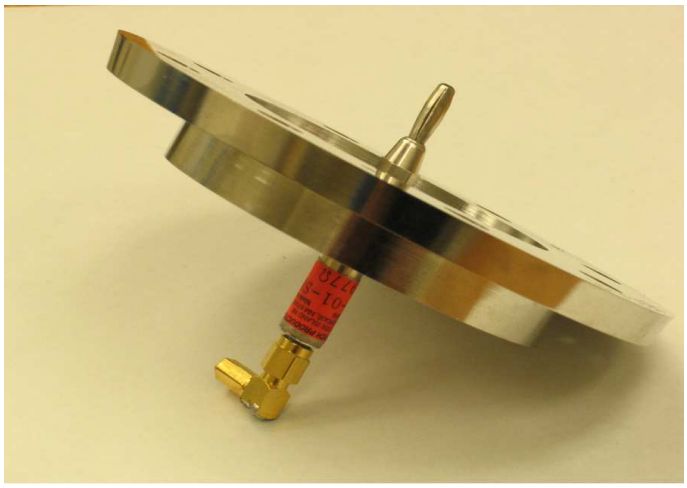

Figure 3.14: A single CVR threaded through the base plate for the calibration setup.

B-dot Probes:

The B-dot probe is an inductive sensor which measures the magnetic flux associated with current flow. It consists of a conducting loop of N turns oriented such that the cross-sectional area, A, of the loop is normal to the magnetic flux density. Current is induced in the loop by the time-varying magnetic field associated with the pulsed current. When the signal from the inductive loop is passed through

a passive integrator the output voltage can be expressed in terms of the magnetic field,

$$V_s = \frac{NAB}{RC}, \tag{3.2}$$

where B is the magnitude of the normal magnetic flux and RC is the time constant of the passive integrator circuit. If the geometry is known, the current can be extracted from the magnitude of the magnetic flux density.

For a disk transmission line, the anode and cathode currents induce a magnetic field in the azimuthal direction. In this experiment, B-dot probes are positioned within concentric grooves along the disks such that the cross-sectional area of the pick-up loop is parallel to the radial direction and perpendicular to the field. These probes consist of a single conducting loop traced on printed circuit board that is soldered to a BNC connector as shown in figure 3.15. The response time for the probe is determined by the ratio of its inductance to its series resistance. Utilizing a single turn increases the overall time response of the monitor.

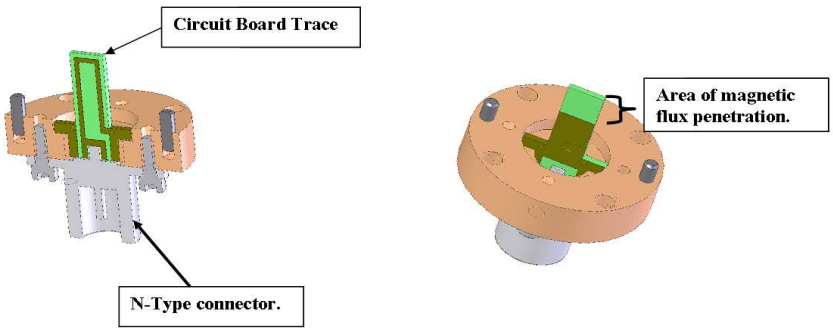

Figure 3.15: B-dot probe diagnostics. Large-signal loop current monitors measure magnetic flux along the anode and cathode.

The B-dot signals are integrated using passive components[6] once they have entered the screen box as illustrated in figure 3.16. While these integrators are fast and resilient to noise, they generate a droop in the output signal [40]. This droop must be numerically corrected through the use of software that is incorporated into the data acquisition. Once the integrated signal is obtained, the local current at each probe position can be calculated using the radial position of the current monitor and its calibration factor determined below.

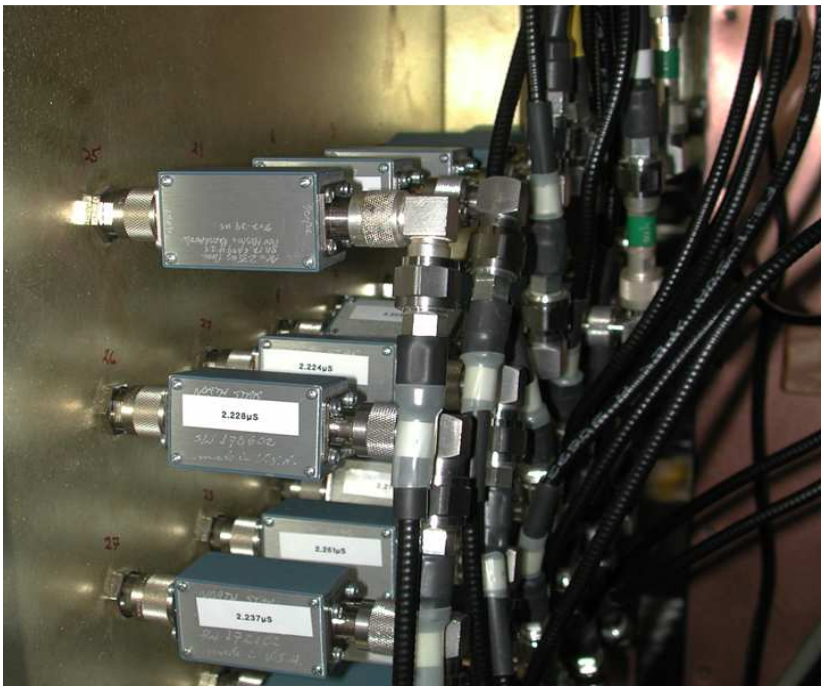

Figure 3.16: *RC* passive integrators. There is a single calibrated integrator for each of the 24 B-dot signals.

[6]This is a variant of the *RC* circuit. When the signal duration is very small compared with the *RC* time constant, the voltage drop is mainly across the resistor. The output voltage is effectively the integration of the input signal divided by the time constant.

Calibration:

At voltages well below the threshold for electron emission, a single current-viewing resistor in the base of the load will register the total current in the MITL. Comparison between the B-dot current monitors and the CVR reference signal provides a general scaling factor for each waveform. These calibration factors multiplied by the RC time constant of the passive integrators used in the screen box gives the overall gauge for each local current monitor.

The hardware assembly used for the calibration of the B-dots is given in figure 3.17. For low voltages the inner can is no longer necessary due to the absence of free electrons in the system. The center spool is thus removed and the CVR is connected directly to a calibration rod which attaches to the anode. The MITL was calibrated in place (figure 3.9) and was pulsed through the existing water lines using a 10kV pulser. This particular pulser possessed a 16 channel output which allowed $\simeq$ 10kV to be distributed through four channels per water line. The integrator circuits shown in figure 3.16 were removed and the B-dot signals were sent directly to the digitizers and integrated using numerical techniques. In order to smooth out erroneous effects, this integrated signal was integrated a second time and compared with the numerically integrated CVR signal which was used as a reference. Using a comparison algorithm, the B-dot signal was scaled and time shifted in order to minimize its difference (least squares) with the reference signal (figure 3.18). During full operation, this calibration factor along with the time constant of each of the passive integrators scales the local EMF signal generated by each B-dot probe into a local current measurement along the MITL electrodes. Subtraction of corresponding anode and cathode signals results in the local electron flow at that radial location.

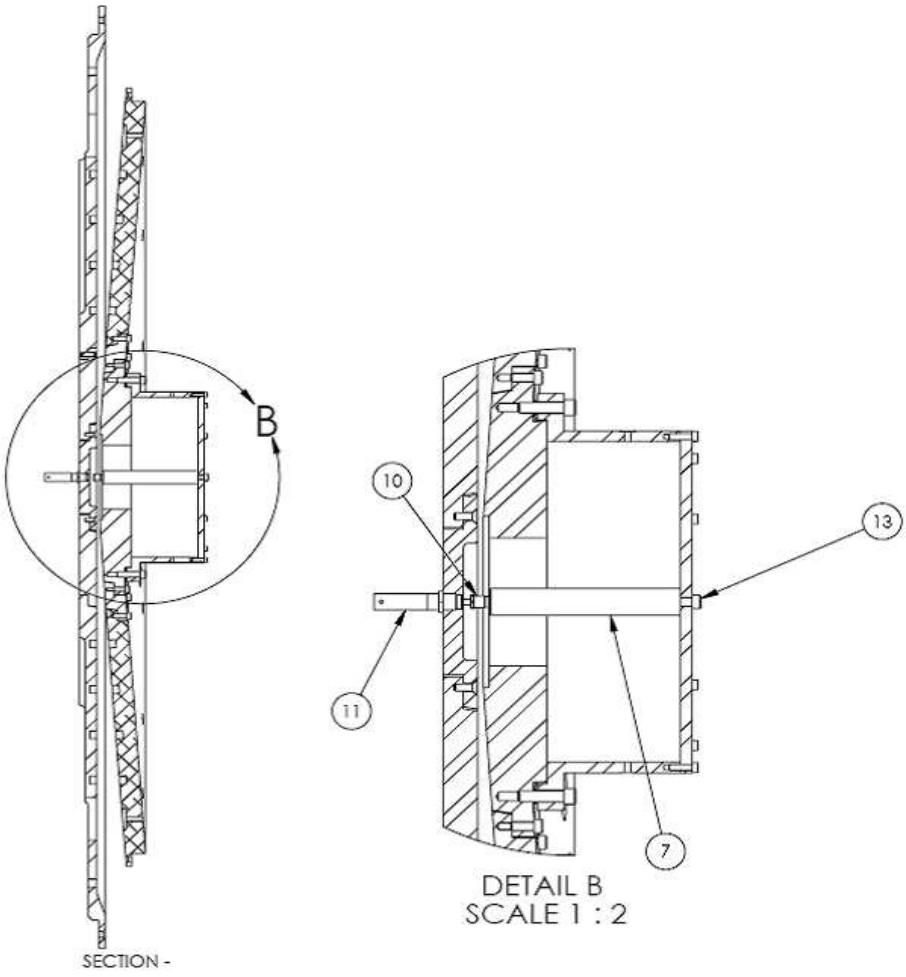

Figure 3.17: Cross-section of calibration assembly. A single current-viewing resistor is connected to the outer housing through a calibration rod which measures the total current.

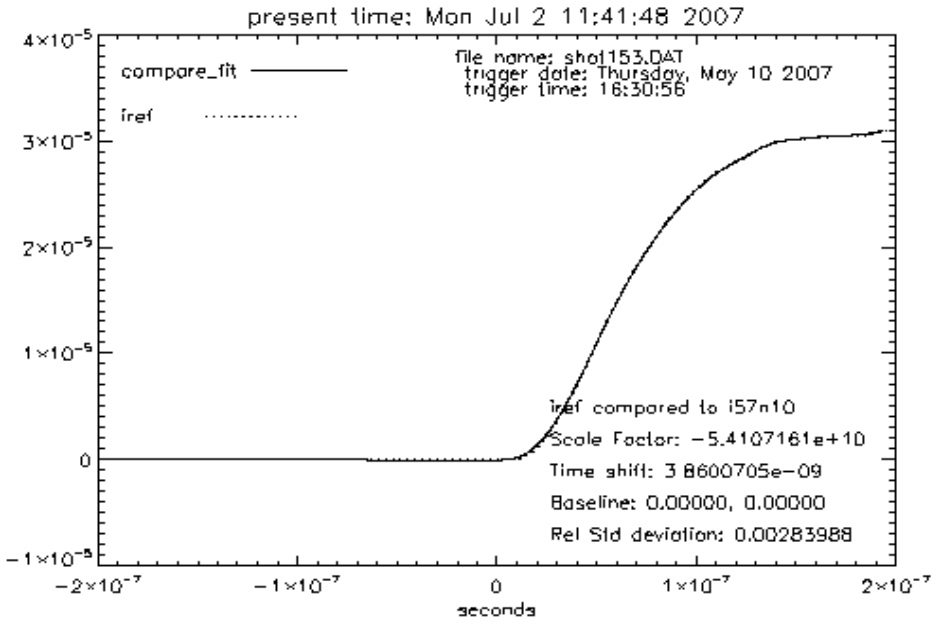

Figure 3.18: Comparison between the time integration of the CVR reference signal and twice integrated B-dot signal. For this example the calibration factor is approximately -5.41e+10 after a time shift of 3.86 ns. The negative scaling factor is a result of this particular probe's orientation along the cathode with respect to the power flow. With a relative standard deviation of roughly 0.2% the signals are nearly indistinguishable.

Chapter 4

PIC Simulation

Prior to the advent of modern high-speed digital computers, only a narrow range of practical scientific problems could be investigated due to the complexity of their geometries. From the 1920's through the mid 1960's, several numerical methods were developed which allowed for the approximation of problems that were intractable or for which closed form solutions didn't exist. With the exponential rise in computational power over the last twenty years these methods have gained immense popularity for their ability to model a variety of complex physical systems. Of these numerical methods, those utilizing finite difference approximations are more frequently used and are applicable to a broader range of applications than any other [41]. It is this finite difference method (FDM) which will provide the basis for the particle-in-cell code used in this work.

First proposed in 1955, the particle-in-cell (PIC) method [42] was developed to solve a certain class of partial differential equations which modeled nonlinear hydrodynamic phenomena. This method involved tracking several individual elements through a phase space continuum[1], while simultaneously calculating the

[1]For a collection of particles or fluid elements the 2-D phase space consists of the particle's position and velocity.

moments of the distribution on a stationary grid. The first four of these moments, where the lowest moment is numbered zero, can be interpreted as the particle density, flux density, pressure tensor, and energy flux density respectively [43].

In plasma physics applications the PIC method essentially follows the trajectories of charged particles within self-consistent electromagnetic (or electrostatic) fields computed on a fixed mesh. The electric fields in the simulation exist as a superposition of externally applied fields and internal fields arising from charge distributions. The internal field is calculated through the introduction of a non-physical grid across the area of interest which assigns a particular charge density at each grid position due to the local particle distribution. Poisson's equation is used to calculate the potentials along the grid due to this charge density which also determines the electric fields. The particle locations are then updated via the Lorentz force which depends upon the simulation particles' charge and momentum relative to the magnetic flux density.

4.1 QUICKSILVER

QUICKSILVER is a finite difference-time dependent (FDTD), three-dimensional, electromagnetic PIC code developed at Sandia National Laboratories [44]. It is capable of utilizing numerous parallel processors to simulate an extensive set of charged particle interactions. It has been used to study a variety of physical processes, such as, electron beams, high-current plasmas, microwave devices, ion and electron diodes, as well as MITLs [45]. It is currently the simulation tool of choice for studying and characterizing the MITLs in Sandia's ZR experiment.

In addition to the QUICKSILVER, several support codes which handle the preprocessing and postprocessing graphical output are utilized. An interactive preprocessor, known as MERCURY, utilizes a graphical platform to define the

simulation boundaries, conductor geometries, and meshing. MERCURY combines this information into an ASCII text file which acts as an input deck for QUICKSILVER. The simulation output is partitioned into several files using a compact machine-portable format known as Portable File Format (PFF). These PFF files are then plotted using the PFIDL post-processor [46]. Various plots of the time history data from the simulation record are possible. These include, particle snapshots containing local momentum and charge densities, field snapshots of the electric and magnetic fields within the geometry, and localized voltage and current diagnostics placed throughout the simulation.

4.1.1 Particle Creation

Within the disk transmission line, particles are introduced into the simulation near the cathode of the MITL based on a space-charge-limited (SCL) emission model [47]. As discussed in Chapter 2, the electron emission from a "cold" cathode is a complicated process that is not completely known. The detailed physics begin at a quantum level and are too small to be resolved by the simulation. In order to reproduce the desired macroscopic behavior of the system, the SCL emission model has several adjustable parameters.

The emission process proceeds as follows: Initially, the voltage pulse traveling down the line introduces an externally applied electric field, E_n, which is normal to the cathode. This value is averaged over the four values at the upper corners of a simulation cell and forces the field emission cell to "turn-on" upon reaching a predetermined threshold, *ebreakdown*. Charge is then created at the cathode surface to force the normal electric field at that point to approximately zero. A typical 2-D field emission cell along the cathode is given in figure 4.1. At each emission time

step, the charge to be introduced into the cell is computed by applying Gauss' law around the circumference of the cell. The created charge is computed by,

$$\Delta Q_{created} = \epsilon_o \Delta A E_n - \rho \Delta A \frac{\Delta x_n}{2}, \tag{4.1}$$

where ρ is the averaged charge density at the four values of the lower corners, x_n is the unit normal vector, and ΔA is the area of the cell on the cathode. The emission threshold parameters used in these simulations were determined by the electron flow data collected from the actual MITL experiment[2].

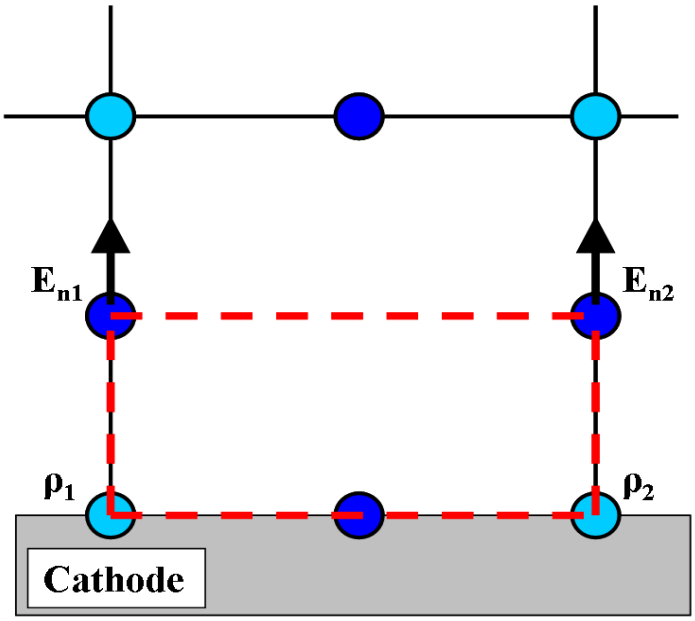

Figure 4.1: 2-D field emission cell. The normal electric field, E_o, is located at "half-grid" points which coincides with the upper corners of the emission cell.

[2]The experimental data for this dissertation is given in Chapter 6. The field emission parameter is set to the voltage level which corresponds to a sustained measurable difference between the anode and cathode currents.

The number of simulation particles created within a cell along the cathode is determined by a weighting scheme. The weights are chosen such that the number of real charged particles that the simulation particle represents adds up to the total charge computed within that cell. Each particle that is created is introduced directly on the surface of the cathode and then translated up to a height h above the surface within a time δt as in figure 4.2. The coordinates $\delta x1$ and $\delta x2$ as well as the height can be set for a random or uniform distribution within the cell compared with other particles introduced into the cell. As the particle is moved upward, the current associated with this motion is added to the accumulated current density for that cell. An incremental change in the normal electric field results from the loss of charge from the cathode and is directed toward the anode as to oppose further introduction of charge.

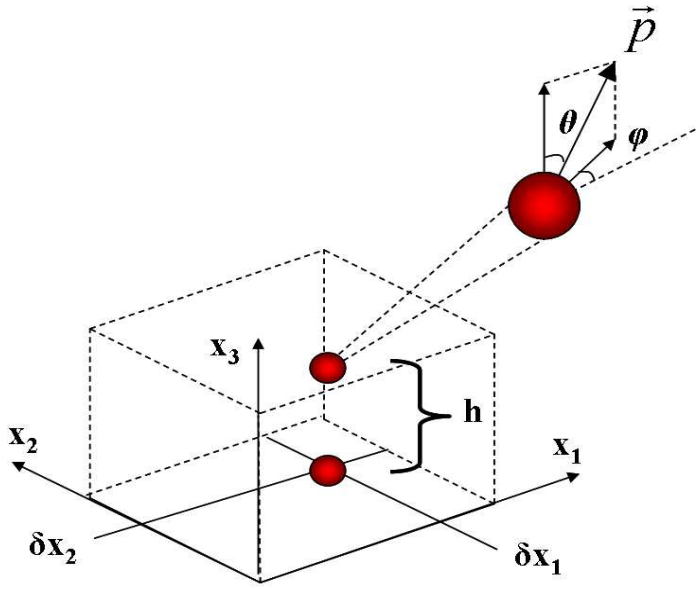

Figure 4.2: Creation of particle within a simulation cell. The momentum vector is shown in spherical coordinates. The particle's height as well as the transverse coordinates are set to a fraction of the cell size.

4.1.2 Killed Particles

The term "killed particles" refers to the flux of simulation particles passing through a surface which has been designated as a conducting region [48]. QUICKSILVER is capable of storing each particle's information as it is removed from the simulation. This data is stored within the particle snapshot file using the *KPSAVE* model and allows the information to be accessed as a simulation diagnostic. Furthermore, several parameters of the simulated particles can be used as a source for more detailed physical models of the particle interactions with the conducting surfaces. These parameters include: physical particle current, mean/standard deviation of particle energy and momentum in each direction, and mean angle with respect to the principle coordinate directions.

In addition to cataloging several physical quantities of the removed particles, QUICKSILVER also captures the spatial distribution of the electron-conductor collisions as a time-history, field-snapshot. Figure 4.3 shows the killed particle flux in the transmission line at 50 ns, just before magnetic insulation has taken place. As expected, the center section of the electron collector and the anode at inner radius possess the majority of the killed particle flux. The cathode contains much of the visible flux during the simulation; however, this is due to the return of the free electrons following there scalloped orbits[3]. Upon returning to the cathode, the electron energy is relatively low. This is confirmed through the recorded momentum and particle energy through this conductor.

The physical particle current is calculated as the total physical charge accumulated over the history time step and is very useful in determining which sections of conductor endure the largest portion of the electron collisions. This proved useful in the design of the inner electron collector, aiding in designing the lengths necessary to

[3]See section 2.2

enclose the majority of the recombining electrons. The mean/standard deviation of the particle energy and momentum were calculated from the charge-weighted sums of the simulation particles collected by the conductor.

Once the killed particles have been recorded the interactions of the electrons with the conducting boundary can be modeled. A series of coupled electron transport codes, known as *ITS*, utilizes the killed particle parameters to accurately model heating of electrode surfaces, back-scattering from bulk conductors, and electron emission through thin foils [49]. This will be covered in more detail in section 4.1.4 on energy deposition. This diagnostic was used to determine the rise in anode temperature due to electron bombardment and whether ions and neutrals are introduced into the system and play a significant role.

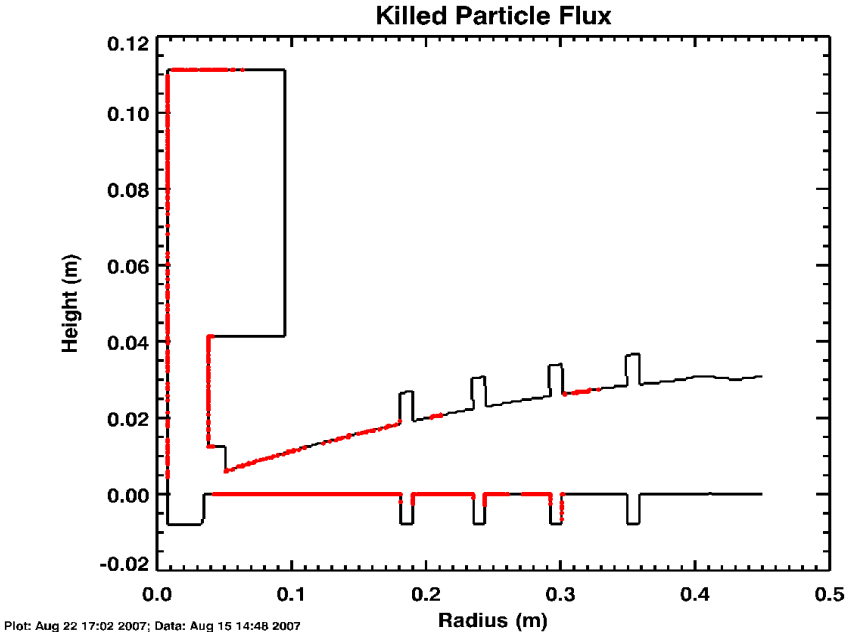

Figure 4.3: Killed Particle Flux at 50 ns.

4.1.3 Field Solvers

The finite difference method (FDM) was developed in the 1920's by A. Thom [50] and has become a very popular, albeit straightforward, method for approximating several different field problems. The FDM technique is based on the approximation of differential equations using finite difference equations. The QUICKSILVER field solver utilizes explicit and implicit leap-frogging algorithms that are based on Yee's finite difference algorithm [51]. In an isotropic medium, such as vacuum, Maxwell's curl equations, in rectangular coordinates, can be expanded into the following six scalar equations:

$$\begin{aligned}
\frac{\delta B_x}{\delta t} &= \left(\frac{\delta E_y}{\delta z} - \frac{\delta E_z}{\delta y}\right), \\
\frac{\delta B_y}{\delta t} &= \left(\frac{\delta E_z}{\delta x} - \frac{\delta E_x}{\delta z}\right), \\
\frac{\delta B_z}{\delta t} &= \left(\frac{\delta E_x}{\delta y} - \frac{\delta E_y}{\delta x}\right), \\
\frac{\delta E_x}{\delta t} &= \frac{1}{\mu_o \epsilon_o}\left(\frac{\delta B_z}{\delta y} - \frac{\delta B_y}{\delta z} - \sigma E_x\right), \\
\frac{\delta E_y}{\delta t} &= \frac{1}{\mu_o \epsilon_o}\left(\frac{\delta B_x}{\delta z} - \frac{\delta B_z}{\delta x} - \sigma E_y\right), \\
\frac{\delta E_z}{\delta t} &= \frac{1}{\mu_o \epsilon_o}\left(\frac{\delta B_y}{\delta x} - \frac{\delta B_x}{\delta y} - \sigma E_z\right),
\end{aligned} \tag{4.2}$$

where the conductivity, σ, is zero in vacuum. The space and time derivatives in equations 4.2 are converted via a central finite difference approximation which is second-order accurate,

$$\frac{\delta F^n(i,j,k)}{\delta x} = \frac{F^n(i+1/2,j,k) - F^n(i-1/2,j,k)}{\delta} + O(\delta^2) \tag{4.3}$$

$$\frac{\delta F^n(i,j,k)}{\delta t} = \frac{F^{n+1/2}(i,j,k) - F^{n-1/2}(i,j,k)}{\Delta t} + O(\Delta t^2) \tag{4.4}$$

This generates an explicit finite difference equation for each of the six scalar electric and magnetic induction field components. These spacial components of the fields are distributed about a unit cell of the Yee lattice as shown in figure 4.4 where $\vec{E}$ and $\vec{B}$ are half cells widths apart and are evaluated at alternate half-time steps.

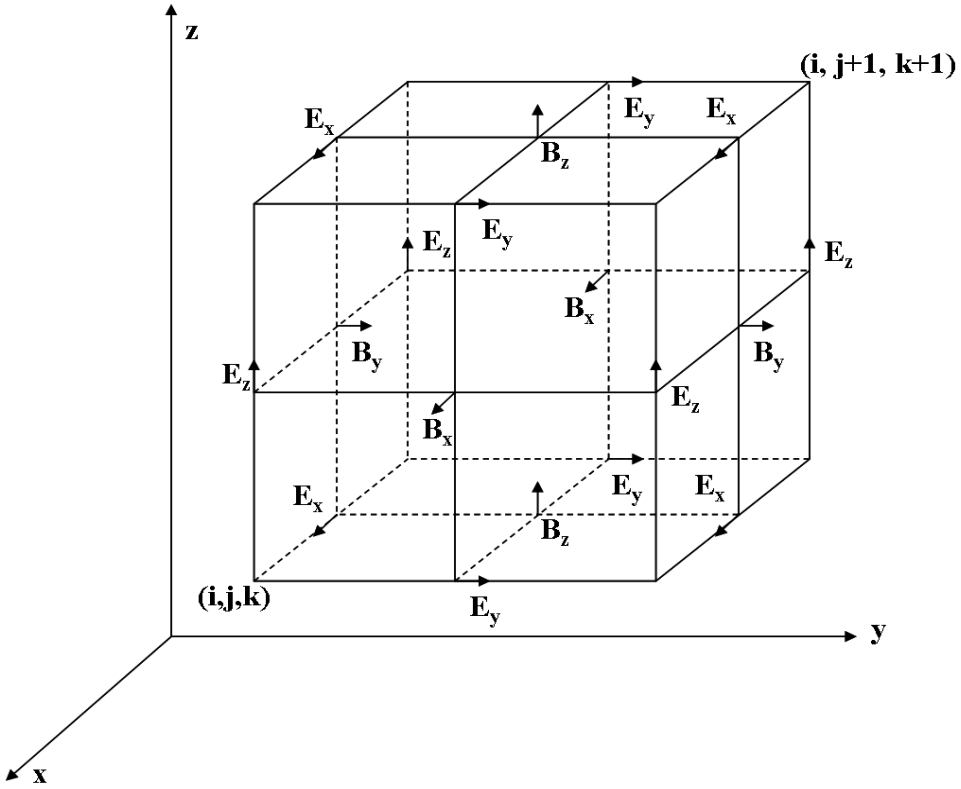

Figure 4.4: Location of the field components within a unit cell of the Yee's lattice. The electric field components are on the edges and the magnetic flux components are in the center of the faces.

For simulation cells adjacent to a conductor, boundary conditions must be applied which are appropriate for the vacuum-material interface. In this work, the anode and cathode are simulated as perfect electric conductors. The boundary conditions are applied along the boundary of a cell such that the tangential components of the electric field as well as the normal components of the magnetic field vanish at each conducting surface.

The mesh used to define the fields across the volume, must be spaced appropriately. The grid size must not allow a significant change in the electromagnetic field from one point to the next. In order to generate meaningful results, the grid spacing in any particular direction must be a fraction of the electromagnetic wavelength. Furthermore, to obtain a computational stability requires that the spacial increments must be greater than the distance traveled by light in a vacuum over that increment of time. This sets the time step for the particular grid spacing used. When charged particles are introduced into the simulation this time step also becomes dependent on the relative magnitude of the magnetic field. For very large magnetic fields the particle orbits become very small due to a reduction in the cyclotron period. This requires a reduction in the simulation time step and a potential refinement in the grid meshing.

The finite difference method is easily adapted to cylindrical or spherical coordinates by applying the appropriate coordinate changes to equations 4.2. Cylindrical coordinates were used for the study of the transmission line disk geometry. In this case the diagnostic grooves can be considered infinite in extent, in the $\hat{\phi}$ direction, so as to reduce the problem to two dimensions. Assuming an approximate uniform current distribution, the three dimensional fields can be easily generated from the model while obtaining faster computational turn around.

4.1.4 Energy Deposition

In order to develop an accurate computational model for the transmission line gap, the effect of cathode field emission on the anode surface must be considered. Early in the pulse, electrons are free to transit the smaller gap sections of the disk and bombard the anode. This increase in electron energy deposition into the anode, leads to a rapid nonuniform increase in temperature along the surface. Several experiments have demonstrated a correlation between the formation of an anode plasma with the specific heat of the anode material [52, 53]. This suggests that electron heating can lead to an avalanche breakdown of adsorbed gases from the anode due to thermal desorption. Sanford *et al.* measured the electron energy deposition in tantalum, titanium, and carbon anodes and found that, independent of the anode material, anode plasma formation required surface temperatures of 400 °C ± 60 °C.

The surface of the anode considered in the experimental setup is composed of two separate material sections. At inner radius, $r \leq 0.34$ m, the anode surface is defined by a stainless steel insert plate which connects with the steel outer housing of the load cavity. The remaining 86.34% of the anode surface consists of aluminum to reduce the overall weight of the plate. Because the aluminum section of the radial MITL is further away from the load it posses a larger gap spacing, greatly reducing its susceptibility to significant energy deposition. On the other hand, the stainless steel section of anode at inner gap becomes a critical design parameter due to the excessive electron bombardment early in the pulse.

Studies of the electron-anode interactions of applied-B ion diodes using PIC simulations [54] led to the further development of temperature and scattering diagnostics within QUICKSILVER. *ITS* coupling models allow for a more detailed modeling of electron-conductor interactions (ECI) using the stored killed particle diagnostics from the simulation. Using a data table, defining the specific ECI for

a particular conductor material, the energy deposition, $Q(E_i, \Theta_j)$ in Mev/cm, for incident electron energies and angles can be obtained. The temperature increment due to a single incident particle of charge, q, passing through a conducting surface of area ΔA is calculated as,

$$\Delta T_p = \frac{100 q Q(E_p, \Theta_p)}{\rho C_p(T) \Delta A} \tag{4.5}$$

where q is the charge in Columbs, ΔA is the area in m^2, ρ is the density in gcm^{-3}, C_p is the specific heat in J $^{\circ}\mathrm{C}^{-1}$ g^{-1}, and Q is the energy deposition in MeV $\mathrm{cm}^{-1}/electron$ ($Q/e = 10^{-6}$ J cm^{-1}/C).

The conductor temperature is recorded as an auxiliary snapshot field and stored at discrete time steps throughout the simulation. Since the temperature of the anode surface is an accumulative effect, later field snapshots will result in the highest temperatures recorded on the anode surface. Initial simulation runs utilizing actual voltage waves from previous experimental shots revealed that the largest anode temperatures found were located at the radius of minimum gap spacing as shown in figure 4.5. This geometry for this particular simulation was designed for a substantial reduction in inner radial electron flow and possessed a minimum gap spacing of 6 mm. In this particular case, it was found that the rise in anode temperature never exceeded ≈ 200 $^{\circ}$ C which is well below the threshold for anode plasma formation [55].

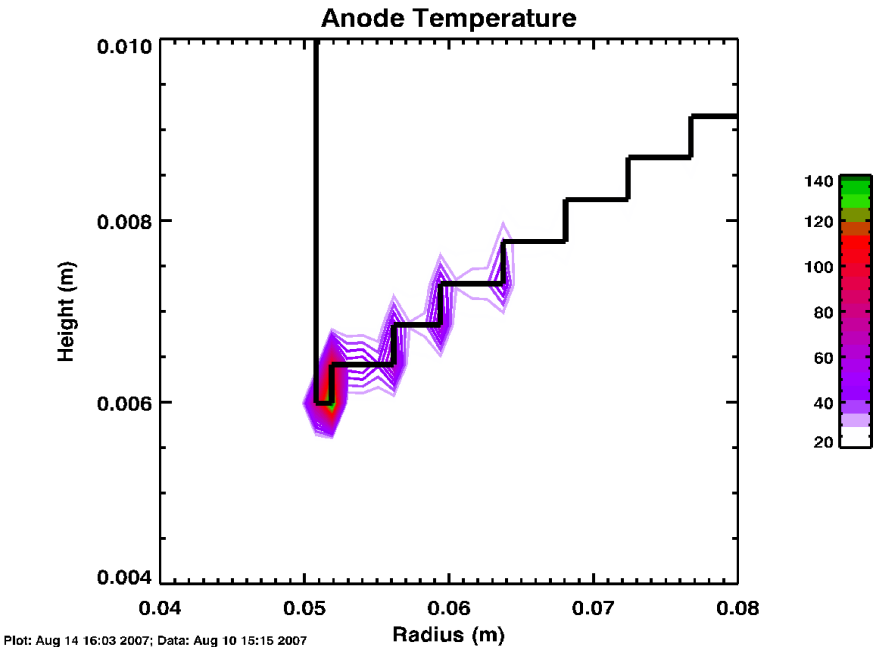

Figure 4.5: Temperature contours in ° C along the anode conductor at $t = 89.5$ ns. The baseline was set to 20 ° C for room temperature.

4.2 Simulation Diagnostics

There are two main time history diagnostics provided by QUICKSILVER that will be utilized in this study. The *HISTORY* command specifies parameters for field and particle time history diagnostics. Measurements based upon the field snapshots are listed in table 4.1. These "virtual" diagnostics can be placed anywhere within the simulation to record local voltages, current, energy flux, etc. Within the disk transmission line geometry, these current probes will be placed at each of the physical B-dot locations as well as in between the grooves for generating radial electron flow plots. The current and localized voltage measured at each of the B-dot positions provides confirmation that the probes are at the same potential as the simulation.

Similarly, the inductance at these positions can be verified when the particle emission model is turned-off to ensure that the current rise-times are comparable.

Type	**Components**	**Comment**
field	*ei, ej, ek*	components of electric field at a point
	bi, bj, bk	components of magnetic induction at a point
	ji, jj, jk	components of current density at a point
	rho	charge density at a point
dl	e, b	voltage ($E \cdot dl$), current ($B \cdot dl$)
da	e, b	surface integral of normal electric/magnetic field
	j, s	surface integral of normal current density/Poynting vector
dv	*rho/energy*	total charge/field energy
	eenergy/benergy	electric/magnetic field energy

Table 4.1: Time history field diagnostics.

The initial voltage pulse is introduced to the system through an inlet section of transmission line which is matched to the outer radius of the disk. This open-circuit voltage pulse is created from actual shot data recorded from the experiment and is equal to twice the amplitude of the forward voltage wave in the system. This waveform is digitized and entered into the simulation using a voltage include file and provides the forward voltage wave for the excitation of the simulated structure.

In addition to the simulation field diagnostics, QUICKSILVER provides time history particle snap shots. The total number of simulation particles as well as their energy and charge are recorded at several time intervals. The software categorizes each recorded particle as either created, killed, or as a particle that remains in the simulation. Several particle parameters are recorded with each snap shot such as directional momentum, charge, position, etc.

4.2.1 Inductance

The radial dependent self-inductance of the transmission line is an important parameter which determines the amount of magnetic flux induced across the line by the current pulse. At any particular distance from the load the lumped inductance is the scaling factor between the localized voltage at that point and the time change in current measured along the anode. Due to the relatively large size of the load collector region to the rest of the transmission line, the majority of the line inductance is located at the minimum radius of the anode profile. This leads to a measured difference of about 2 nH between the inner most current monitors and those located at the furthest radial extent. Therefore, the measured voltages at each B-dot location are rather close and decrease with smaller radii. The lumped inductance at each B-dot location was calculated using the Quicksilver diagnostics[4] for the anode current

[4]This was done in the absence of charged particle emission from the cathode.

and the electric field distribution across the transmission line,

$$L = \frac{\int \int V dt}{\int I dt}. \tag{4.6}$$

Here V is the local electric potential at the location of the current monitor and was derived from the line integral of the electric field across the gap. The inductances of the B-dot probes along with that of the load are included in the radial profile given in figure 4.6. This profile represents the total inductance of the MITL, including the load cavity, for a given radius, $r \geq r_o$. At the minimum gap spacing, r_o, the inductance is just that of the load cavity, $L = 50$ nH.

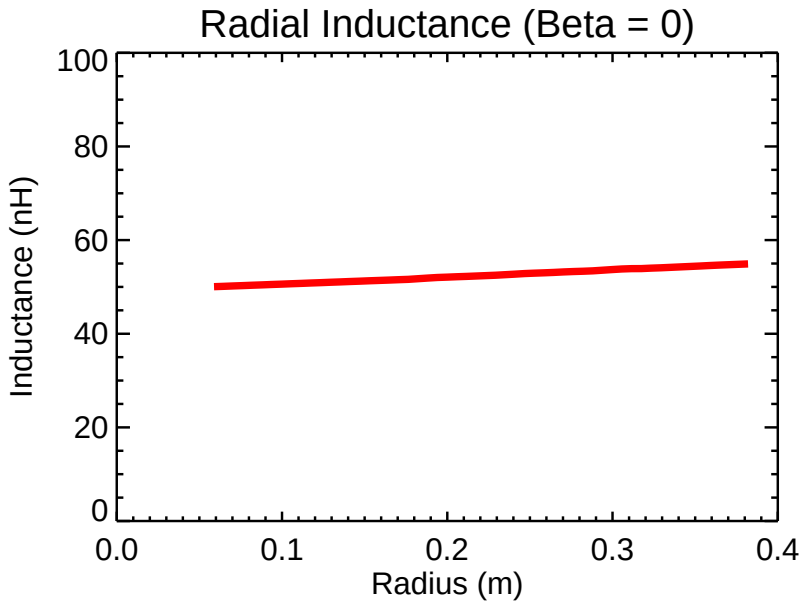

Figure 4.6: Lumped inductance at the entrance to the load cavity and each of the four B-dot probe radial locations.

Figure 4.7 compares the radial inductance profiles of two separate re-trapping parameters, β. These profiles do not include the load cavity and therefore only represent the lumped inductance between the anode and cathode within the A-K gap at a particular radius. Because the gap spacing of each geometry must be equal at outer radius, the minimum gap must change the fractional electron flow at the load. The minimum gap must be raised in order to increase the re-trapping rate of the radial MITL. The minimum gap of the $\beta = 3.7$ geometry was about 2.22 mm higher than the constant flow geometry. This lead to the increase in self-inductance shown in figure 4.7.

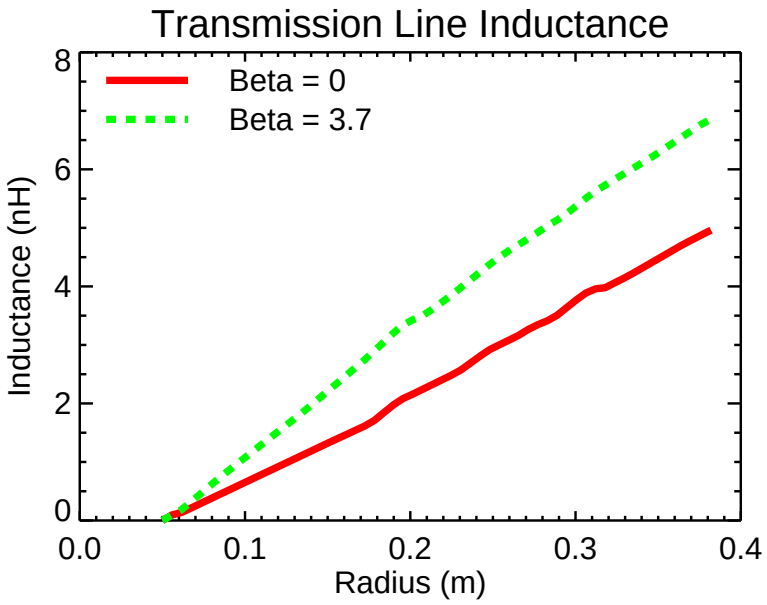

Figure 4.7: Lumped inductance at the entrance to the load cavity and each of the four B-dot probe radial locations.

4.2.2 Field Measurements

The collective behavior of the electron flow is greatly affected by the electric and magnetic fields in the A-K gap of the transmission line[5]. Using the field snap-shot diagnostics, QUICKSILVER is capable of constructing contour plots of these fields on any of the principle axes at a variety of time intervals throughout the power pulse. The voltage input pulse generated at the power inlet of the simulation defines the initial electric field profile across the A-K gap. As electrons are emitted from the surface of the cathode, this field is altered by the existence of space charge along the negatively charged electrode as shown in figure 4.8. The current associated with the power pulse establishes a magnetic inductance within the line which is perpendicular to the electric field. A contour of the magnetic flux density in the $\hat{\theta}$ direction at peak voltage during a standard simulated pulse is given in figure 4.9.

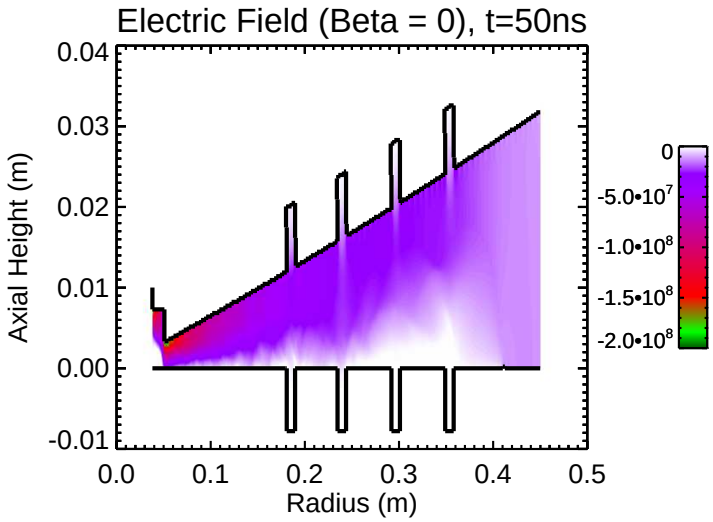

Figure 4.8: MITL electric field in the $\hat{z}$ direction. The electric field strength is diminishing throughout the space charge and is zero along the cathode.

[5]Chapter 2

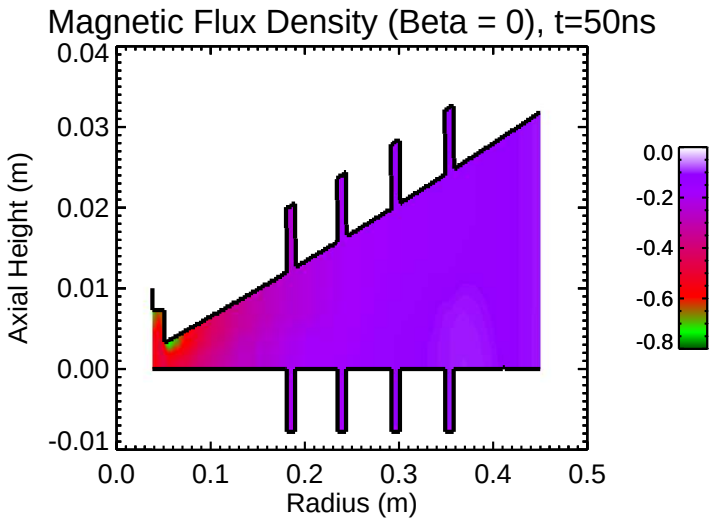

Figure 4.9: Magnetic flux density within the MITL. The field is negative indicating that it is in the $-\hat{\theta}$ direction.

The recorded fields within the simulation allow for the development of voltage and current diagnostics. Voltages are obtained by simple line integrals of the electric field,

$$V = \int \vec{E} \cdot d\vec{l}, \tag{4.7}$$

where dl is an infinitesimal line segment of a path running across the A-K gap which is perpendicular to both the anode and cathode. A contour of the voltage is illustrated in figure 4.10. Similarly, the current is obtained by line integrals of the magnetic flux divided by the permeability of free space (i.e. Ampere's Law in vacuum).

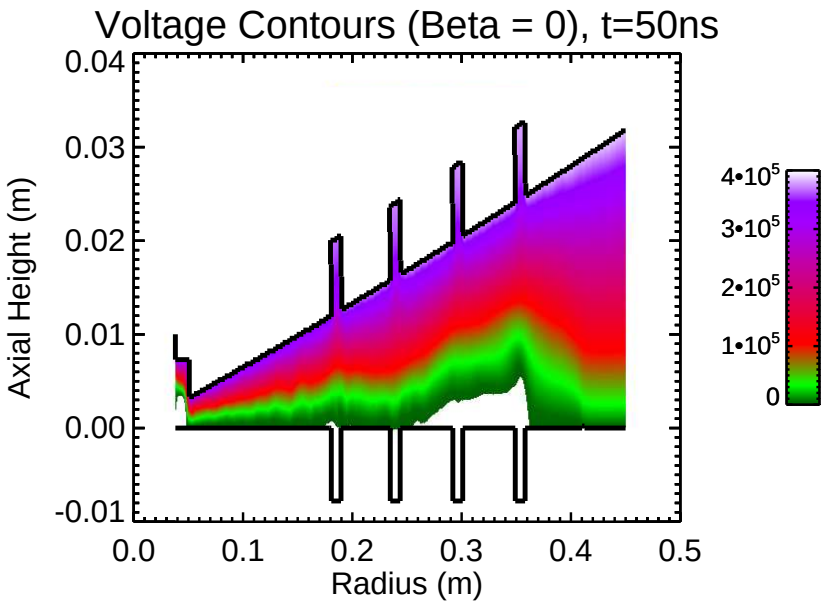

Figure 4.10: Voltage contours within the A-K gap. The potential is between the anode and the top of the space charge layer.

The electron charge density can be determined through the application of an inverse weighting scheme on the simulation particles that are currently in the system. The weights which correlate the amount of charge to the density of simulation particles was introduced upon the particles creation as covered in section 4.1.1. This spatial density is stored as a field-snapshot at discrete moments of time as shown in figure 4.11. These field snap-shots are useful in the construction of movies which can be used to illustrate the collective dynamics of the electrons during insulation.

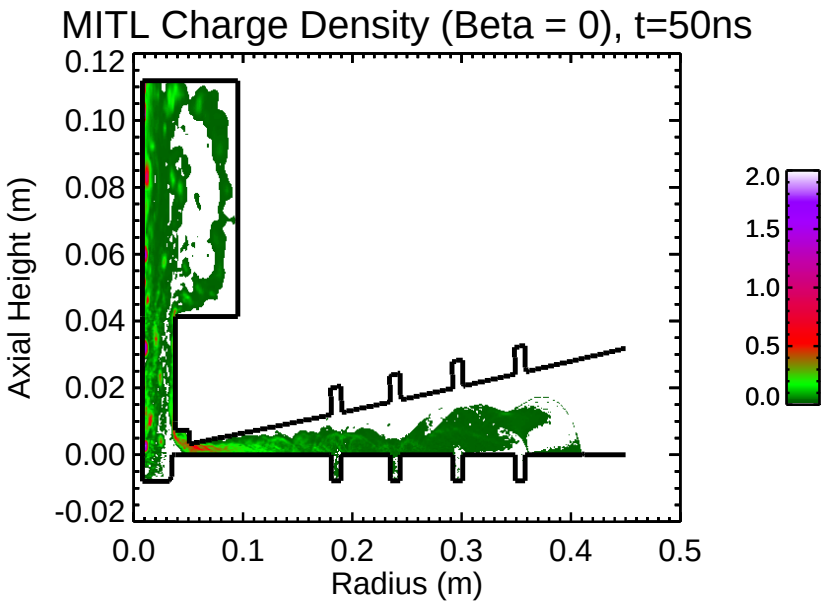

Figure 4.11: MITL charge density prior to full magnetic insulation.

4.2.3 Electron Flow Current

Assuming that losses in the disk transmission line are negligible, the current constituted by the average free electron drift along the cathode is equal to the difference measured between the anode and cathode currents. These currents are initially equal prior to the formation of space charge until the insulation process results in a drop in the cathode current through electron emission. The localized voltage at a particular position in the MITL is dependent on the self-inductive scaling of the time change in anode current. As this potential decreases along with the falling edge of the current pulse, the electric field diminishes across the A-K gap. This allows the cathode current to once again rise up to the anode level. During voltage reversal the average electron drift, which was originally in the direction of power flow, approaches zero and shifts directions to flow radially outward from the center of the MITL. If the negative cycle of the potential is large enough then the

anode and cathode experience a role reversal.

In the PIC simulations, the local voltage and current are obtained through line integrals of the calculated fields. This is done at several locations distributed throughout the MITL as well as those corresponding to the physical B-dot locations themselves. A typical measurement of the local voltage and line currents at the inner B-dot diagnostic is shown in figure 4.12. There is good separation between the currents between 35 ns and 70 ns which correlates to the time interval for magnetic insulation. By subtracting Ia and Ic in figure 4.12, the time dependent electron flow current at the inner B-dot location is determined, figure 4.13.

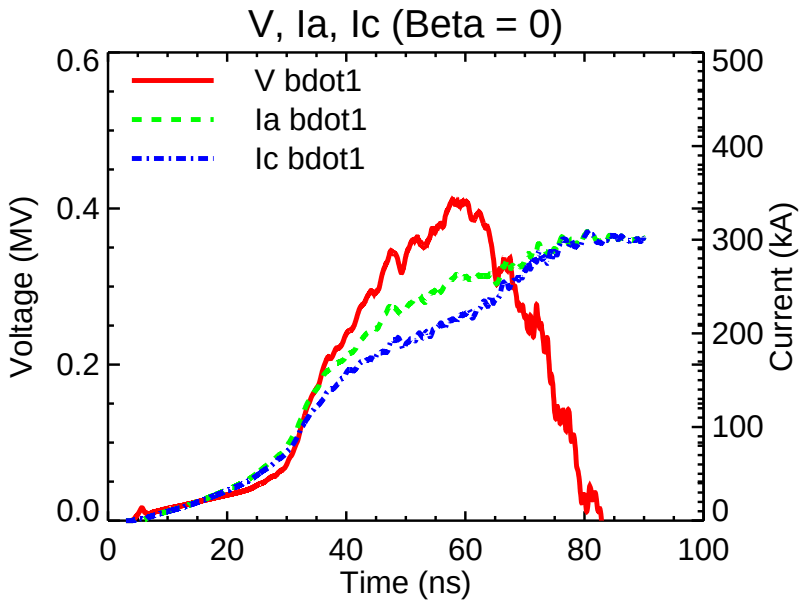

Figure 4.12: Simulated voltage across the A-K gap located at the outer most B-dot probe.

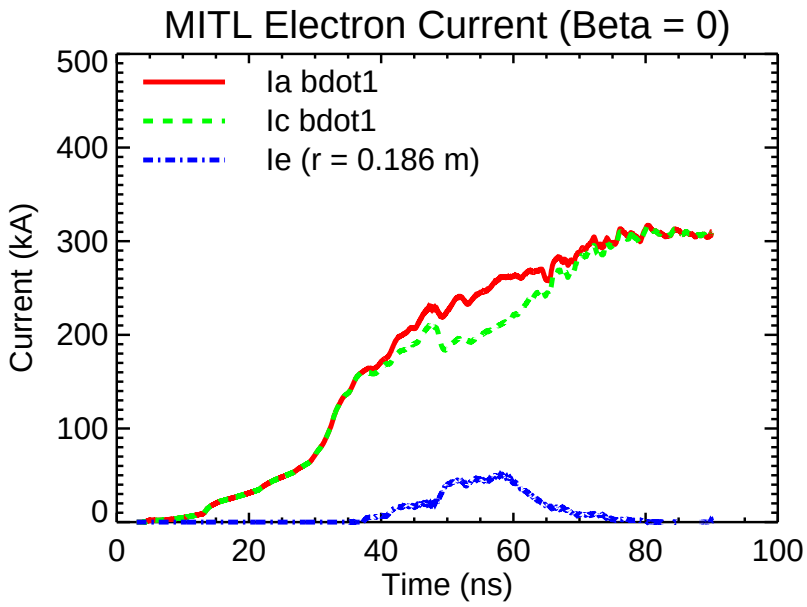

Figure 4.13: Simulated electron flow current measured by the inner B-dot diagnostic.

Chapter 5

Simulation Results

Two dimensional particle-in-cell simulations were conducted for several different electron flow profiles ranging from constant flow, $\beta \simeq 0$, to greatly reducing flow, $\beta > 3$. Several aspects of the disk MITL's performance were investigated in order to attain a fundamental understanding of the limitations inherit to the design of gap profiles from fractional electron flow considerations. Charge density contour plots, combined with the localized voltage and line currents, facilitated in the establishment of a time window for the magnetic insulation. The radial electron flow could then be examined throughout the evolution of the insulation process along with the electric and magnetic flow impedances. Further investigation into electron energy deposition along the surface of the anode offered insight into the design of the inductive load cavity and possible plasma closure considerations. Finally, magnetic flux and charge density contours provided a clear picture on the effects of perturbations within the electron sheath due to the diagnostic grooves along the cathode.

The radial electron flow model derived in section 2.5.1 was developed under the assumption that the electron layer was confined closely to the cathode during magnetic insulation and therefore the anode current was substantially greater than

the electron flow. In order to verify this model each profile was simulated at very high voltage in order to reduce the effect of space charge. With a relatively low load impedance, compared with the vacuum line impedance, the resulting current driving the line is capable of creating the would necessary magnetic insulation to meet this criteria. Radial electron flow plots from these simulations were compared against theoretical model predictions at several times during the insulation process, providing a region of validity for the model. Later simulations were driven at a much lower voltage pulse which was constructed from a previous shot by the pulse power driver used on the experimental setup. While the radial profiles from the experimental hardware are useful in studying the space charge effects at lower electric field strengths, the high voltage simulations become invaluable in developing design techniques for large z-pinch drivers which operate at voltages well over a megavolt[1].

5.1 Radial Electron Flow

The conductor geometries for the following simulations are assumed to be symmetrical in the azimuthal direction and extend radially outward from the load to the inlet of the transmission line feed, as shown in figure 5.1. The MITL region of the simulation consists of the A-K gap between the curved anode and flat cathode conductor boundaries and their grooves which represent the current monitoring diagnostics of the experiment. The load cavity consists of the entire volumetric region of the electron can inside the outer housing. Due to the CVR diagnostics, the inner can could not be represented in a two dimensional geometry and therefore was not included. The entire cavity, however, represents the lumped load inductance and is the only load structure necessary for defining the electron flow in the MITL.

[1]The refurbished Z driver at Sandia National Laboratories is designed to have an insulator stack voltage of about 4.5 MV.

The simulations were conducted on the "Koopa" computer cluster at Sandia National Laboratories in Albuquerque, NM. The simulations typically ran on 16-32 processors and incorporated a maximum of one million simulation particles. The highest cell concentration in the simulation grid is positioned along the cathode and throughout the grooves of both electrodes. A finer mesh along the emitting surface provides a higher resolution of the electron sheath which contains the largest density of simulation particles. This meshing was extended up to the anode diagnostic grooves to obtain the most accurate results possible at those locations. Because there were no direct measurements recorded from the load cavity during the simulation, this region consisted of a sparser mesh for reduced computing time. The cell sizes near the surface of the cathode and within the grooves were set to 200 μm.

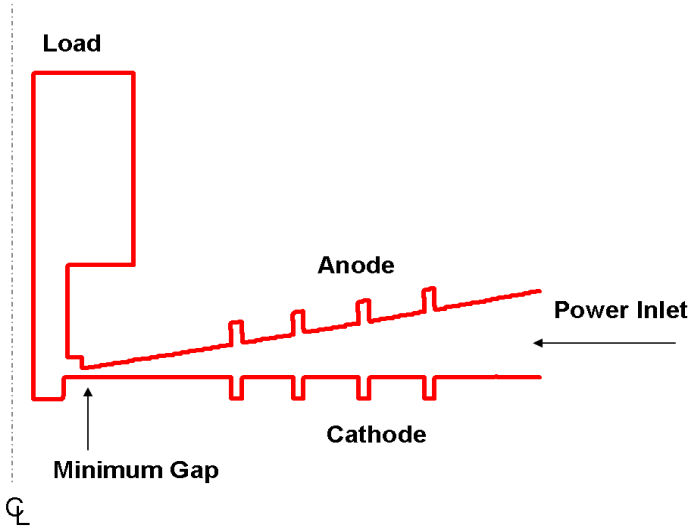

Figure 5.1: Conductor geometry for radial disk MITL simulation.

The boundary conditions at the inlet feed were generated from an experimentally derived forward-traveling waveform (shot 500) which had a peak voltage around 500 kV. For the high-voltage simulation this waveform was amplified by a factor of

ten to obtain a open-circuit voltage waveform of about 10 MV[2] In order to satisfy the Courant-Friedrichs-Lewy condition[3], the time steps for the 10 MV and shot500 simulations were set to 208.3 fs and 625 fs respectively. The decreased time step for the high voltage simulation was also necessary to obtain the proper resolution of the cyclotron period within the load cavity region due to its extremely large local magnetic flux density which was calculated to be roughly 40 T.

The following subsections provide a detailed record of three separate profile simulations. These simulations include the constant flow profile, $\beta = 0$, a reducing flow profile, $\beta = 1$, and a very large radially increasing electron flow profile, $\beta \simeq 3.7$. This wide range in re-trapping parameters, β, was necessary to construct a comprehensive picture of the radial electron flow near different operating regimes. To facilitate in the validation of the electron flow model used, each simulation profile was performed for each voltage feed, (i.e. 10 MV and shot500). Snapshots are included of the charge density inside the MITL section at a time prior to full insulation and later at peak insulation. The centroid of the charge and current densities are overlayed onto the early snapshot. During peak insulation these centroids tend to converge for well insulated transmission lines. The flow impedances defined by these centroids are given as fractions of the vacuum impedance and illustrate the amount of insulation achieved in the line and the amount of relative space charge along the cathode at peak insulation. Finally, the radial electron flow is given along with a theoretical comparison which utilizes the local anode voltage and line currents directly from the simulation. The theoretical comparison is derived from the full space charge pressure-balance model given in equation 2.19. The voltage and currents from each simulation are plotted separately.

[2]Quicksilver uses an open-circuit voltage waveform as the input to the transmission line inlet. This waveform is obtained by doubling the forward-traveling pulse.

[3]This is a restriction on the maximum time step to ensure convergence in the algorithms for solving discrete partial differential equations. The time step must allow sufficient time for the particle information to propagate through the space discretization.

5.1.1 Constant Electron Flow, $\beta = 0$

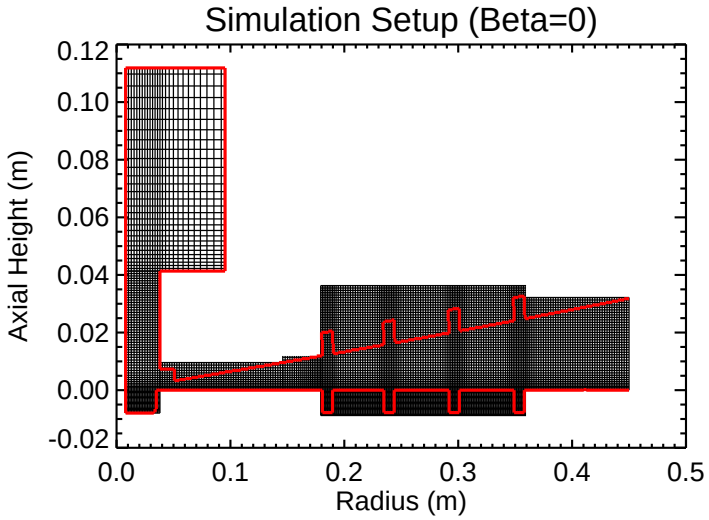

Figure 5.2: Simulation setup for constant electron flow profile. The transmission line feed inlet is positioned at $r = 0.45$ m. The minimum cell size is 200 μm and is located along the cathode.

The simulation setup for the constant flow profile, $\beta = 0$, is given in figure 5.2. At high voltage the MITL was at peak insulation around $t = 53$ ns. A charge density snapshot prior to insulation, $t = 35$ ns, is given in figure 5.3. The spread in the electric and magnetic flow impedances, figure 5.4, illustrates the distance the electron sheath extends into the A-K gap. Because electrons travel faster as they approach the anode, the centroid of the current density is further away from the cathode than that of the charge density. This results in a magnetic flow impedance which is noticeably less than the electric flow impedance. The electron flow versus radius is plotted in figure 5.5. The simulation appears to be very close to the theoretical value. It should be noted that the profile is not quite level because insulation, and thus a constant electron flow, has still not yet been achieved. The radial line voltage and corresponding line currents at this time are given in figure 5.6.

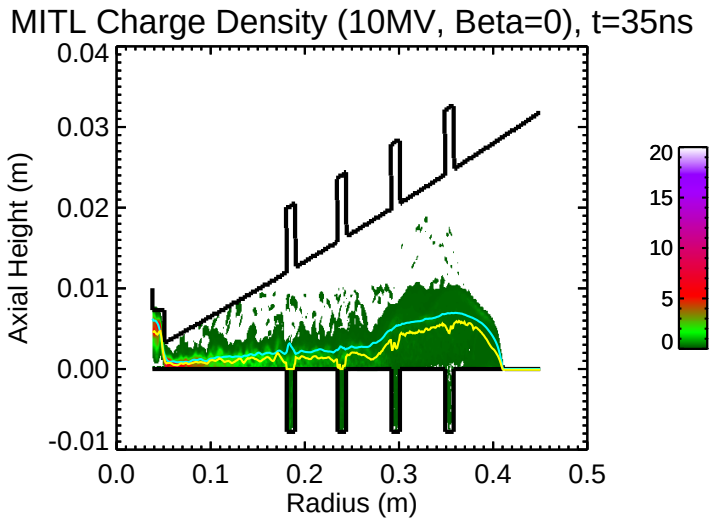

Figure 5.3: Charge density at $t = 35$ ns for the constant radial flow MITL with 5 MV forward voltage wave. The centroid for the charge density is shown below the centroid of the current density.

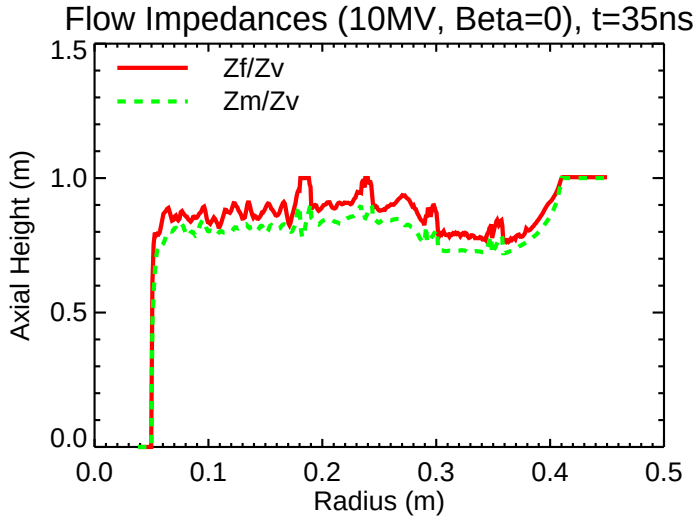

Figure 5.4: Electric and Magnetic flow impedances at $t = 35$ ns, high-voltage.

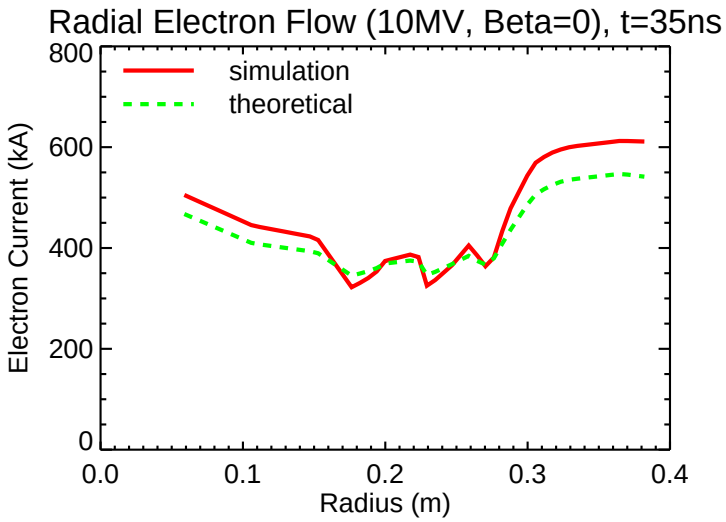

Figure 5.5: Radial electron flow at $t = 35$ ns for the constant radial flow MITL with 5 MV forward voltage wave. Prior to insulation the profile has not yet leveled out.

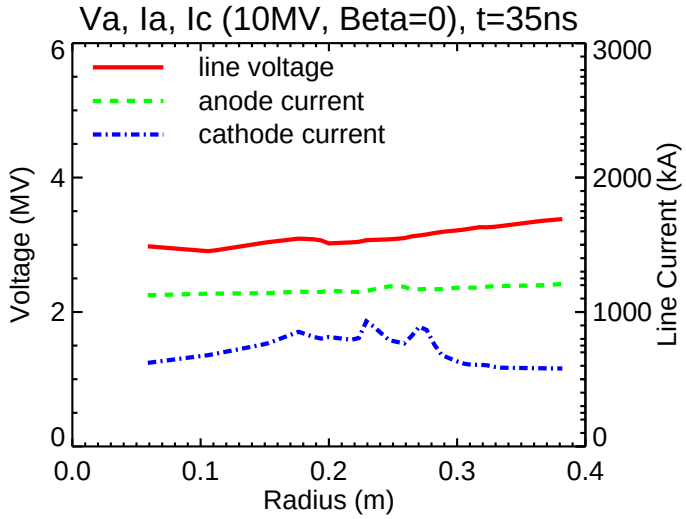

Figure 5.6: Line voltage, anode current, and cathode current plotted versus radius at $t = 35$ ns, high-voltage.

At 53 ns the majority of the charge density, figure 5.7, is confined to a small sheath along the cathode surface. The electric and magnetic flow impedance are now converging and are collectively moving toward the overall vacuum impedance of the line as shown in figure 5.8. The electron flow, given in figure 5.9, is now characterized by a constant radial profile at a magnitude of approximately 270 kA. This value represents the average separation between the anode and cathode currents which are illustrated in figure 5.10.

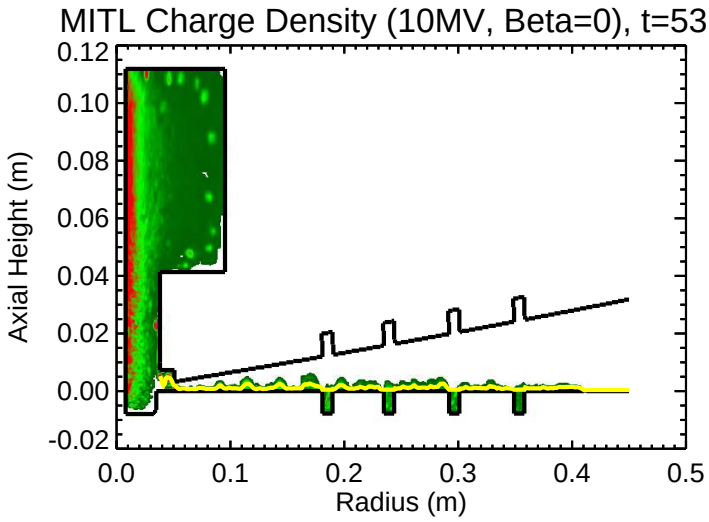

Figure 5.7: Charge density at $t = 53$ ns for the constant radial flow MITL with 5 MV forward voltage wave. The centroids for the charge and current densities approximately overlay.

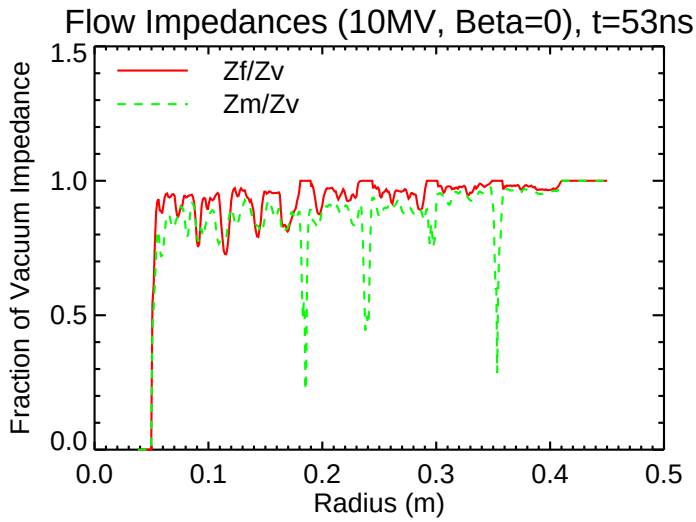

Figure 5.8: Electric and Magnetic flow impedances at $t = 53$ ns, high-voltage.

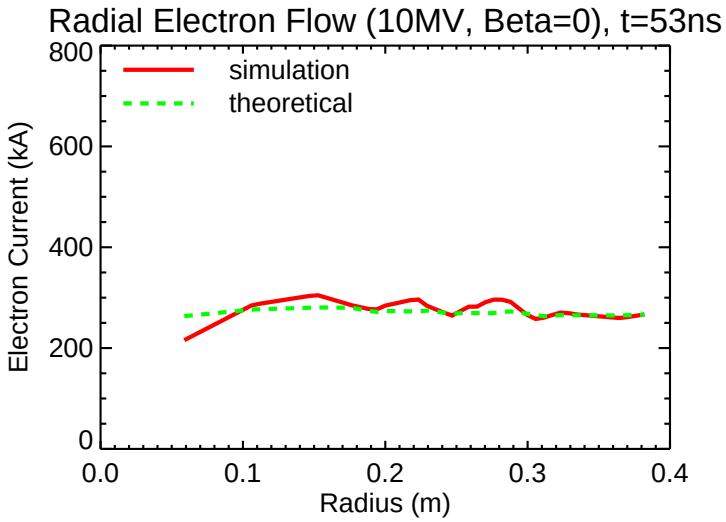

Figure 5.9: Radial electron flow at $t = 53$ ns for the constant radial flow MITL with 5 MV forward voltage wave. During insulation this profile is approximately constant with respect to radius.

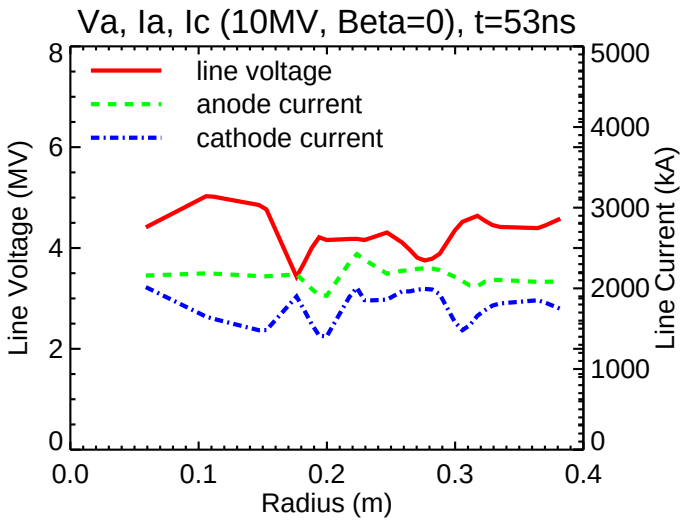

Figure 5.10: Line voltage, anode current, and cathode current plotted versus radius at $t = 53$ ns, high-voltage.

At lower voltage the simulated results and the electron flow model begin to diverge. The voltage forward wave fed into the transmission line inlet was around 500 kV and possessed the same exact shape, and therefore timing, of the high voltage waveform used. Figure 5.11 gives the MITL charge density at 50 ns which is roughly 10 ns before the time of peak insulation. Because the line voltage is significantly lower than in the previous case, emission from the cathode becomes more localized. The sharp diagnostic grooves along the cathode possess a much lower emission threshold due to their field enhancement. As the voltage level rises these are the first regions to begin freely emitting electrons into the A-K gap. As these charged particles are driven back to the cathode due to the magnetic flux in the line, their orbits are fairly large due to the line current operating at a level close to saturated flow. These electrons are capable of shielding other parts of the electron surface, further delaying their emission. Because the line is fairly under-insulated, it is never able to overcome this feature of the cathode surface. This results in the noticeable curvature present

in the radial flow impedance profiles given in figure 5.12.

The radial electron flow is shown in figure 5.13. While the simulation is in close agreement with the theoretical values throughout the middle of the MITL, at larger radius the voltage is still too low to insulate the line. Below $r = 0.1$ m the theoretical value cannot be resolved due to inadequate insulation which violates the pressure-balance assumption used in the model. The line voltage and electrode currents used in the theoretical model are given in figure 5.14.

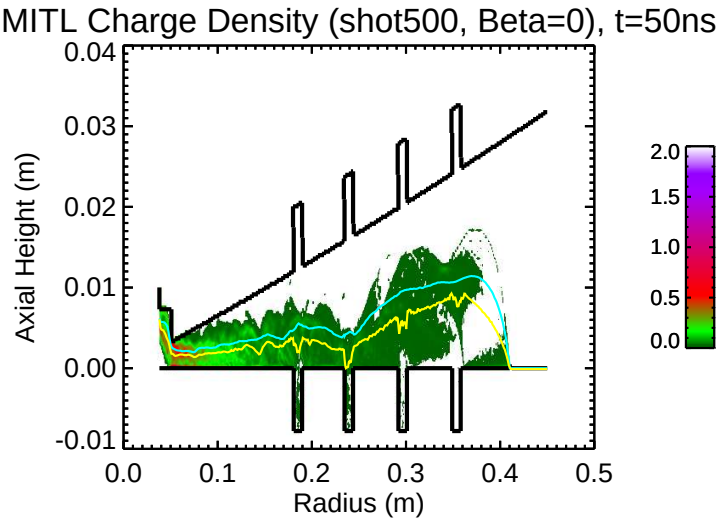

Figure 5.11: Charge density at $t = 50$ ns for the constant radial flow MITL with 500 kV forward voltage wave. The centroid for the charge density is shown below the centroid of the current density.

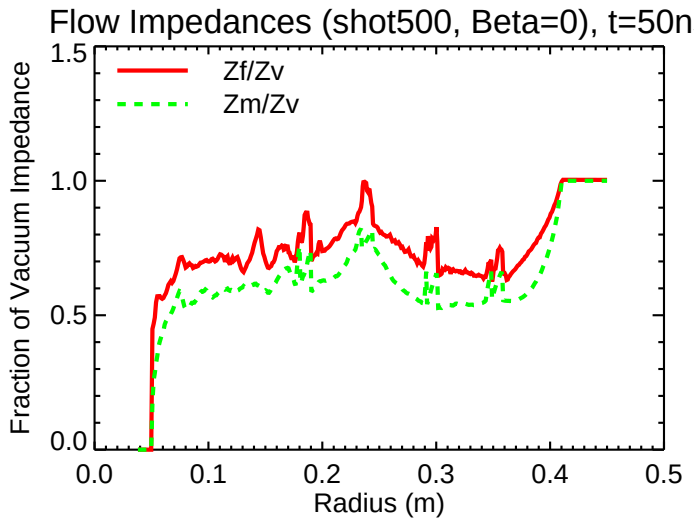

Figure 5.12: Electric and Magnetic flow impedances at $t = 50$ ns, low-voltage.

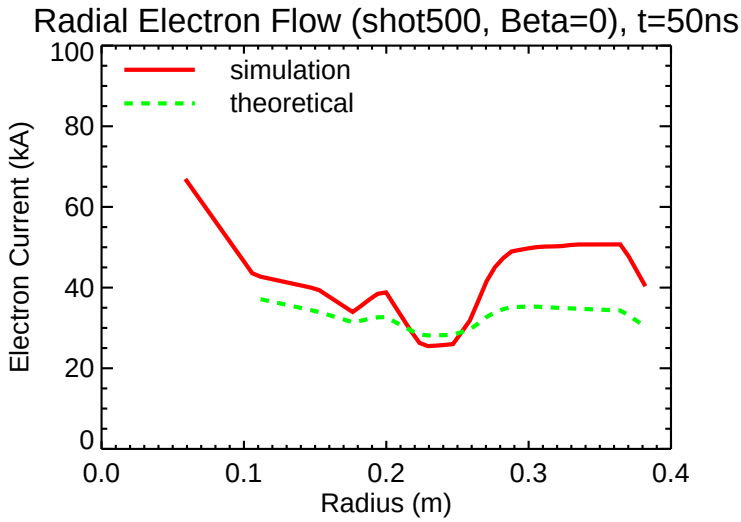

Figure 5.13: Radial electron flow at $t = 50$ ns for the constant radial flow MITL with 500 kV forward voltage wave. Prior to insulation, the theoretical value predicted by the pressure-balance model cannot resolve the electron flow below a radius of 10 cm.

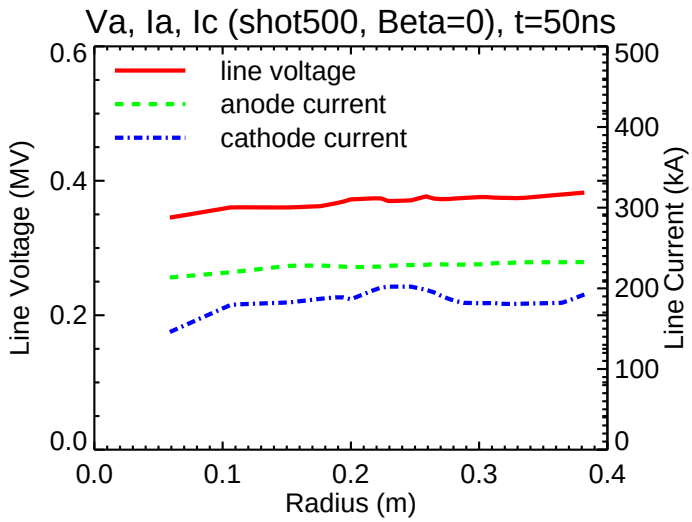

Figure 5.14: Line voltage, anode current, and cathode current plotted versus radius at $t = 50$ ns, low-voltage.

At peak insulation, $t = 60$ ns, the charge density, figure 5.15, reveals that the electron sheath still extends far into the A-K gap. The current drawn by the MITL is incapable of heavily insulating the line and the space charge along the cathode accounts for a much greater fraction of the entire line voltage, which is apparent when comparing figures 5.16 and 5.17. The space charge correction for these simulations were calculated using pressure-balance theory, section **??**,

$$V_{SCC} = \frac{m_e c^2}{2e}\left(\left(\frac{I_a}{I_c}\right)^2 - 1\right), \tag{5.1}$$

where $\frac{m_e c^2}{2e} \approx 255 \times 10^3$, $\frac{I_a}{I_c}$ is determined from simulation diagnostics, and the charge density near the cathode is assumed to be uniform in the axial direction. At t =60 ns the space charge in the 500 kV simulation constitutes 37.9% of the total line voltage across the A-K gap. In contrast, the space charge in the high voltage simulation at peak insulation, $t = 50$ ns, only contributes to 2.27% of the total potential.

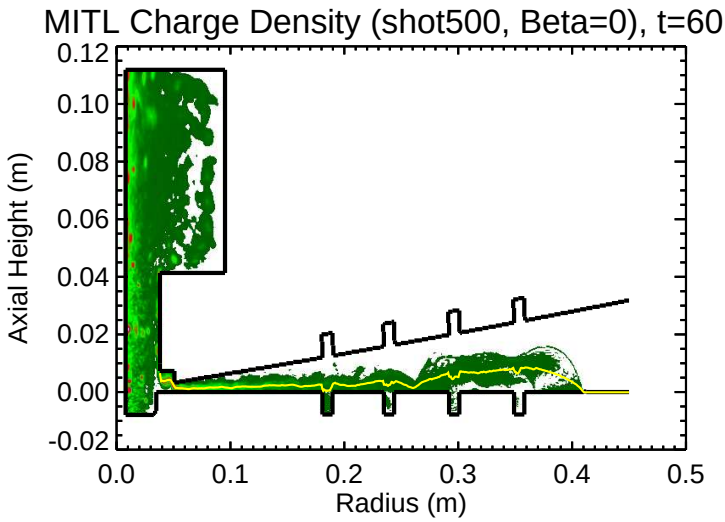

Figure 5.15: Charge density at $t = 60$ ns for the constant radial flow MITL with 500 kV forward voltage wave. The centroid for the charge density is shown.

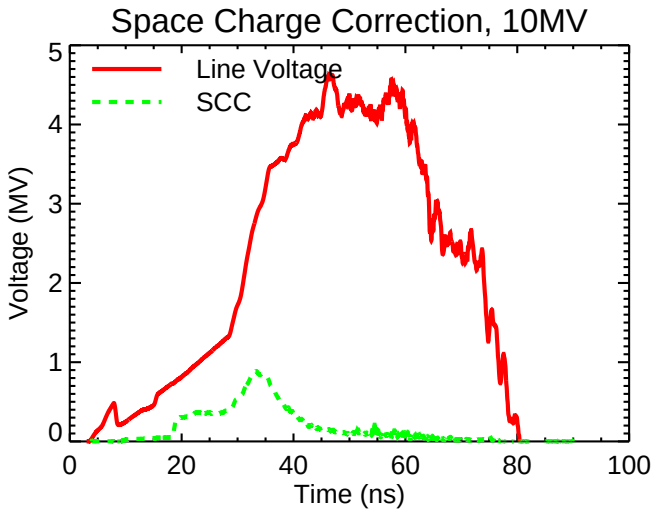

Figure 5.16: Comparison between the full line voltage and the space charge correction term predicted from pressure-balance theory, high-voltage.

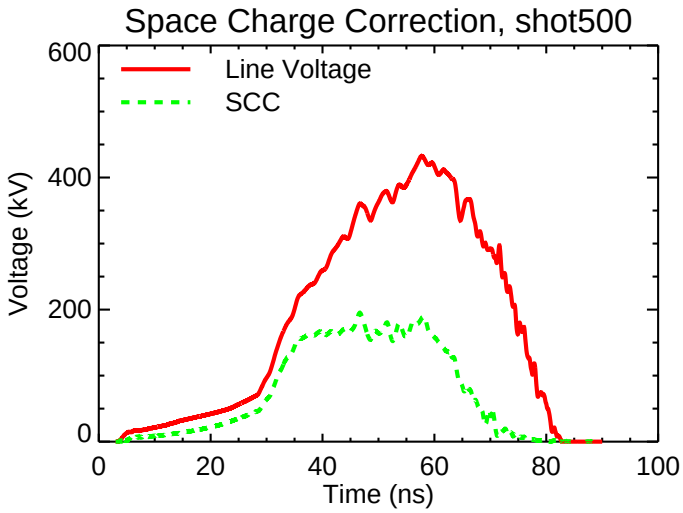

Figure 5.17: Comparison between the full line voltage and the space charge correction term predicted from pressure-balance theory, low-voltage.

The flow impedances, figure 5.18, are more level during peak insulation, however, their ratio to the vacuum line impedance is still much less than unity. Due to the amount of space charge in the A-K gap, the electric and magnetic flow impedances never converge as they do in the high voltage case. The radial electron flow, figure 5.19, has become closer to the constant theoretical curve. Because the theoretical model assumes a substantially larger line voltage, the curves tend to disagree at larger radii where the gap spacing is largest and thus the electric field strength on the cathode surface is weakest. This results in an nonuniform emission near the power inlet of the transmission line. The line voltages and currents for this simulation are displayed in figure 5.20.

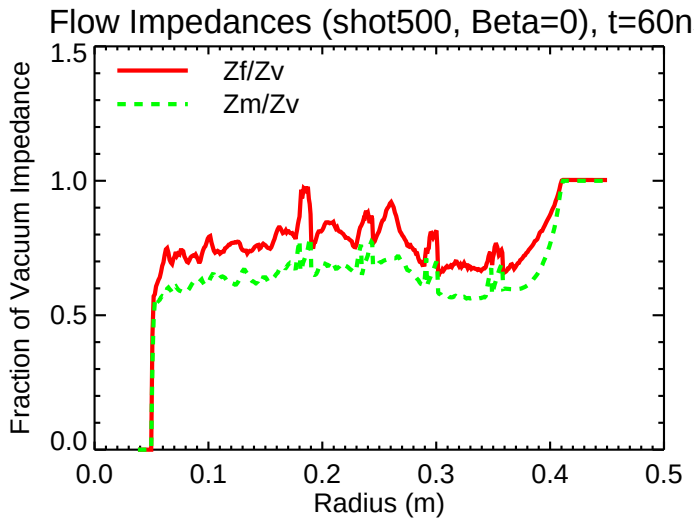

Figure 5.18: Electric and Magnetic flow impedances at $t = 60$ ns, low-voltage.

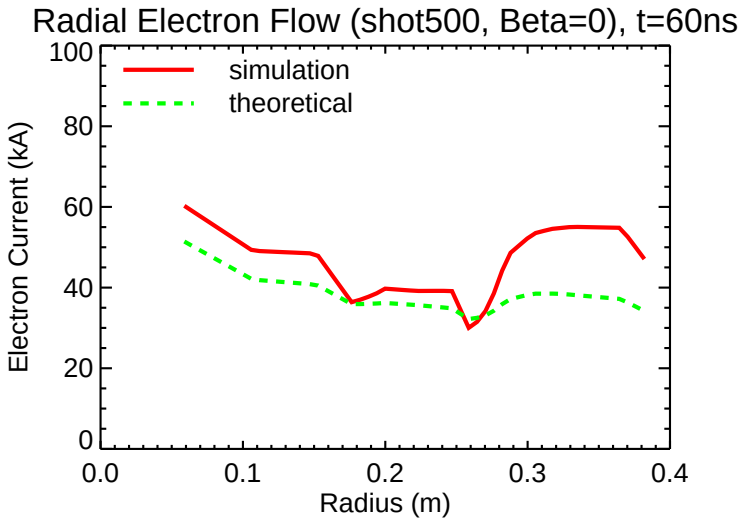

Figure 5.19: Radial electron flow at $t = 60$ ns for the constant radial flow MITL with 500 kV forward voltage wave. During insulation the radial electron profile is approximately constant with respect to radius.

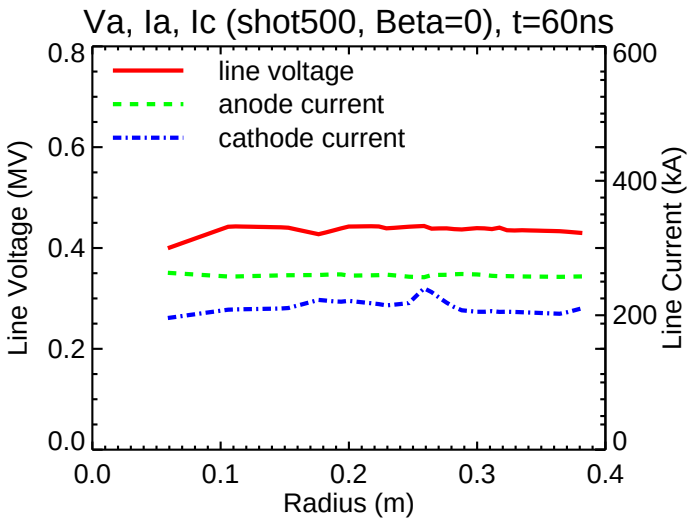

Figure 5.20: Line voltage, anode current, and cathode current plotted versus radius at $t = 60$ ns, low-voltage.

5.1.2 Reducing Electron Flow, $\beta = 1$

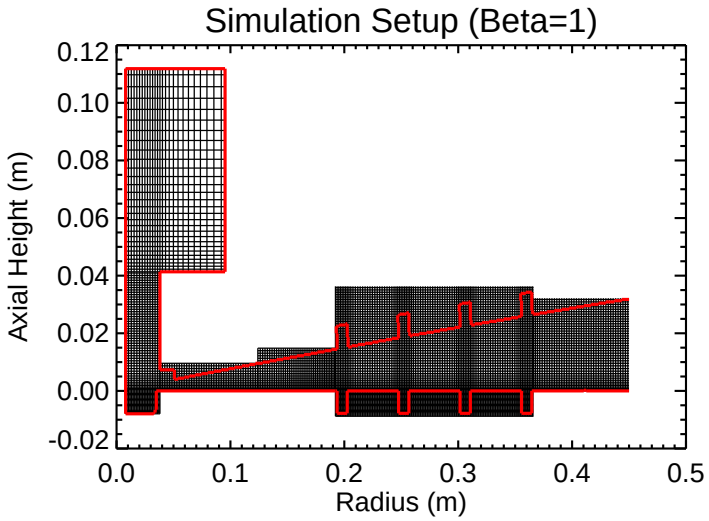

Figure 5.21: Simulation setup for the $\beta = 1$ reducing electron flow profile. The transmission line feed inlet is positioned at $r = 0.45$ m. The minimum cell size is 200 μm and is located along the cathode.

The simulation setup for the reducing flow profile, $\beta = 1$, is given in figure 5.21. At high voltage the peak insulation time was around $t = 50$ ns. Charge density snapshots within the MITL at $t = 40$ ns and $t = 50$ ns are given in figures 5.22 and 5.23 respectively. Just as the case was for the constant profile at high-voltage, the centroids of the charge and current density converge as peak insulation is achieved. The flow impedances are shown in figures 5.24 and 5.25 respectively. As the transmission line becomes magnetically insulated the magnetic flow impedance advances toward the electric flow impedance and their ratio to the vacuum line impedance approaches unity. As the space charge is driven in the direction of the cathode, the diagnostic grooves are filled with more electrons. This drives the centroid of the current density downward toward the grooves resulting in the lowered spikes seen in the plot of magnetic flow impedance given in figure 5.25.

The theoretical value derived from the electron flow model is not well defined beyond the period of magnetic insulation. Figure 5.26 shows a good correspondence between this value and the simulated waveform out to about a radius of 23 cm where the increase in radial flow cannot be resolved. During insulation, figure 5.27, the model and the simulation appear to be in good agreement and are characterized by a reducing radial electron flow. The voltage and line currents at these times are given in figure 5.28 and 5.29 respectively.

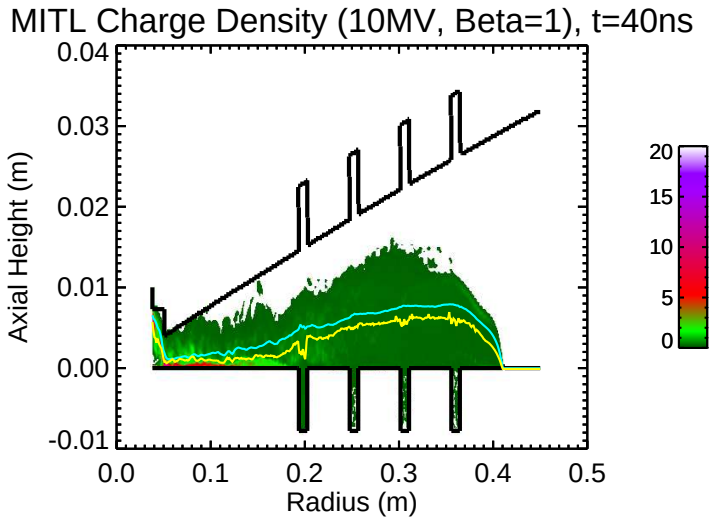

Figure 5.22: Charge density at $t = 40$ ns for the constant radial flow MITL with 5 MV forward voltage wave. The centroid for the charge density is shown below the centroid of the current density.

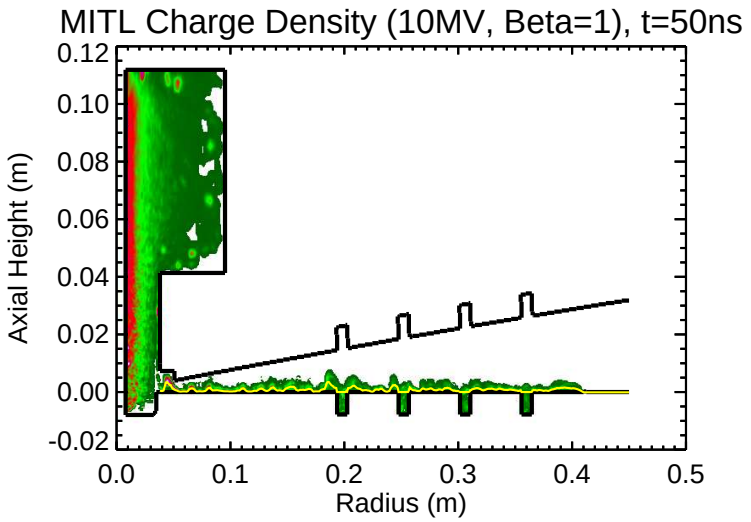

Figure 5.23: Charge density at $t = 50$ ns for the constant radial flow MITL with 5MV forward voltage wave. The centroids for the charge and current densities approximately overlay.

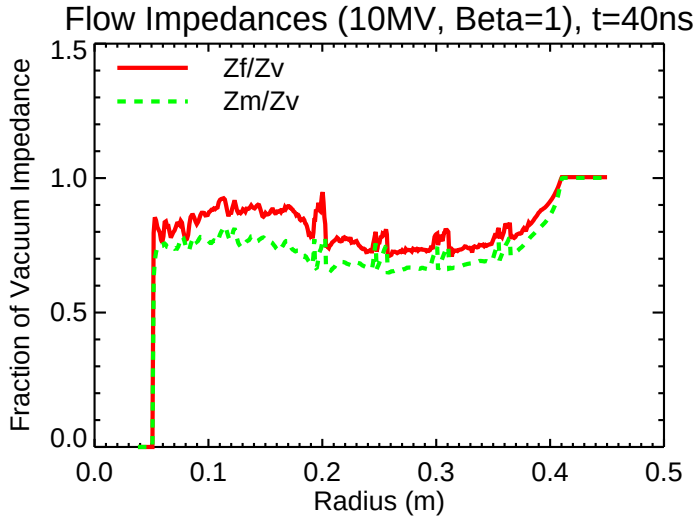

Figure 5.24: Electric and Magnetic flow impedances at $t = 40$ ns, high-voltage.

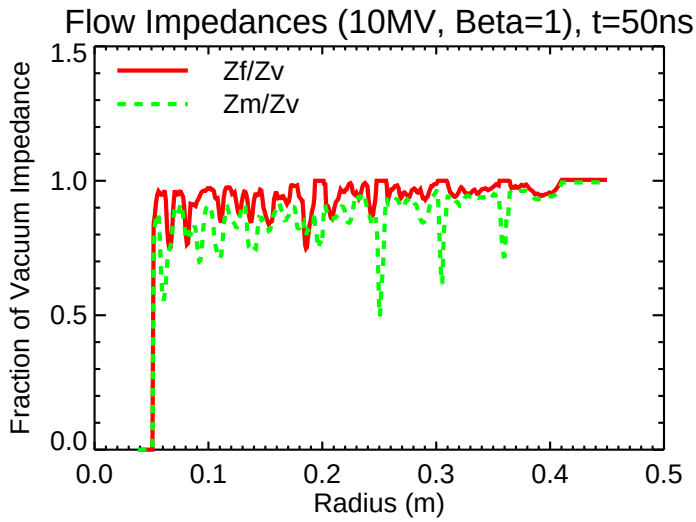

Figure 5.25: Electric and Magnetic flow impedances at $t = 50$ ns, high-voltage.

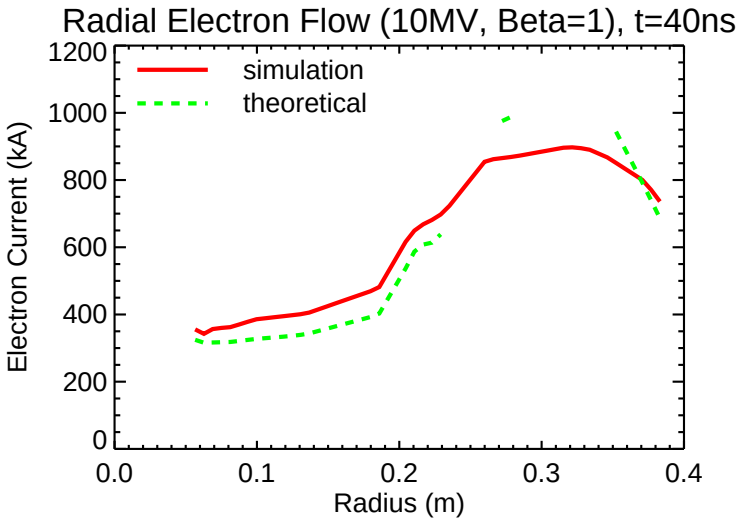

Figure 5.26: Radial electron flow at $t = 40$ ns for the $\beta = 1$ MITL profile with 5 MV forward voltage wave.

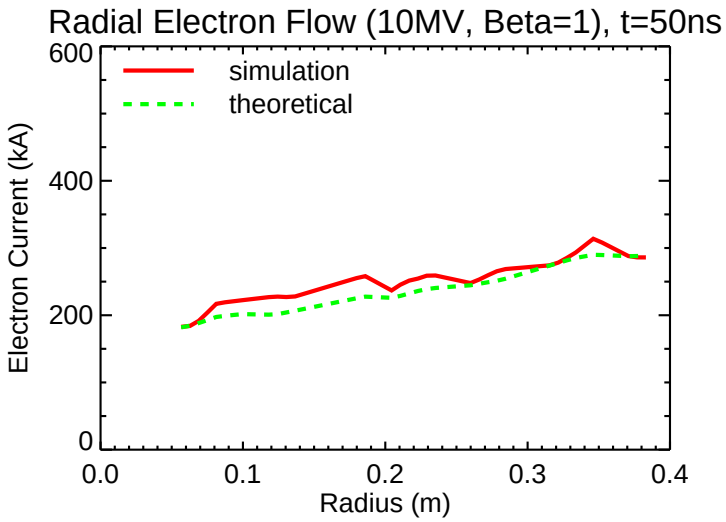

Figure 5.27: Radial electron flow at $t = 50$ ns for the $\beta = 1$ MITL profile with 5 MV forward voltage wave.

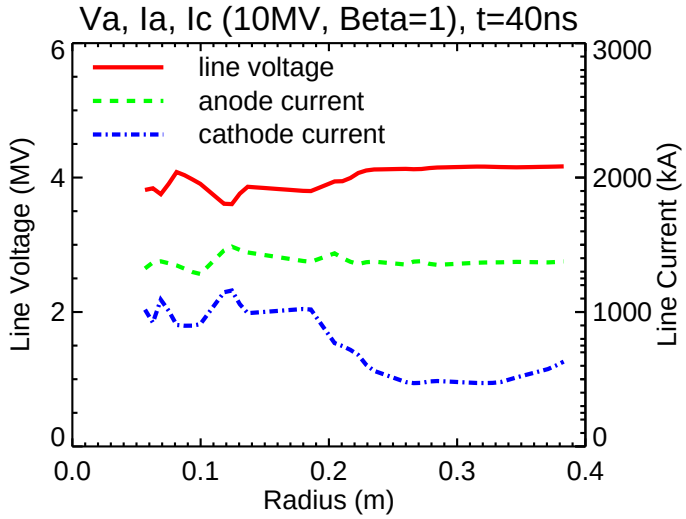

Figure 5.28: Line voltage, anode current, and cathode current plotted versus radius at $t = 40$ ns, high-voltage.

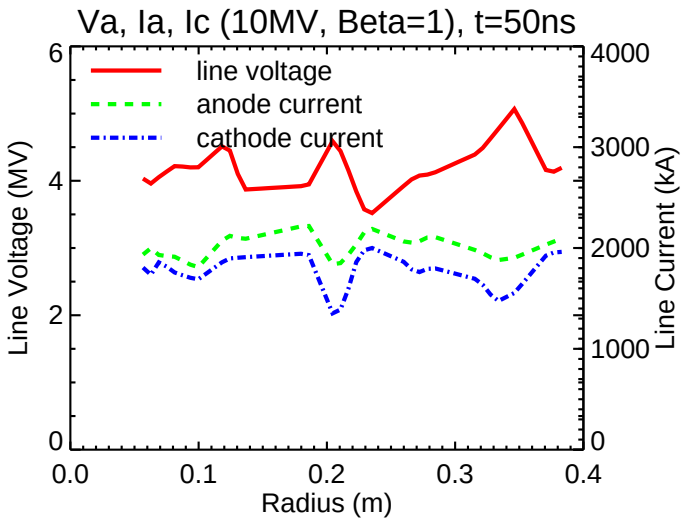

Figure 5.29: Line voltage, anode current, and cathode current plotted versus radius at $t = 50$ ns, high-voltage.

The results of the low voltage simulation for the $\beta = 1$ profile are summarized in figure 5.30 through figure 5.37. The charge density contours, flow impedances, and radial electron flows are juxtaposed to illustrate differences in the simulation during, and just prior to, magnetic insulation. At $t = 50$ ns the anode line current is just below the saturated insulation level resulting in the familiar separation between the charge and current density centorids, figure 5.30. Due to the low voltage and inadequate pressure balance, the theoretical model for the radial flow is unable to converge at large radius, figure 5.34. During insulation, $t = 65$ ns, the electron charge density is held near the cathode, yet the electric and magnetic flow impedances are still characterized by a noticeable separation due to large amounts of space charge, 5.33. The radial electron flow during insulation, figure 5.35, is very close to the values predicted by the theoretical model, however, at large radius they begin to diverge due to the larger gap spacing and weaker electric field strength present from the marginal voltage levels.

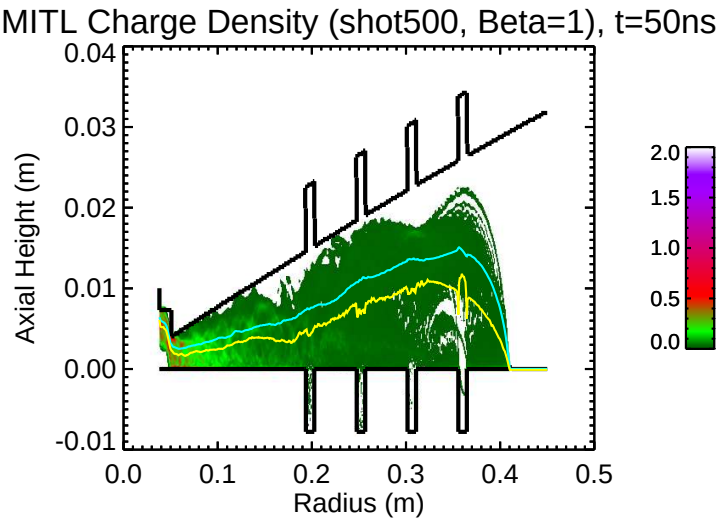

Figure 5.30: Charge Density at $t = 50$ ns for the $\beta = 1$ MITL profile with 500 kV forward voltage wave.

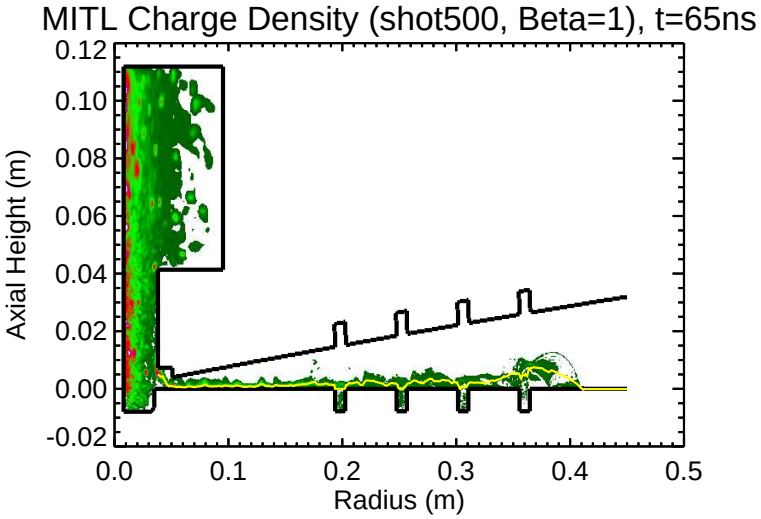

Figure 5.31: Charge Density at $t = 65$ ns for the $\beta = 1$ MITL profile with 500 kV forward voltage wave.

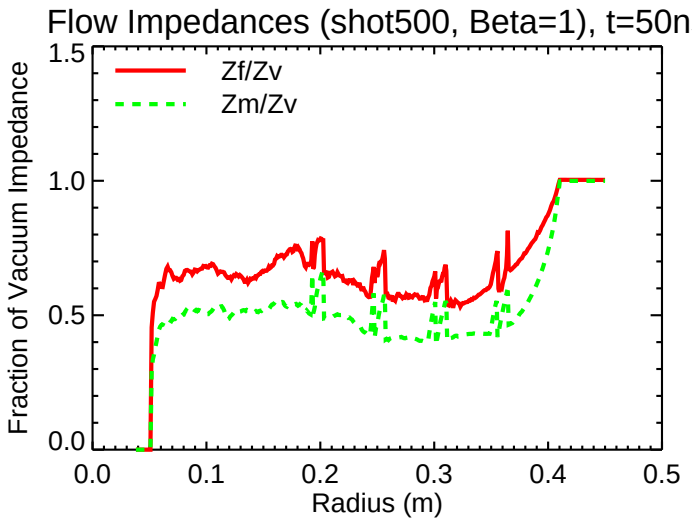

Figure 5.32: Electric and Magnetic flow impedances at $t = 50$ ns, low-voltage.

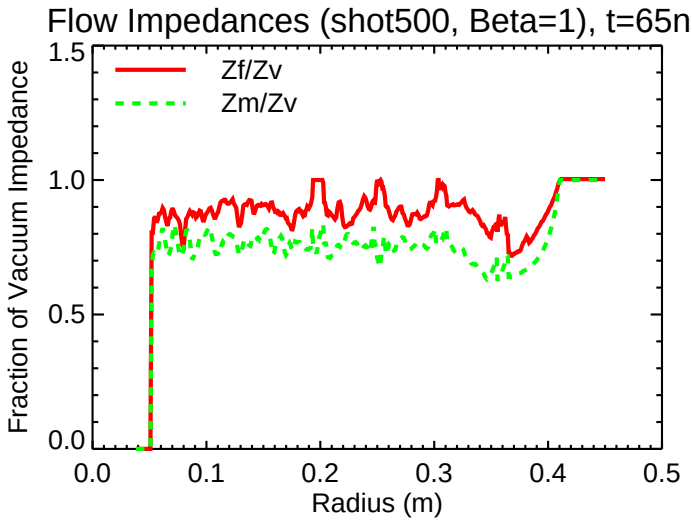

Figure 5.33: Electric and Magnetic flow impedances at $t = 65$ ns, low-voltage.

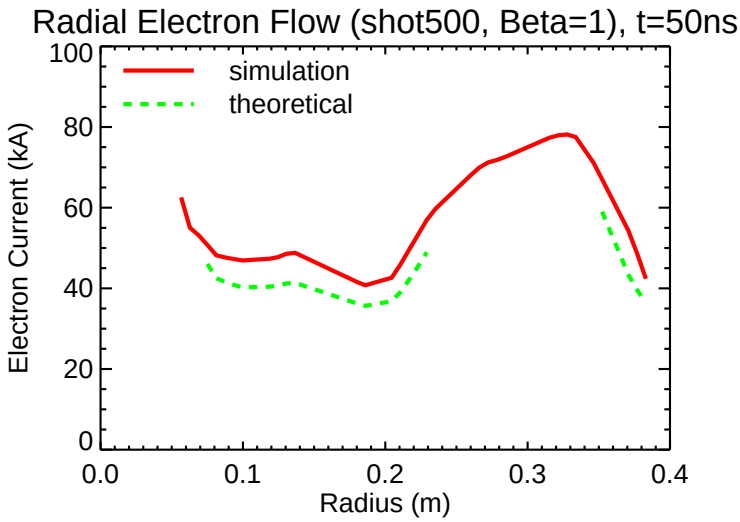

Figure 5.34: Radial electron flow at $t = 50$ ns for the $\beta = 1$ MITL profile with 500 kV forward voltage wave.

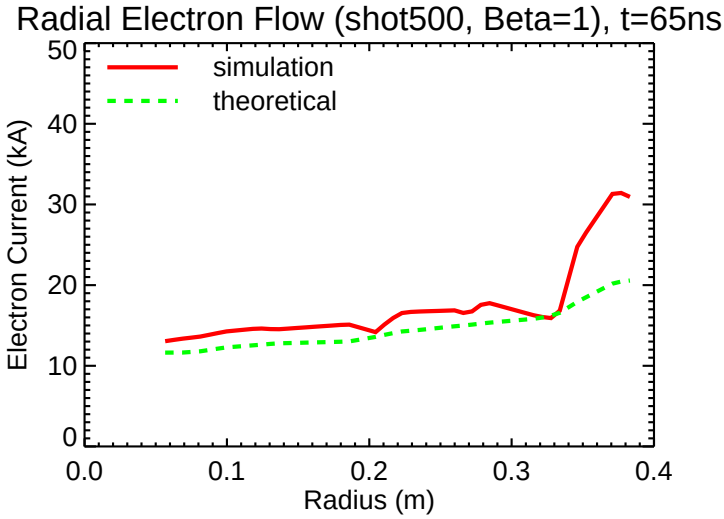

Figure 5.35: Radial electron flow at $t = 65$ ns for the $\beta = 1$ MITL profile with 500 kV forward voltage wave.

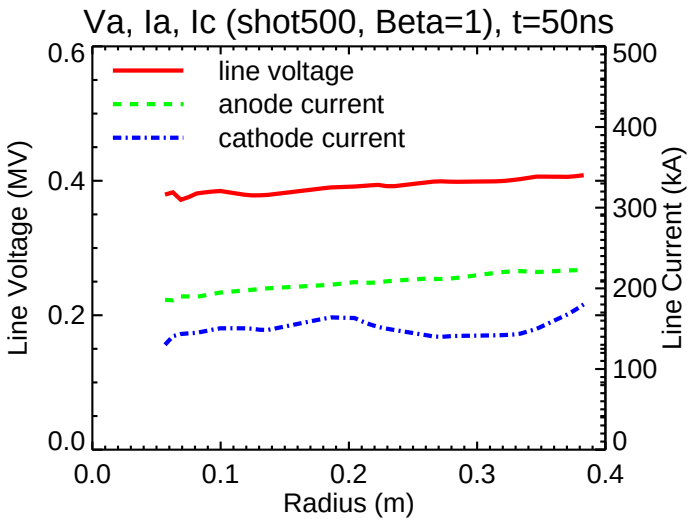

Figure 5.36: Line voltage, anode current, and cathode current plotted versus radius at $t = 50$ ns, low-voltage.

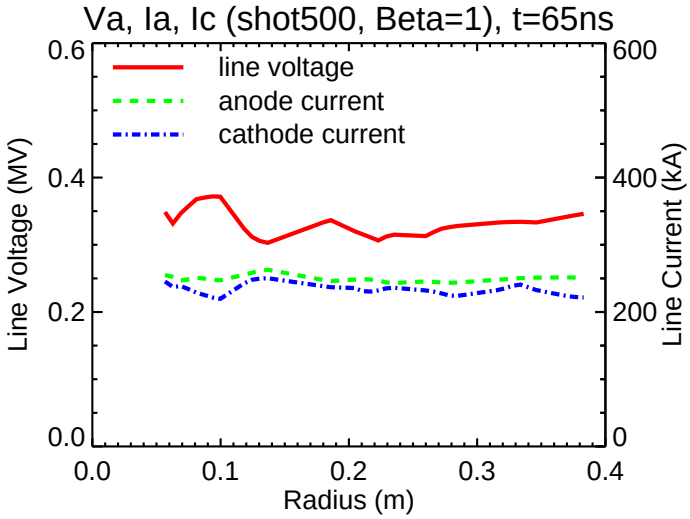

Figure 5.37: Line voltage, anode current, and cathode current plotted versus radius at $t = 65$ ns, low-voltage.

5.1.3 Reducing Electron Flow, $\beta \simeq 3.7$

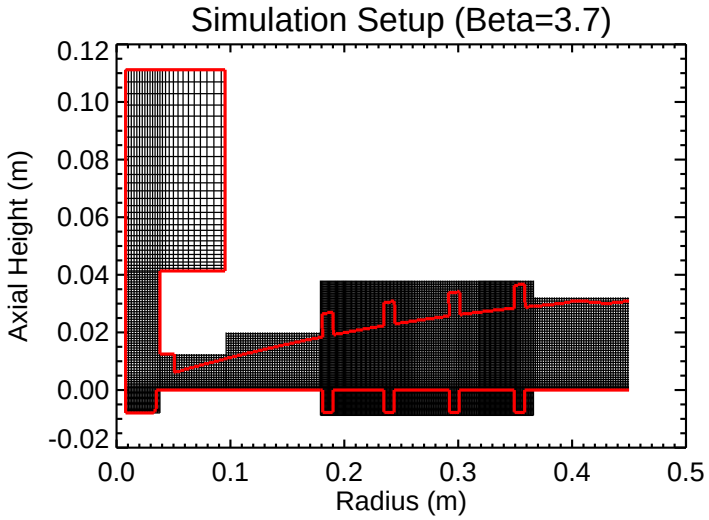

Figure 5.38: Simulation setup for the $\beta = 3.7$ reducing electron flow profile. The transmission line feed inlet is positioned at $r = 0.45$ m. The minimum cell size is 200 μm and covers the entire middle portion of the MITL.

The simulation setup for the reducing flow profile, $\beta > 3$ is given in figure 5.38. This was one of the earliest simulations and is characterized by a more extensive finer mesh. Later it was discovered that smaller cell sizes in the middle of the A-K gap didn't improve the accuracy of the simulation and just resulted in increased computation time. Future simulations were constructed in order to limit the finer meshing to just the cathode surface and the diagnostic grooves in the A-K gap.

The results of the high voltage simulation for the $\beta > 3$ profile are summarized in figure 5.39 through figure 5.46. Although lower electron current at small radius is beneficial in the reduction of potential electron energy being deposited into the anode, larger re-trapping parameters usually result in a more unstable electron flow. These vortices tend to be most prevalent at smaller radius near the minimum gap. Unstable flow within small A-K gaps often provides a mechanism for electron transmission to

the anode as will be shown in section 5.3.

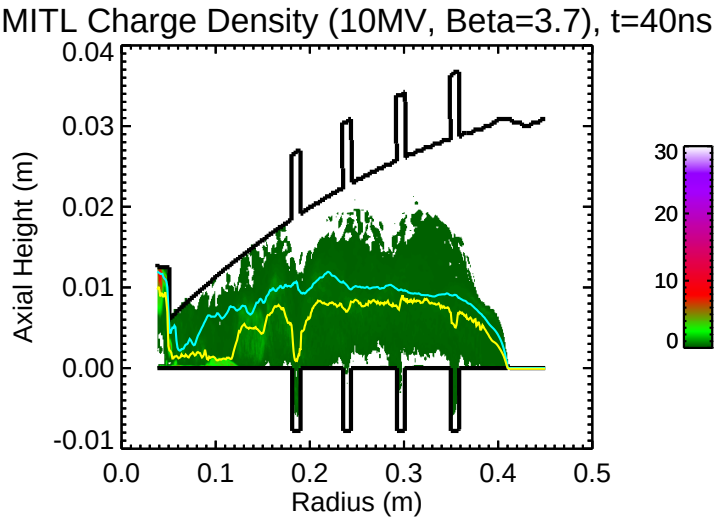

Figure 5.39: Charge Density at $t = 40$ ns for the $\beta = 3.7$ MITL profile with 5 MV forward voltage wave.

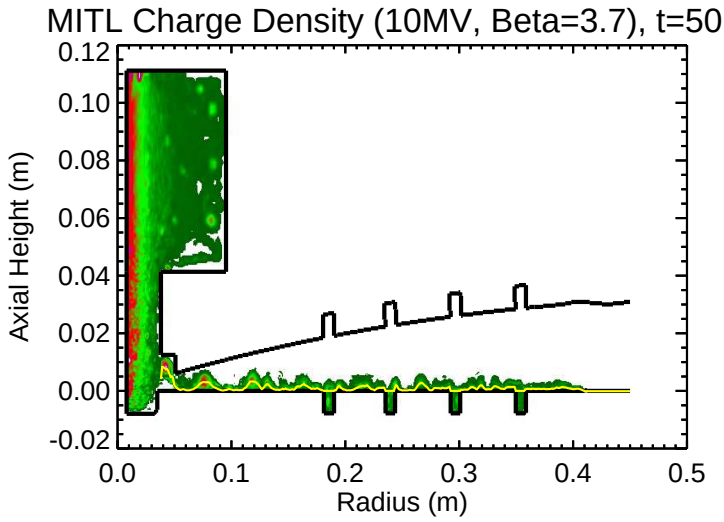

Figure 5.40: Charge Density at $t = 50$ ns for the $\beta = 3.7$ MITL profile with 5 MV forward voltage wave.

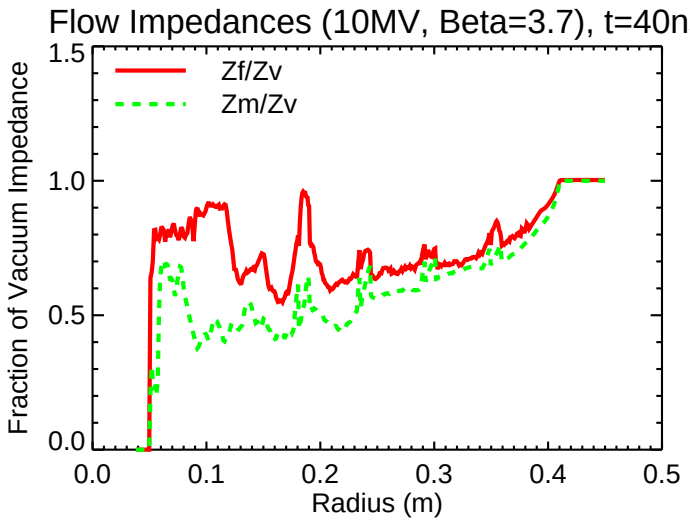

Figure 5.41: Electric and Magnetic flow impedances at $t = 40$ ns, high-voltage.

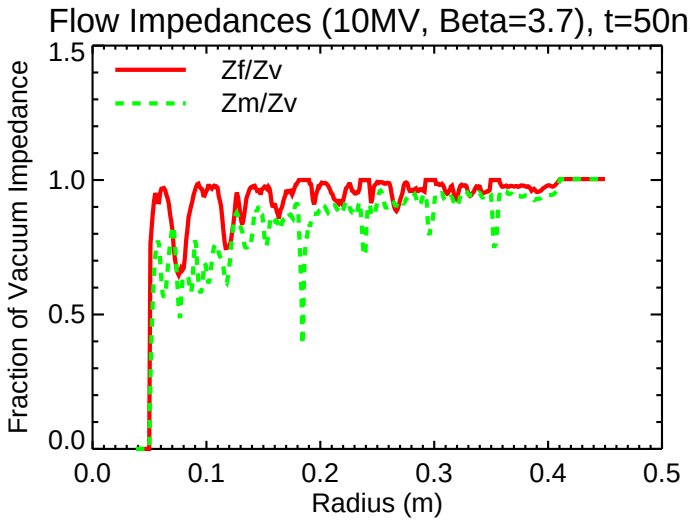

Figure 5.42: Electric and Magnetic flow impedances at $t = 50$ ns, high-voltage.

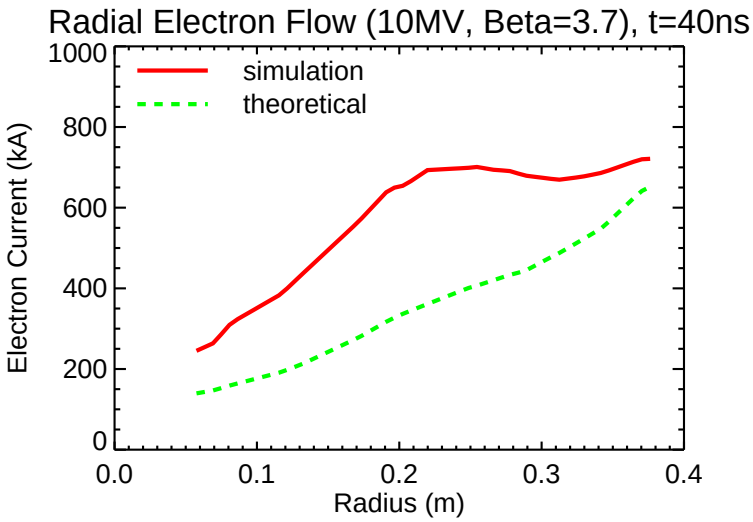

Figure 5.43: Radial electron flow at $t = 40$ ns for the $\beta = 3.7$ MITL profile with 5 MV forward voltage wave.

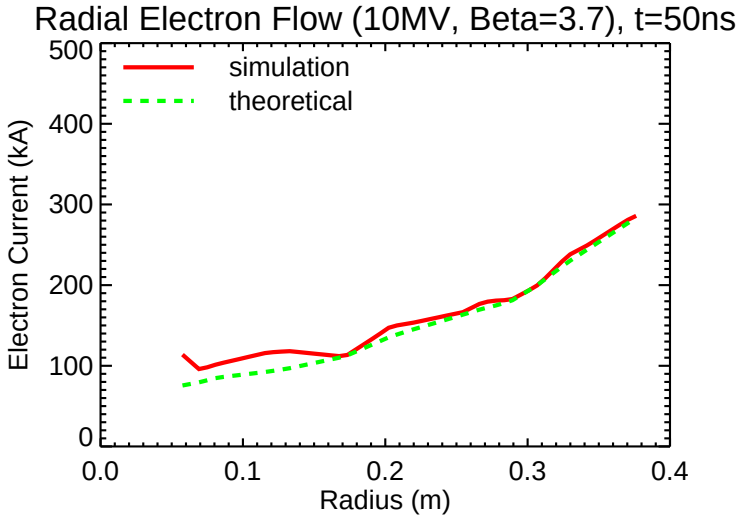

Figure 5.44: Radial electron flow at $t = 50$ ns for the $\beta = 3.7$ MITL profile with 5 MV forward voltage wave.

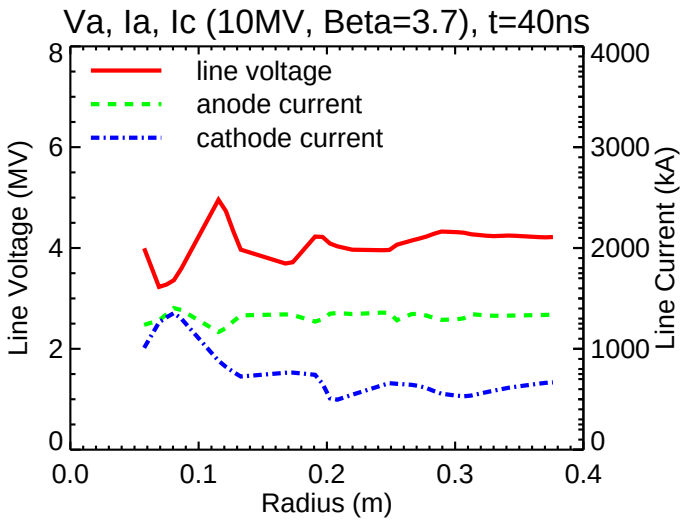

Figure 5.45: Line voltage, anode current, and cathode current plotted versus radius at $t = 40$ ns, high-voltage.

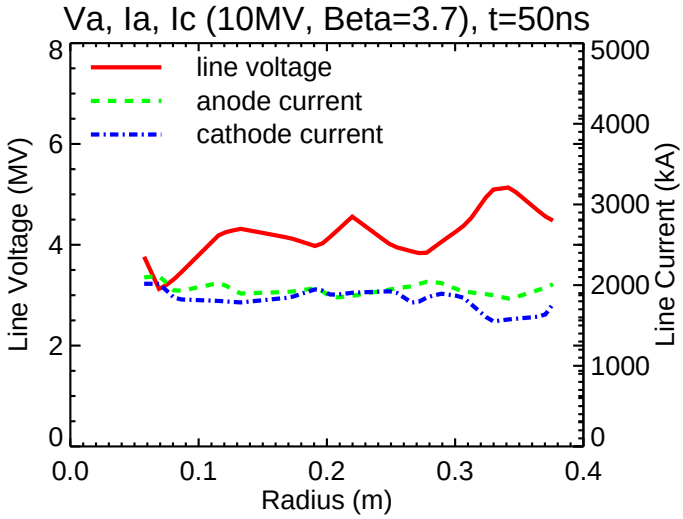

Figure 5.46: Line voltage, anode current, and cathode current plotted versus radius at $t = 50$ ns, high-voltage.

5.2 Re-trapping Parameter Comparison

Comparisons between the re-trapping rate of several radial electron flow profiles are given below. These simulation profiles ranged from nearly constant flow, $\beta \simeq 0$, to a greatly reducing flow, $\beta > 3$. Additional re-trapping rates were obtained by changing the height of the simulated load cavity. The lumped inductance at the load, L_o, is one of the three main design parameters for the re-trapping rate of electron flow. By increasing the height of the load cavity for a particular radial profile, the re-trapping parameter will decrease. Alternatively, if the can height is decreased, this lowered inductance causes β to increase. This was done experimentally by designing two separate load cavities of 33.9 nH and 50 nH. The original anode geometries were designed for $\beta = 0$ and $\beta = 1$ assuming a 50 nH load inductance. The additional load provides twice the number of radial profiles for the anode hardware used; each lower inductive load resulting in a slightly higher reduction in inner radial electron flow. These re-trapping parameters, as well as those resulting from purely simulated load geometries, were included in the plots below.

The theoretical model developed in section 2.5.1 predicts that the electron current for any given re-trapping parameter, β, will be of the form:

$$I_e(r) = I_{e:r_{max}} \exp(\beta(r - r_{max})), \tag{5.2}$$

where $I_{e:r_{max}}$ is the maximum electron current for a reducing flow profile and r_{max} is the maximum radial length of the disk MITL. The three high voltage radial profiles covered in section 5.1 are plotted together in figure 5.47. Each curve has been shifted vertically such that the their values coincide at maximum radius. This plot includes the simulation data for each re-trapping parameter, the theoretical solution utilizing pressure-balance, and the general current model from equation 5.2.

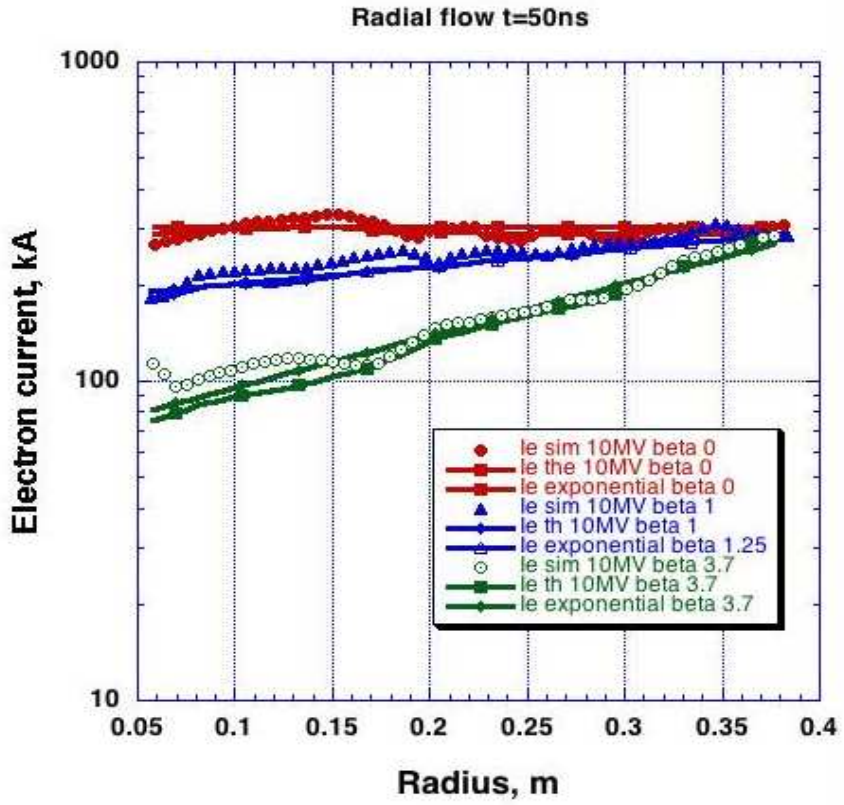

Figure 5.47: Simulation electron flow for the $\beta = 0$, 1, and 3.7 radial profiles at high voltage. $\beta = 0$ represents constant electron flow. $\beta = 1$ represents a reduction of electron flow which decreases as $1/e$ for every meter towards the load. $\beta = 3.7$ represents the highest re-trapping rate.

The simulation values appear to corroborate the theoretical predictions to a great extent. The change in re-trapping rates partitions figure 5.47 into three distinct sections. The 'top' curve represents the constant electron flow design, $\beta = 0$, while the $\beta = 1$ curve is shown to decrease by $1/e$ for every reducing meter. The 'bottom' curve represents an aggressive re-trapping rate that is characterized by a large drop in electron flow near the load. The separation between the group of curves illustrates the relative decrease in electron flow at inner radius for higher re-trapping rates. Additional high-voltage simulations with varying re-trapping rates are shown in

figure 5.48. These re-trapping rates were constructed by altering the load inductance of the MITL profiles given in figure 5.47. This change in the MITL inductance affects the line voltage in each simulation resulting in a time shift for the magnetic insulation. For comparison, each curve had to be recorded within its own respected window of magnetic insulation. It is only for this window of time that the re-trapping parameter is defined. This can be illustrated for the case of constant electron flow in figure 5.49. Radial profiles were constructed periodically over a relatively long simulated time interval. For each profile an IDL[4], curve fitting, routine was incorporated to determine the relative re-trapping rate in each case. These re-trapping parameters were then plotted versus time to determine their range of convergence.

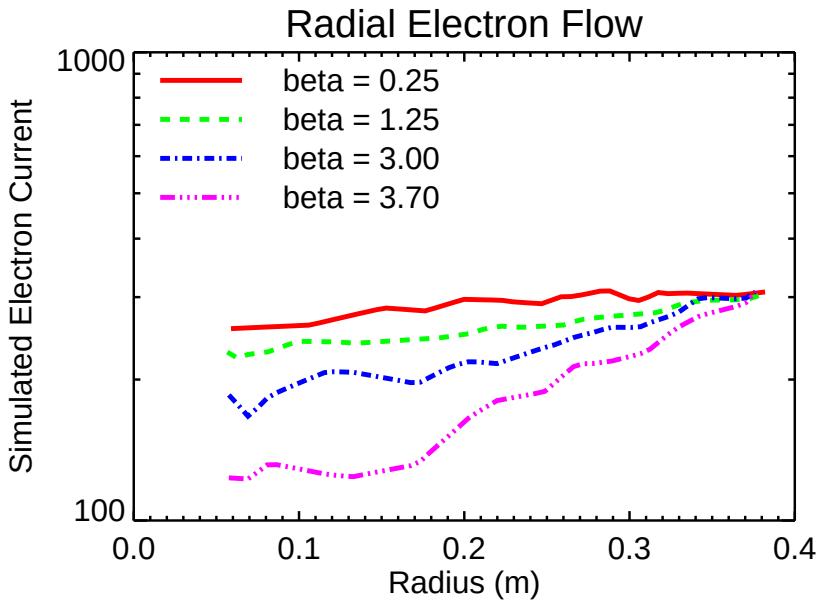

Figure 5.48: Comparison between four different simulated re-trapping rates. Each simulation was characterized by a different MITL inductance resulting in different times for magnetic insulation to occur. Each curve was recorded during its respective insulation window.

4

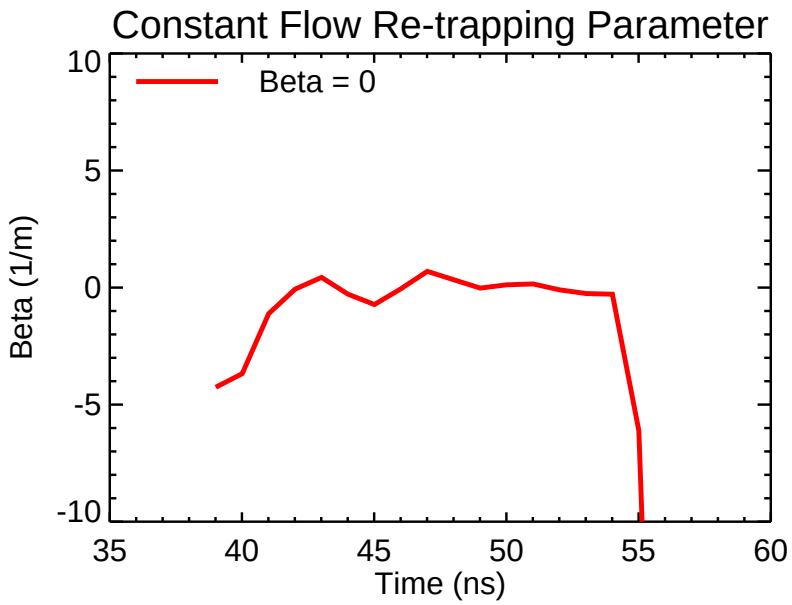

Figure 5.49: Re-trapping parameter, β, versus time for a high-voltage constant electron flow profile. The plateau region of the curve represents the time period of magnetic insulation.

For each simulation the following always appears to hold: For a particular load inductance, an increase in the re-trapping rate leads to a decrease of electron current at the load, figure 5.50. If the load inductance is held constant and the change in re-trapping rate is only due to a modification in the anode curvature, this reduction appears to follow a nearly linear regression. If the local voltage level significantly changes from one re-trapping rate to the next, due to inductive load alterations, then the electron flow at the load can rise. When the inductance is increased, the ratio of the electron current at the load to the current at the feed continues to decline as in the constant load case, however, the voltage along the entire line is raised.

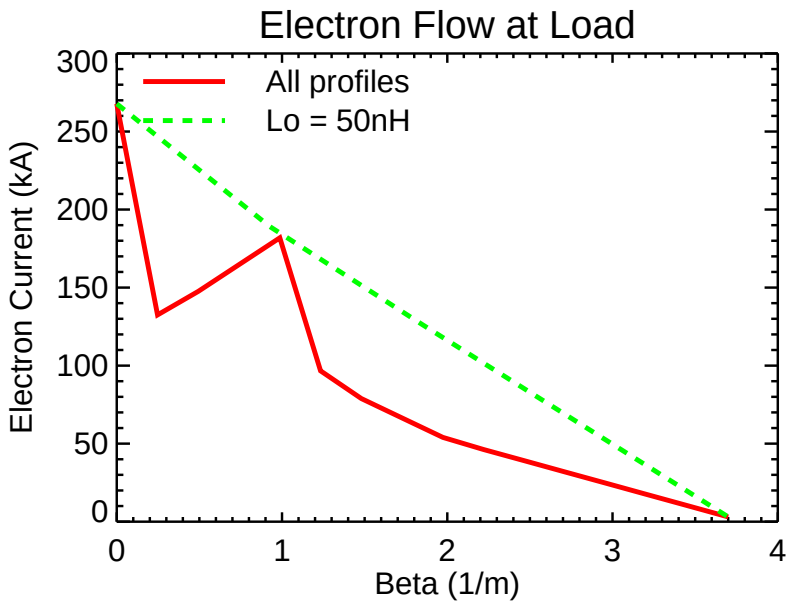

Figure 5.50: Simulated electron flow at the entrance to the load cavity. The top curve represents a reduction in flow with a increase in the re-trapping parameter for a constant load inductance. The bottom curve is a collection of all the simulated re-trapping rates based on various load inductances. The curve droops away from the top line because the additional re-trapping rates were obtained with a lower load inductance.

Similar comparisons can be made for the above simulated profiles operating at low-voltage. Figure 5.51 combines the low-voltage simulation data with theoretical predictions for the same re-trapping rates plotted in figure 5.47. The theoretical model appears to be more accurate for more stable re-trapping rates (i.e. $\beta \leq 1$). While these curves cannot be characterized by a monotonically radially increasing function, their decreasing electron flow at inner radius for increasing β is still consistent with the higher voltage simulations. The variations displayed here are not surprising because the low voltage does not specifically meet the assumptions of the original model.

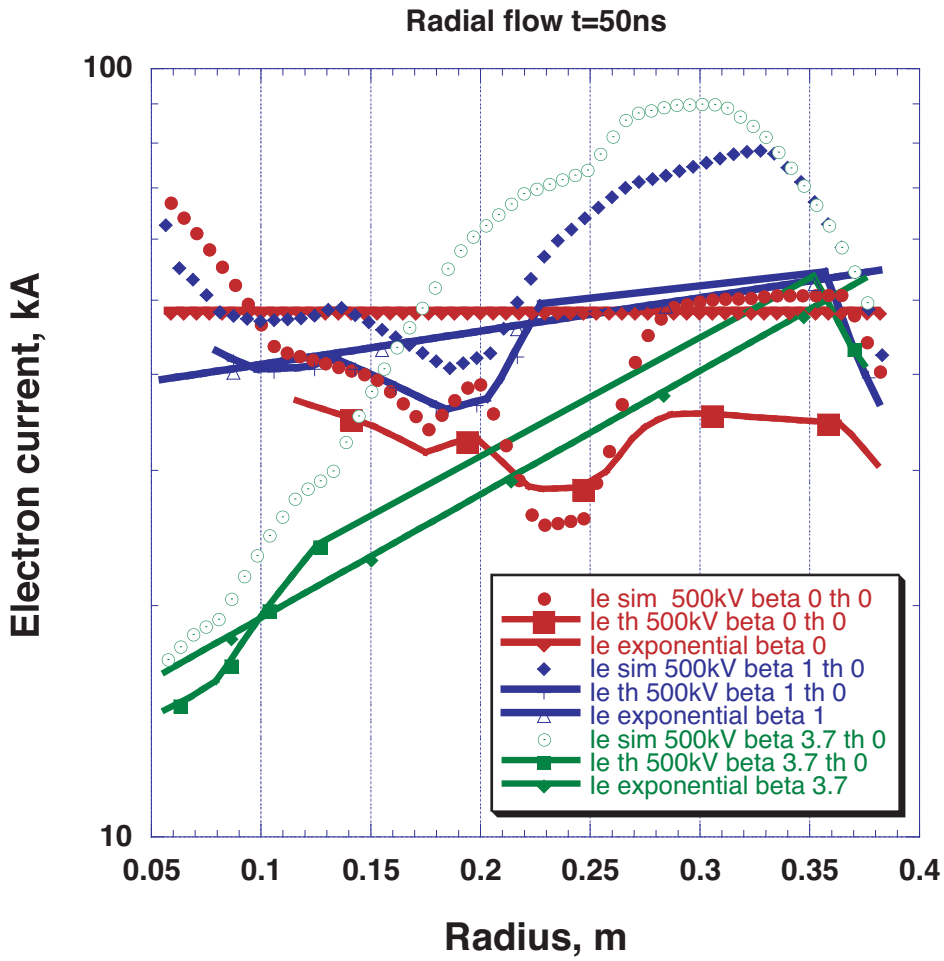

Figure 5.51: Simulation electron flow for the $\beta = 0$, 1, and 3.7 radial profiles at low voltage. These curves display a larger fluxuation from the theoretical model than the high-voltage case. This is not surprising, however, since low voltage does not specifically meet the assumptions of the model.

5.3 Anode Temperature

The heating of the anode surface by electron energy deposition for each of the simulations above was calculated using the QUICKSILVER/ITS coupling model[5]. The incident angle, momentum, and total charge of each simulation particle passing through the anode surface was recorded. The temperature along the conductor surfaces was initialized to 20 °C and the temperature differential was calculated using equation 4.5. The local energy deposition and specific heat capacity were found using a "lookup" data table that was formulated for stainless steel 304a[6]. This is consistent with the inner radial material of the MITL which consists of a steel anode and cathode insert. For outer Aluminum sections, the temperature increase, ΔT, is approximately 18.7% higher as a result of the difference between the density and specific heat capacities of the materials. While the density of steel is almost three times that of Aluminum, the specific heat capacity is almost half, where the average specific heat capacity of Aluminum over a temperature interval of 25-500 °C is roughly 990 (J $kg^{-1}K^{-1}$) [56].

The electron energy deposition into the conductors of each of the radial disk profiles all shared similar characteristics. For high voltage simulations (i.e. 5 MV forward wave), the maximum heating was found to occur within the load region of the transmission line while the only significant anode temperature change within the A-K gap occurred at the entrance to the load cavity. For lower voltage simulations (i.e. 500 kV forward wave), the largest accumulation of electron energy deposition was located at the entrance to the load cavity and was on the same order of magnitude as the high voltage simulations. The maximum recorded surface temperature for each profile and each boundary condition feed is provided in table 5.1. The location of the maximum surface is given as well as the total measured inductance at the

[5]This was covered in section 4.1.2

[6]SS304a is the material of the radial MITLs used in the Z machine at Sandia Labs.

transmission line feed. It is important to note that although the minimum gap is almost doubled from $\beta = 0$ to $\beta \simeq 3.7$, the inductance of the line and thus the efficiency of the MITL has not been significantly compromised. Plots of the maximum temperature and line inductance versus β for the low voltage and high voltage case are given in figures 5.52 and 5.53 respectively.

Simulation	T_{max}(°**C**)	**Location** (r, z)	L(**nH**)
$\beta = 0$, shot500	1034.16	(0.502, 0.0033)	55.71
$\beta = 0$, 10MV	9423.56	(0.0381, 0.0096)	55.71
$\beta = 1$, shot500	541.796	(0.502, 0.0033)	56.2
$\beta = 1$, 10MV	7599.81	(0.0381, 0.0096)	56.2
$\beta = 3.7$, shot500	222.669	(0.502, 0.0033)	58.32
$\beta = 3.7$, 10MV	3167.51	(0.0381, 0.0096)	58.32

Table 5.1: Maximum anode temperature for each simulation setup.

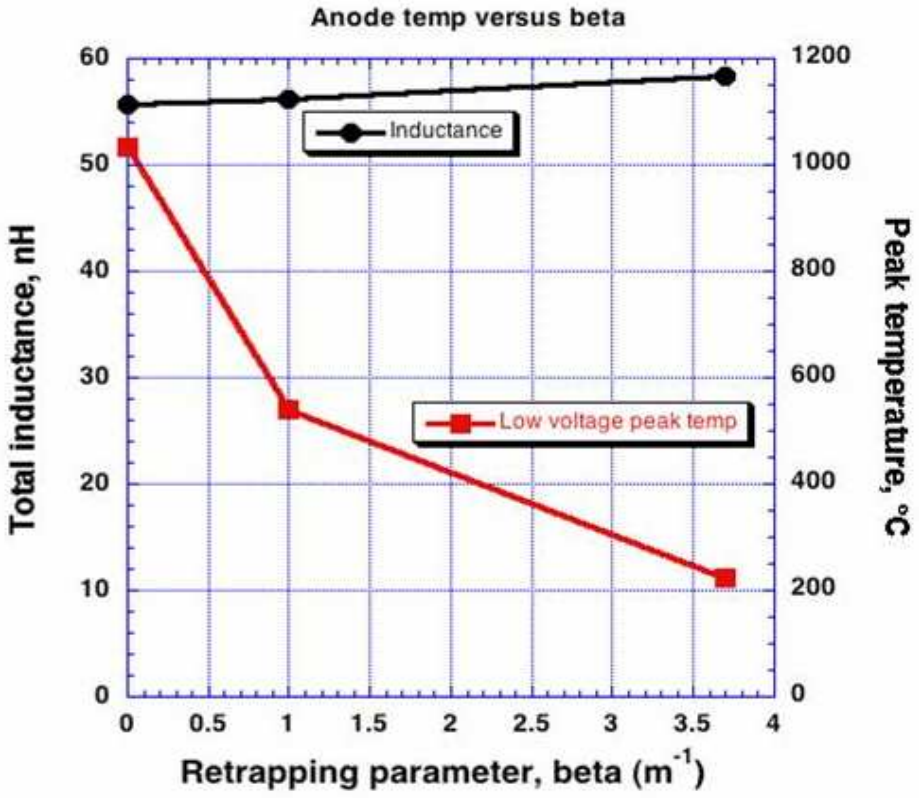

Figure 5.52: Peak anode surface temperature and line inductance versus β for the low voltage (500 kV) QUICKSILVER simulations. Electron emission thresholds for the low voltage case are assumed to be zero. Temperature measurements are made at the end of the pulse, $t = 89$ ns.

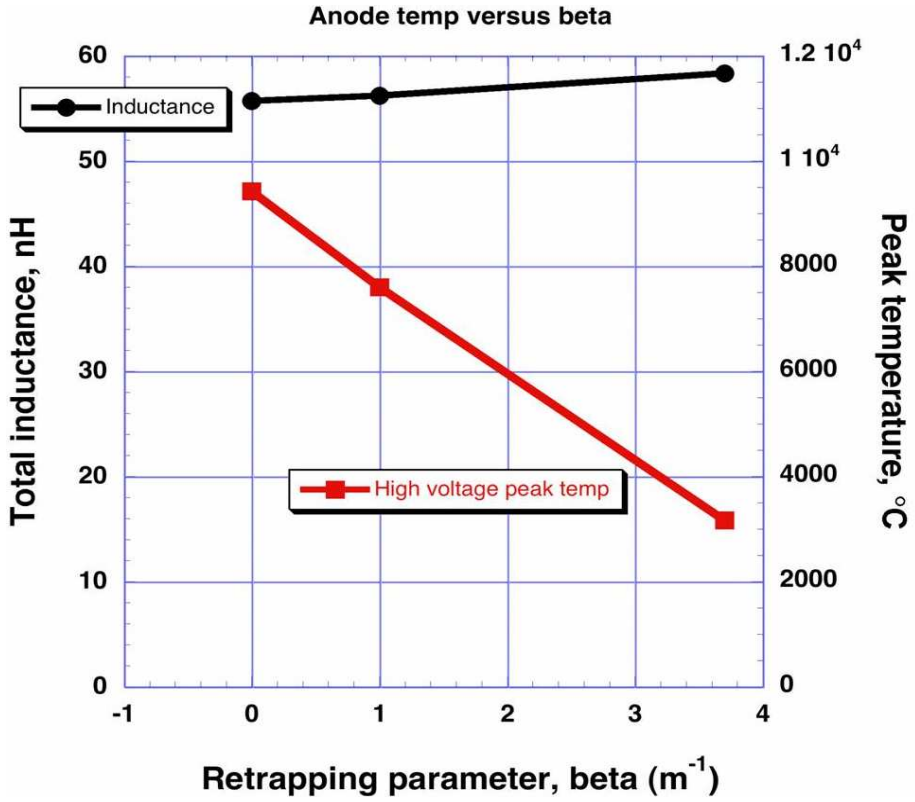

Figure 5.53: Peak anode surface temperature and line inductance versue β for the high voltage (5 MV) QUICKSILVER simulations. Electron emission thresholds for the high voltage case are assumed to be 200 kV/cm. Temperature measurements are made at the end of the pulse, $t = 89$ ns.

The anode temperature snapshots for the high voltage constant flow profile are given in figures 5.54 and 5.55. Figure 5.54 shows all of the temperature surface contours within the MITL above an the ambient temperature, $T = 20°\text{C}$. For large voltages, the greatest rise in anode temperature was recorded inside the load region at the top of the throat, just inside the upper cavity. An enlarged snapshot of the heated anode region at the minimum gap is given in figure 5.55. The temperature threshold along the anode surface was set for 400 °C to coincide with the approximate threshold for anode plasma formation [55].

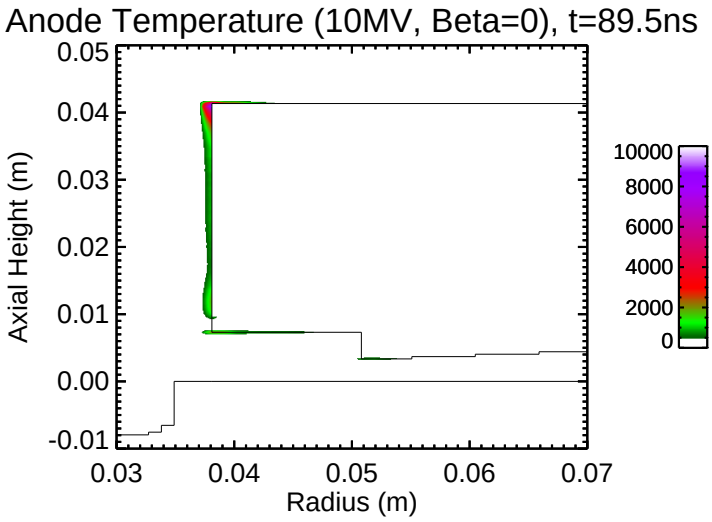

Figure 5.54: Electrode heating due to electron deposition for the high voltage simulation. The maximum surface temperature is located in the upper throat of the load cavity. The only significant anode heating occurs at the minimum gap spacing.

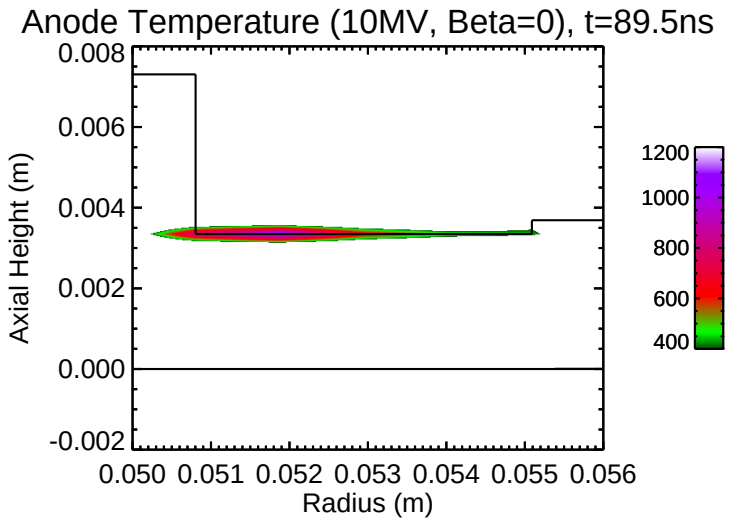

Figure 5.55: Enlarged contour temperature plot of the anode minimum gap region. Temperatures in excess of 400 °C are shown along the anode surface.

The anode temperature snapshots for the constant flow profile fed with the 500 kV forward traveling wave are given in figures 5.56 and 5.57. For lower voltage levels the largest anode temperature coincides with the minimum gap spacing at the entrance to the load. The enlarged contour temperature plot at the minimum gap is given in figure 5.57. Once again the minimum threshold has been set to 400 °C to show the location of possible anode plasma formation.

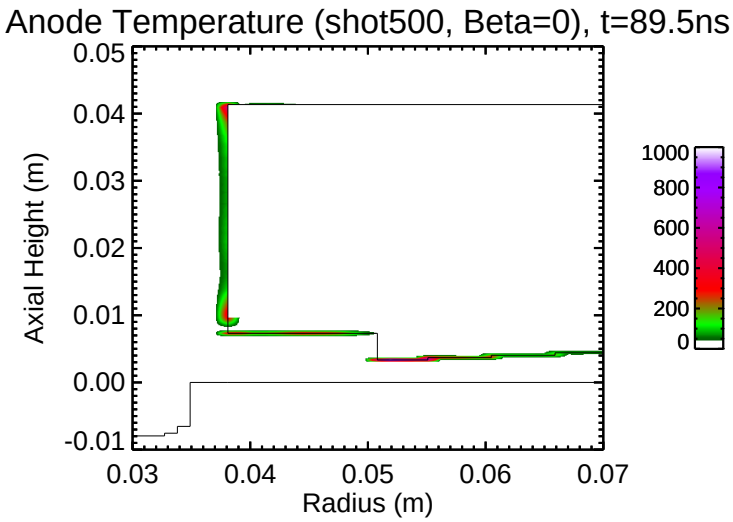

Figure 5.56: Electrode heating due to electron deposition for the low voltage simulation. The maximum surface temperature occurs at the minimum gap spacing.

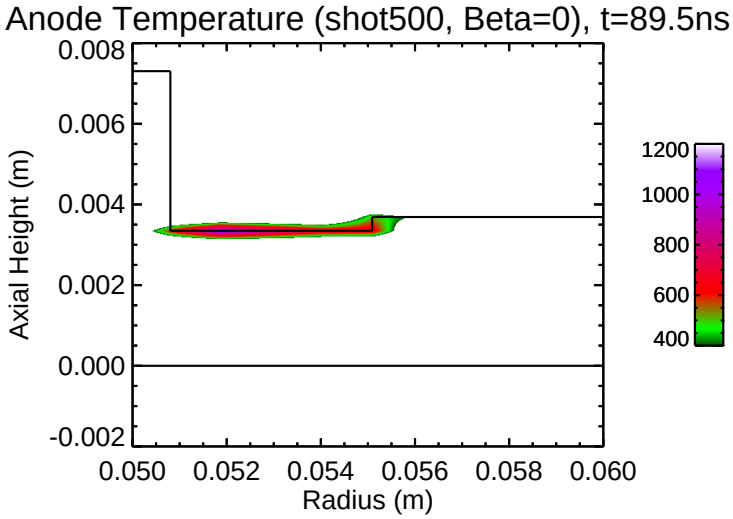

Figure 5.57: Enlarged contour temperature plot of the anode minimum gap region. Temperatures in excess of 400 °C are shown along the anode surface.

From the onset of the power pulse the inductive load appears as a shunt between the anode and cathode of negligible resistance. For $t = L/Z_{cav}$, where Z_{cav} is the transmission line vacuum impedance at the entrance to the load cavity, electrons stream to the anode at the minimum gap. For the constant electron flow profile, $\beta = 0$, the load impedance is shown in figure 5.58. For this case, the minimum gap, g_o, was 0.0036 m and the load inductance, L_o, was around 50 nH resulting in a time constant of $t \simeq 12.4$ ns. For $t > 12.4$ ns, the electrons begin traveling into the load cavity and establish a current along the inner collector can. If the minimum gap was doubled, in this case, the time for electron energy deposition would be cut in half. Consequently, the minimum gap becomes an important design parameter. In the situation where the maximum gap of the disk line is a constraint, the anode profile only has two degrees of freedom. When heating of the anode is considered, there will be a further constraint on the gap size at the load that will limit the possible fractional radial electron flow that can be implemented.

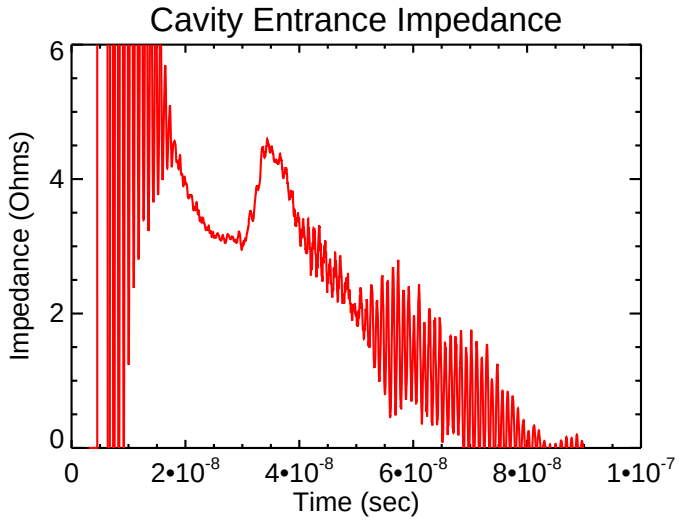

Figure 5.58: Load impedance for the constant radial electron flow profile.

Table 5.2 provides a summary of the time required for the anode surface at the minimum gap to be heated to 400 °C. Due to poor insulation, the lower voltage simulations reach the threshold anode temperature much faster even though the higher voltage simulations initiate electron emission from the cathode earlier. For minimum gap sizes around 6 mm, the effect of the gap size was dominant over the under-insulated space charge and the low voltage simulation never achieved a surface temperature higher that 222 °C. Additionally the large voltage simulation at this gap spacing suffered from a more unstable electron flow due to having such a large re-trapping rate. This lead to a decrease in the time necessary for the anode temperature to reach 400 °C.

Simulation	**Time for** $T_{anode}(g_o) > 400°\mathbf{C}$
$\beta = 0$, shot500	18.01 ns
$\beta = 1$, shot500	18.51 ns
$\beta = 0$, 10MV	45.51 ns
$\beta = 1$, 10MV	49.01 ns
$\beta = 3.7$, 10MV	36.01 ns

Table 5.2: Time required for minimum gap anode surface to reach 400 °C. Maximum temperature for $\beta = 3.7$, shot500, is 222.7°C.

5.4 Cathode Diagnostic Grooves

The simulation region of the electron sheath near a cathode groove is shown in figures 5.59 and 5.60. These grooves house the large-signal current monitors used in the experiment. After the electron sheath is formed along the cathode, electrons are free to enter the cathode grooves and tend to circulate forming "eddie" currents. If the direction of the electron flow is assumed to only be in the direction of the power flow, then the electrons will fill the groove on the same time scale as the magnetic field. This time can be estimated by the ratio of the inductance of the groove to the resistance seen by the electron current across the groove. The resistance across the groove is given by

$$R = \frac{V_{groove}}{I_e}, \tag{5.3}$$

where the potential across the groove is directly proportional to the time derivative of the MITL's cathode current, $\dot{I}_c$. This scaling factor is the groove inductance, L_g, which determines the time scale for the electrons to fill the groove,

$$\tau = \frac{L_g}{R} = \frac{I_e}{\dot{I}_c}. \tag{5.4}$$

For a typical low voltage simulation, $\tau \simeq 2.7$ ns. Since the grooves are filled with electrons so quickly, there is no significant effect on the measured current registered by the current monitors and the grooves become negligible.

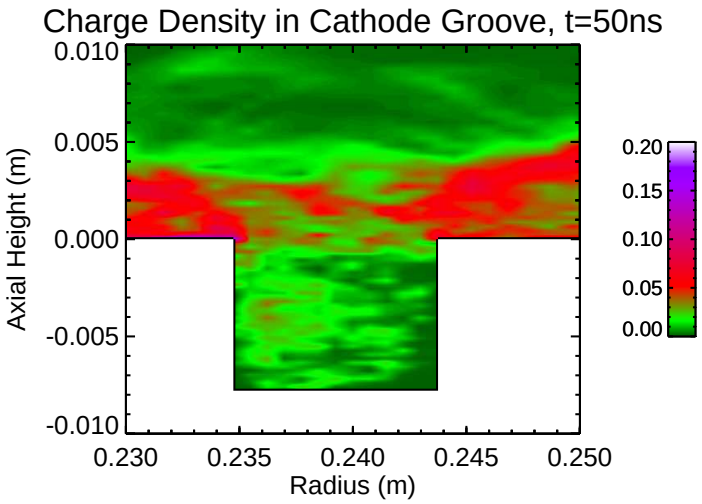

Figure 5.59: Charge density in C/m^3 within a cathode diagnostic groove at 50 ns for a 500 kV simulation.

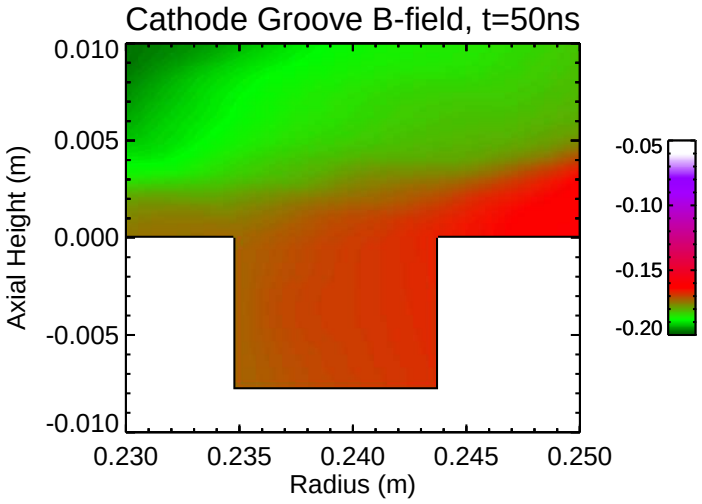

Figure 5.60: Magnetic flux density in Tesla within a cathode diagnostic groove at 50 ns for a 500 kV simulation. The flux is negative denoting that the field is oriented out of the page in the $-\hat{\theta}$ direction.

5.5 Collector Can

In the experimental setup the inductive load cavity houses the inner collector can and CVR diagnostics. Early in the pulse, emitted electrons stream from the cathode to the anode at the load on a time scale of roughly $\tau = L/Z_{cav}$. For $t > \tau$ the electrons enter the outer housing of the load cavity and begin to contribute to the surface current density along the inner collector can. The current is measured by a CVR at the base of the can which records the electron flow at the MITL load. Any electrons that are not captured by the inner collector do not contribute to the electron flow measurement. It is important to determine the distribution of charge density inside the load and to quantify the portion of the charge on each face of the cavity. The length of the inner collector should then be long enough to trap the majority of this charge. If a percentage of the load charge density can be associated with a particular can length then a gauge factor can be determined that would be useful in scaling experimental CVR measurements.

A QUICKSILVER contour plot of the charge density within the load region from the low voltage simulation at peak voltage is shown in figure 5.61. The centroid of the charge density is shown overlaying the contour plot. This centroid extends into approximately 23.4% of the throat region and 13.8% of the upper cavity. Because the dimensions of the load cavity are small in comparison with the ratio of the pulse width to the average electron drift velocity, the effect of the electron space charge in the load region can be approximated through an electrostatic simulation[7]. The simulation results, based upon the centroid charge position, are given in figure 5.62. The original electron collector design would account for slightly more than 97% of the distributed charge within the load cavity. If the inner can is simplified to encompass only the center rod and the lid, only 69% of the charge is accounted for.

[7]The IES ELECTRO software package was used for the electrostatic simulations.

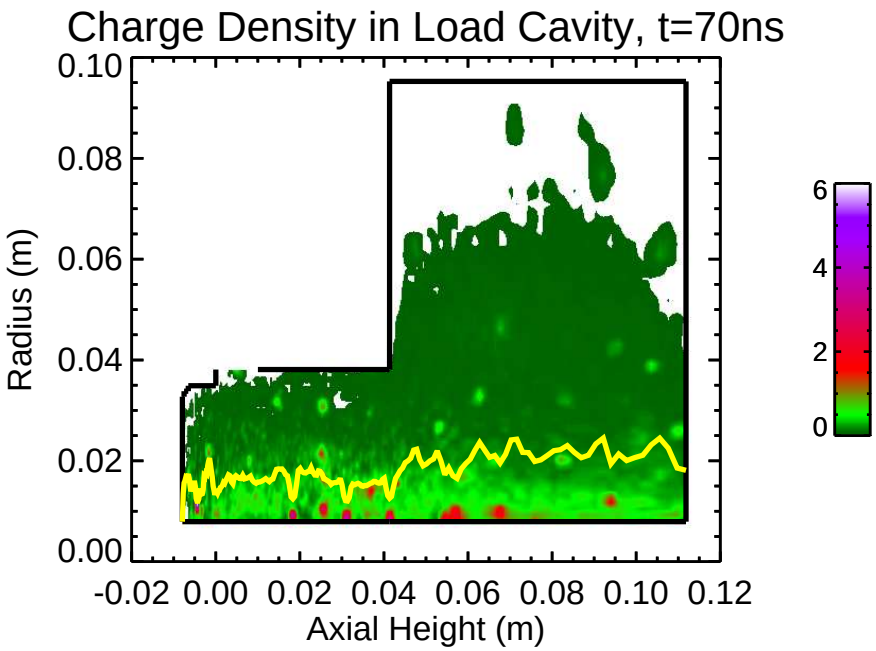

Figure 5.61: Charge density inside the load cavity. The centroid is shown to increase as it crosses from the throat of the can into the upper cavity. The load region is oriented such that center rod running along the axis of revolution is along the x-axis. The entrance to the load is located in the upper left.

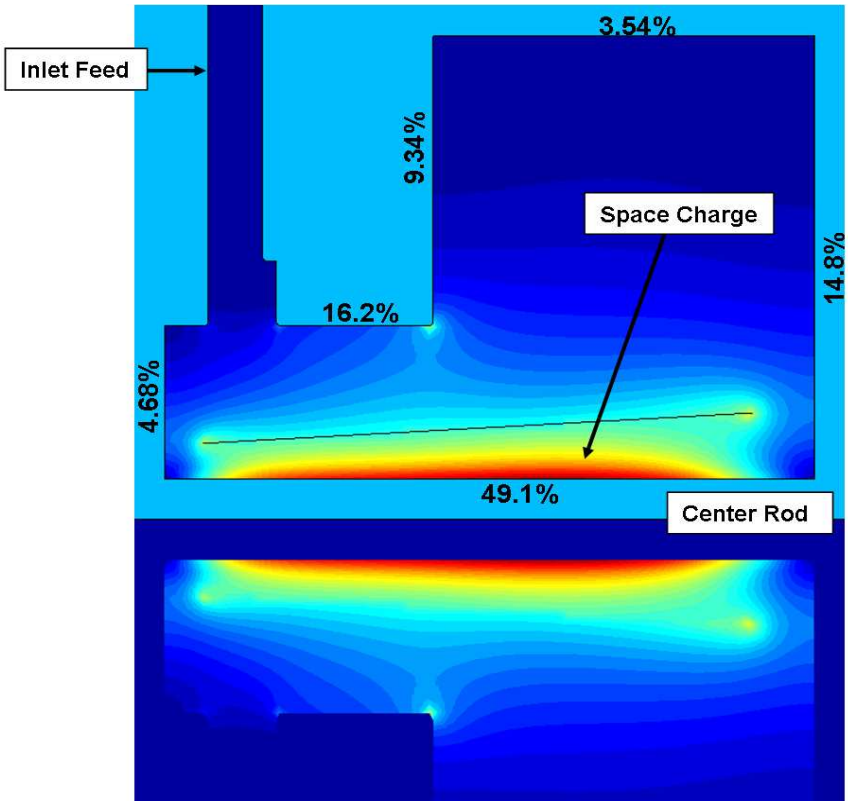

Figure 5.62: Electrostatic simulation of charge distribution within the load. The charge was integrated along the boundaries of the outer can and are displayed as percentages of the total distribution.

Chapter 6

Experimental Results

The experimental data for this dissertation was collected over several shots where the forward voltage waveform, which was used to drive the MITL, was varied over a range of 500 kV to 800 kV. The input power was divided among four pulse forming water lines which connected to the cathode inside the oil side of the insulator stack. The timing between these four lines determined the uniformity of the surface current along the cathode. Individual measurements from the current monitors inside the MITL demonstrated a reasonable uniformity between 120^o sections of the plate. This allowed the current monitors along the anode and cathode to be averaged azimuthally for comparison with the 2-D PIC simulations. Because low voltage simulations, $V < 1$ MV, demonstrated marginal magnetic insulation, it was difficult to distinguish between the general behavior of the electron flow for each set re-trapping rate, especially at smaller radii. As a result, only the constant flow profile, $\beta = 0$, and the largest reduction in flow were examined in the hopes that such a large disparity between re-trapping rates would be evident. The original design for the constant flow profile dictated the use of a 50 nH inductive load in the experiment. In order to maintain comparable voltages between the profiles, the 50 nH load was used along with the other anode hardware, as well, which defined a re-trapping rate

of $\beta \simeq 3.7$. The experimental shots used for the comparison were chosen based on the similarity of the forward voltage wave used to feed each experiment as shown in figure 6.1.

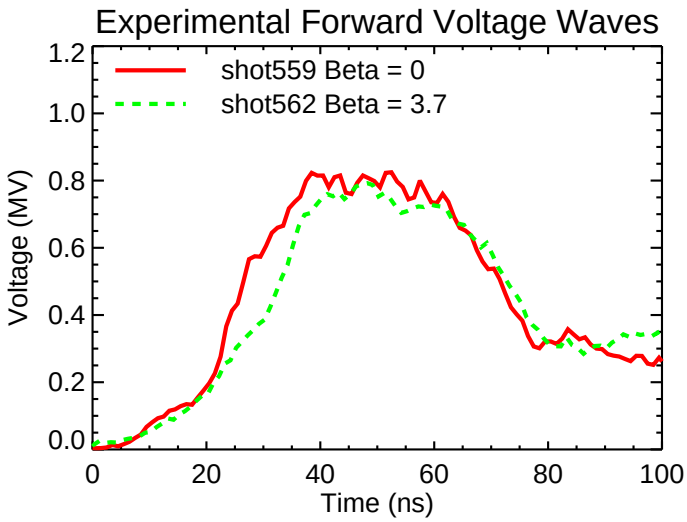

Figure 6.1: Experimental forward voltage waveforms averaged from voltage measurements on the four pulse-forming water lines feeding the MITL. The PIC simulations were driven with these exact waveforms.

6.1 Constant electron flow (shot 559)

The constant electron flow profile was designed to eliminate any radial dependence on the fluctuation of the electron current. This is equivalent to the optimal case of uniform flow when designing the gap spacing under the assumption that field emitted electrons are incapable of returning to the cathode. The simulations for this profile, which were presented in chapter 5, were in excellent agreement with

the theoretical model at high voltage, $V \simeq 5$ MV. The simulation results began to deviate, however, as the fields associated with the pulse began to approach the critical strengths necessary for magnetic insulation. This allowed the electron sheath to extend further into the MITL gap providing a greater opportunity for electrons to reach the anode. Experimental shot 559 was driven with a slightly larger voltage pulse, $V = 800$ kV, than the initial simulations but is still considered within the low voltage regime. Additional simulations were conducted with the new forward voltage wave in order to provide a direct comparison.

A typical anode and cathode measurement from shot 559 is given in figure 6.2. The two curves separate shortly after the field emission threshold has been reached and electrons begin accelerating into the A-K gap from the cathode surface. When electrons leave the cathode, this results in a decrease in the cathode current. The elapsed time between the separation of the line currents and when they come back together, shortly after peak, defines the time window for magnetic insulation. The maximum electron flow occurs near the midpoint and corresponds to $t \simeq 45$ ns.

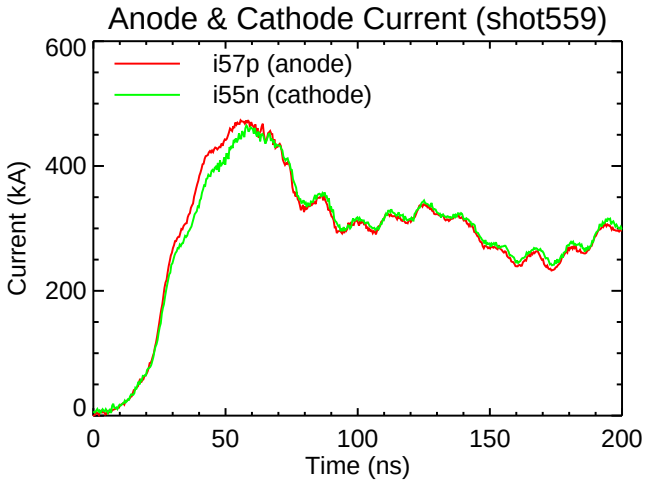

Figure 6.2: Shot 559: Anode and Cathode currents.

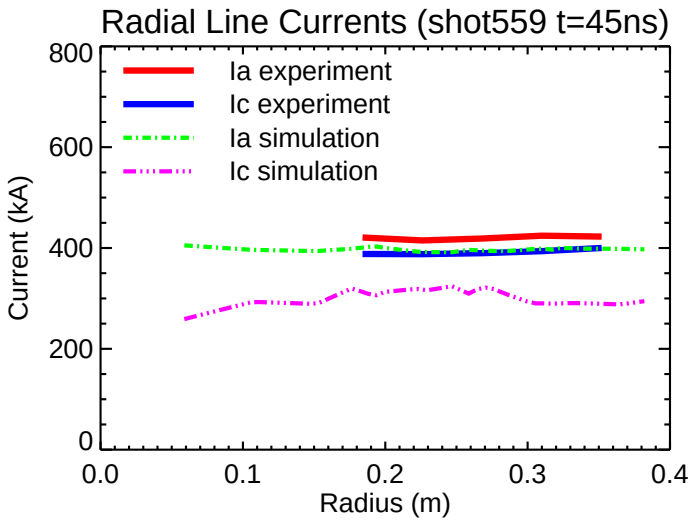

Figure 6.3: Shot 559: Radial profile of anode and cathode currents near the time of peak electron flow.

The radial profile of the anode and cathode currents is illustrated in figure 6.3. Comparisons between the simulation and the time dependent anode and cathode currents are given in figures 6.4 and 6.5 respectively. In this case, the measured anode current compared rather well with the simulation data. The rise-times were in excellent agreement, which demonstrated a close correlation between the inductance calculated within the PIC simulation and that present within the experiment. The cathode currents displayed a similar correlation in rise-time, however, they deviated significantly while electrons were present within the MITL's A-K gap. The cathode current measured on shot 559 exceeded the simulated value by more than 100 kA at peak insulation. This difference led to a dramatic increase in the electron flow predicted by the PIC simulation as shown in figure 6.6.

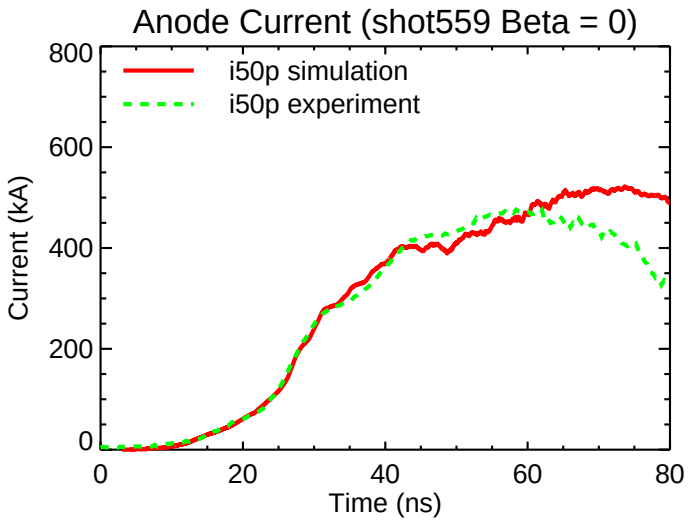

Figure 6.4: Shot 559: Comparison between the experimental and simulated anode currents. Both currents were recorded from the inner radial B-dot probe.

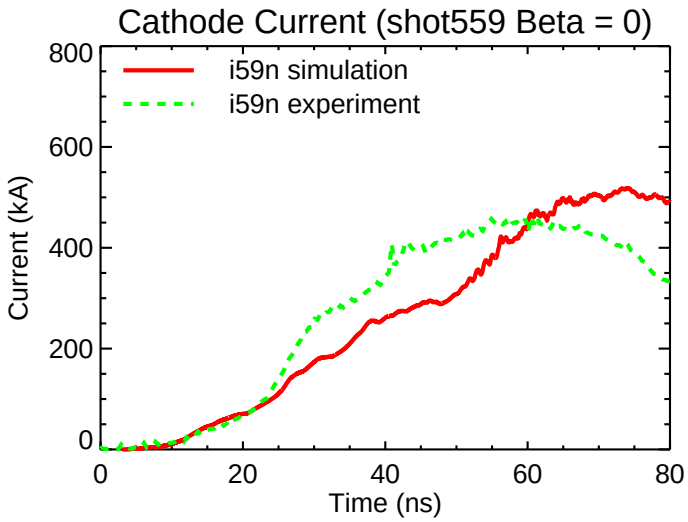

Figure 6.5: Shot 559: Comparison between the experimental and simulated cathode currents. Both currents were recorded from the outer radial B-dot probe.

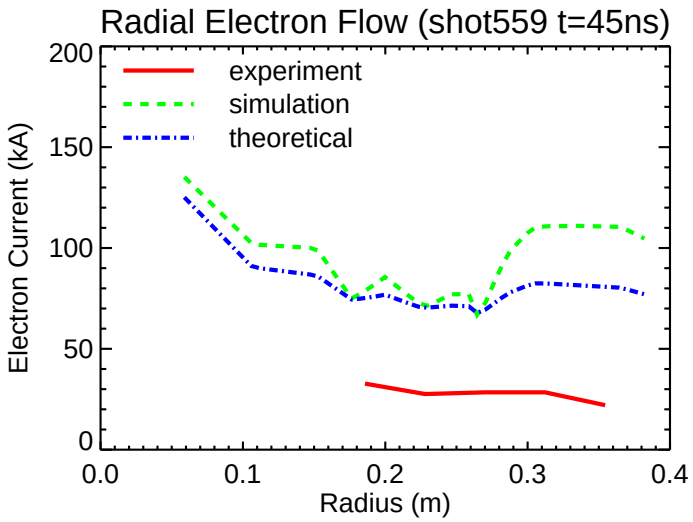

Figure 6.6: Shot 559: Comparison between the experimental and simulated radial electron flow profiles.

Further investigation into the discrepancy between the experimental and simulated cathode currents is quite revealing. The cathode current is equal to the difference between the anode current and the electron drift inside the A-K gap of the MITL. Because the anode currents from the simulation appear to be in close agreement with the experimental data, figure 6.4, this would suggest that the disparity in the electron flow primarily depends upon the behavior of the electrons at the cathode surface. This could either be a result of inadequate modeling of the field emission or additional electron re-trappment that was not accounted for along the cathode surface.

Within the A-K gap of a MITL, excessive electric field strengths result in explosive electron emission from the cathode. As the electrons enter the gap, the vacuum electric field is modified via this introduction of charge. Eventually, this charge density is substantial enough to cancel out the electric field at the cathode surface such that no additional electrons are emitted into the gap. This condition, known as

space-charge-limited emission, is responsible for the regulation of the vacuum charge density. During steady-state operation, electrons are emitted from the cathode to replace charge that has either left the transmission line or has been collected at the anode. If additional electrons are injected into the gap region the opposite occurs; the electric field will be reversed such that electrons are driven back toward the cathode. Because the voltage level for magnetic insulation in this experiment is marginal, as shown through simulation, the anode is subjected to sufficient energy deposition due to electron bombardment resulting in the introduction of additional charge into the gap. This charge could result in electrons being recollected at the cathode thus increasing its current. While the electric field along the cathode in the PIC simulation is allowed to vary due to the field emission algorithm, the electrodynamics, which occur within the MITL's A-K gap, are calculated under the assumption that the cathode is a space-charge-limited-emitter and that the electric field at its surface is always zero. The PIC simulation only considers field emission from a defined surface and does not provide a mechanism for the introduction of additional charge into the system. Thus, the collection of previously emitted electrons by the cathode surface due to electric field reversal does provide an explanation for the larger cathode currents observed in experiment.

The current detected by the CVR in the base of the collector can for shot 559 is given in figure 6.7. This signal was relatively close to the current measured by the B-dot probes but would "turn-off" unexpectedly, early in the pulse, by a mechanism which is not clearly understood. Typically, problems with hardware alignment would result in the shorting of the inner collector can as illustrated in figure 6.13 for shot 562. When the inner can was not shorted it did provide useful information during the initiation of the electron field emission. Using this diagnostic, electrons could be detected slightly earlier than the resolution of the subtraction between the B-dot signals would allow. Because electrons were detected very early in the pulse and great precautions were taken to lower the field emission threshold by coating the

cathode in Aerodag, we are led to believe that the threshold of the field emission is not a concern. We thus assume that electric field reversal at the cathode is primarily responsible for the over estimation of the electron flow by the simulation. A model to test this hypothesis will be developed in section 6.3.

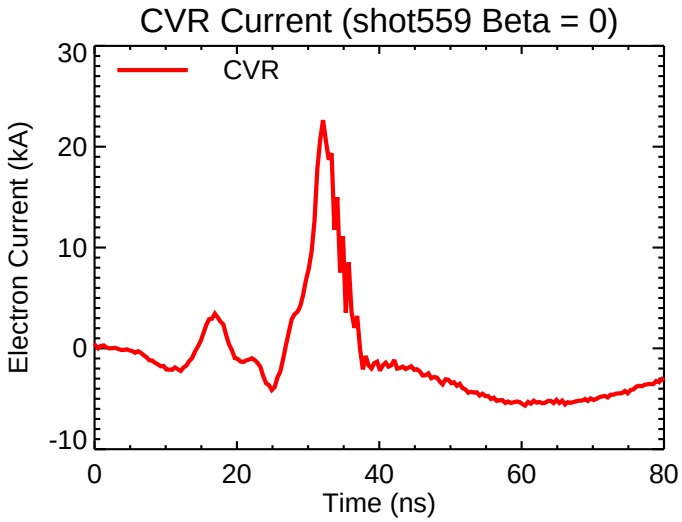

Figure 6.7: Shot 559: CVR signal.

6.2 Reducing electron flow (shot 562)

The reducing electron flow profile used in this experiment defined a re-trapping rate of $\beta \simeq 3.7$ for a load inductance of 50 nH. This was the most aggressive design and provided the greatest possible variation between radially changing flows at comparable voltages. The experimental data for the reducing electron flow profile, shot 562, is given in figures 6.8-6.13. The anode and cathode measurements shown in figure 6.8 are very similar to those recorded in shot 559. The rise-time in shot

562 is slightly longer due to the increased inductance in the line. Microwaves are now more prevalent within the cathode signal, indicating a larger instability of flow resulting in the bunching of electrons. The radial profile of the currents is given in figure 6.9. The time dependent comparisons for the anode and cathode currents are given in figures 6.10 and 6.11 respectively. The situation here is very similar to what was witnessed in the constant flow experiment. The anode currents are in very close agreement, figures 6.9 and 6.10, while the cathode currents clearly deviate. Unlike shot 559, however, the disparity between the experimental and simulated cathode currents appears to increase with radius. Because of the relationship between the electron and cathode currents, this amplified separation is inherited by the radial electron flow profile given in figure 6.12. The CVR signal for this particular shot is given in figure 6.13. Unfortunately, the inner collector can was shorted for this shot as seen from the dramatic negative shift in the CVR signal. This is a result of the total current being dumped through the CVR at the base of the can.

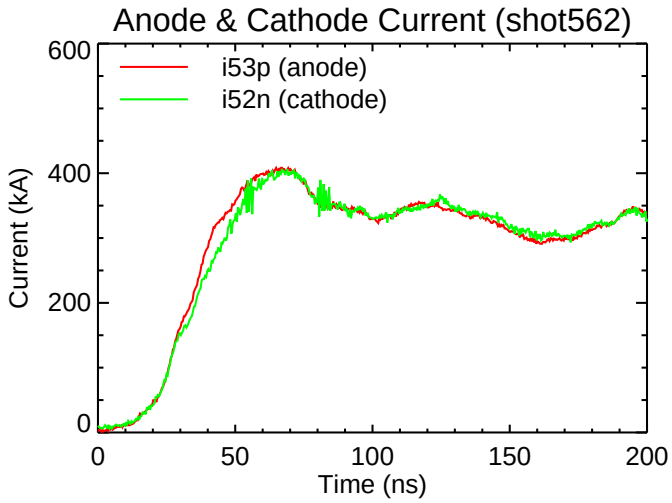

Figure 6.8: Shot 562: Anode and Cathode currents.

The discrepancy between the experimental and simulated electron flow appears to be more complicated in the case of a reducing flow profile. Because a radial electron re-trapping rate is built into the hardware design, the cathode current will increase with a decrease in radius, figure 6.9. If the MITL in the experiment was experiencing field reversal along the cathode surface it would be more noticeable at a larger radius; the larger re-trapping rate near the load effectively reduces the effect of additional electrons entering the A-K gap on the cathode's space-charge-limited-emission. The field reversal would be more evident in the sections of the line where electrons weren't already returning to the cathode.

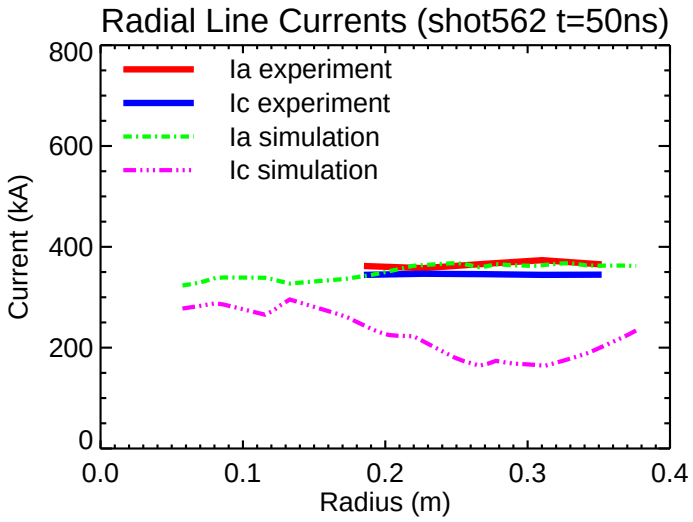

Figure 6.9: Shot 562: Radial profile of anode and cathode currents near the time of peak electron flow.

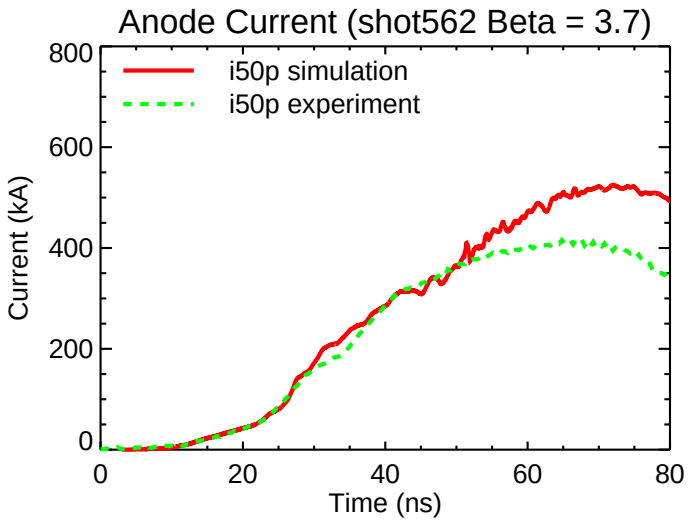

Figure 6.10: Shot 562: Comparison between the experimental and simulated anode currents. Both currents were recorded from the inner radial B-dot probe.

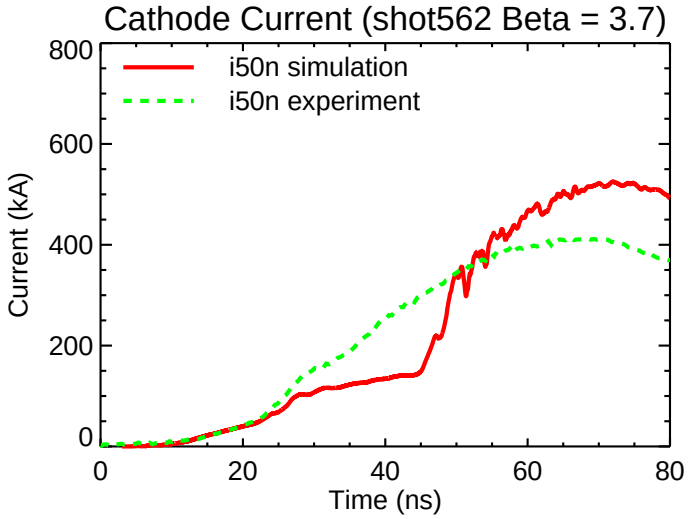

Figure 6.11: Shot 562: Comparison between the experimental and simulated cathode currents. Both currents were recorded from the inner radial B-dot probe.

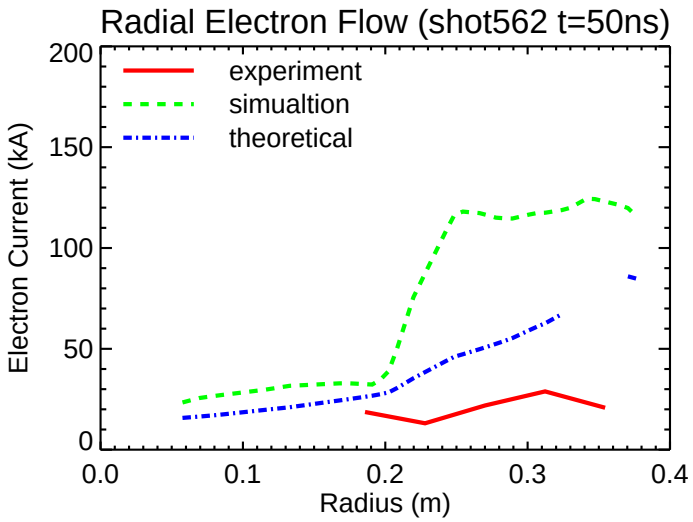

Figure 6.12: Shot 562: Comparison between the experimental and simulated radial electron flow profiles.

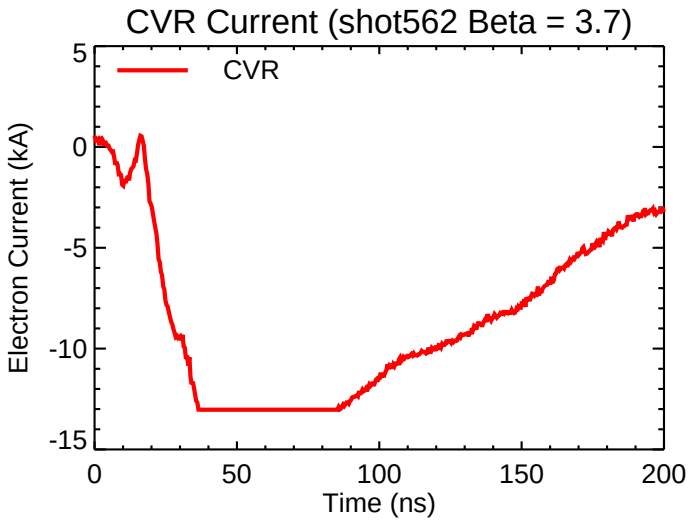

Figure 6.13: Shot 562: CVR signal.

6.3 Flow Impedance Model with Electric Field Reversal at the Cathode

If there is a reversal of the electric field, and thus a negative charge present at the cathode surface, there will be a decrease in the electron current within the MITL. The electric flow impedance, which is defined by the centroid of the charge distribution, on the other hand, does not vary greatly as a result of electric field reversal [57]. As electrons are being lost to the cathode, the centroid position of the remaining charge changes only marginally [13]. It is therefore beneficial to study this situation in terms of the flow impedance which is easily obtained from the simulations.

If we examine the charge profile from the simulated data on shot 559, figure 6.14, we notice an excellent corroboration with the constant axial charge profile predicted by the theoretical model. Using this model, $Z_f = V_a/cQ_a$, and the line voltage provided by the simulation, the flow impedance is found to be $Z_f \simeq 3.07\ \Omega$. It would be expected that this flow impedance for the space-charge-limited-emission case (i.e. $Q_c = 0$) would not deviate significantly from the case of electric field reversal along the cathode (i.e. $Q_c < 0$).

In order to properly examine the situation of field reversal, the theoretical model must be modified to include the possibility of charge existing along the cathode. If we generalize the procedure outlined on page 1336 of reference [13], such that $Q_c \neq 0$, we can define the following charge density profile,

For $0 < G < G_s$,

$$Q(G) = \frac{1}{c}\left(\frac{I_c^2}{mc^2/e}\right) G + Q_c,$$

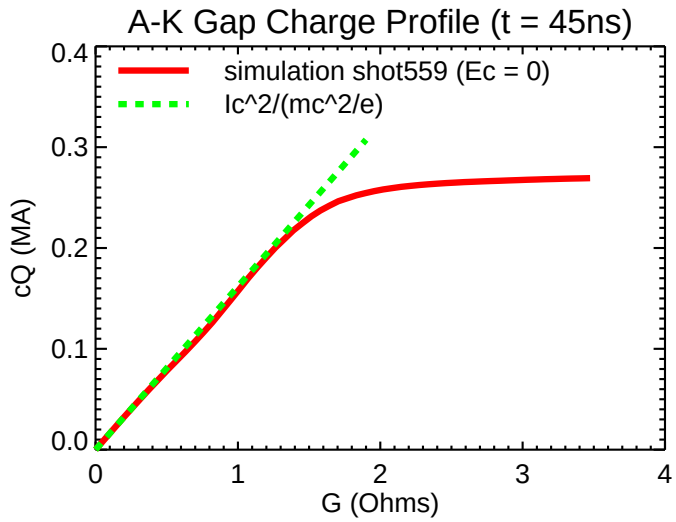

Figure 6.14: Simulation of shot 559. Charge density profile across the A-K gap at $r = 0.18$ m with $I_c = 0.288$ MA.

For $G > G_s$,

$$Q(R) = Q_a,$$

where G_s is determined from $Q(G_s) = Q_a$,

$$G_s = \frac{c(Q_a - Q_c)mc^2}{eI_c^2}.$$

If the charge density profile given above is substituted into the general definition of electric flow impedance, equation 2.40, such that,

$$Z_f = Z_v - \frac{Z_v Q_a - \int_0^{Z_v} Q(G)dG}{Q_a - Q_c}, \tag{6.1}$$

then the flow impedance can be expressed as

$$Z_f = Z_v - \frac{mc^2}{2e}\frac{c(Q_a - Q_c)}{I_c^2}. \tag{6.2}$$

If we assume that a quasi-static balance has been achieved such that the electric and magnetic field pressures, within the A-K gap, do not cause the sheath to expand or retract across the gap spacing, then we can relate the anode and cathode charge densities to their respective line currents,

$$c^2(Q_a^2 - Q_c^2) = I_a^2 - I_c^2. \tag{6.3}$$

Using this equation in conjunction with equation 6.2 allows the charge density along the cathode, Q_c, to be expressed only in terms of the line currents, vacuum impedance, and flow impedance,

$$cQ_c = \frac{c^4 m_e^2 (I_a^2 - I_c^2) - 4e^2 I_c^4 (Z_v - Z_f)^2}{4em_e c^2 I_c^2 (Z_v - Z_f)}. \tag{6.4}$$

Similarly, the equation for the charge per unit length along the anode is given by,

$$cQ_a = \frac{c^4 m_e^2 (I_a^2 - I_c^2) + 4e^2 I_c^4 (Z_v - Z_f)^2}{4em_e c^2 I_c^2 (Z_v - Z_f)}. \tag{6.5}$$

The graph of cQ_c and cQ_a with respect to the flow impedance, Z_f, for shot 559 is given in figure 6.15. The vacuum impedance was calculated from $Z_v = 60g/r$ at the location of the first current monitor and the line currents were taken from the experimental data. The charge per unit length along the cathode surface is

negative, indicating an electric field reversal, for $Z_f \leq 3.93\ \Omega$. A flow impedance greater than this cut-off would result in $Z_f/Z_v > 99\%$, which would indicate a highly insulated system which is not possible with the experimental voltages used. The flow impedance calculated from the simulation data, $Z_f = 3.07\ \Omega$, is well within the range of field reversal. For the electric field to be completely canceled out along the cathode, $Q_c = 0$, there would have to be greater than a 28% change in flow impedance between the simulation and the experiment.

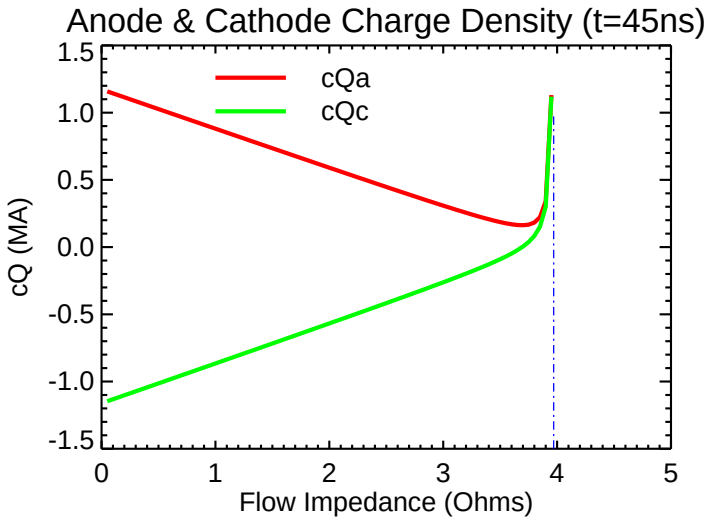

Figure 6.15: Shot559 ($r = 0.185$ m): cQ_a and cQ_c versus flow impedance, Z_f. The experimental line currents are $I_a = 0.421$ MA and $I_c = 0.388$ MA. The vacuum impedance is denoted by the vertically dashed line, $Z_v = 3.97\ \Omega$.

At $Z_f = 3.07\ \Omega$, $c(Q_a - Q_c) = 0.53$ MA. The drift velocity, v_d, is found to be roughly 20% of the speed of light in vacuum. Therefore, the electrons are quickly evacuated from the line at peak electron flow. The electron drift decreases after the peak flow until it finally reaches voltage reversal at $t \simeq 81.5$ ns. The line voltage as a function of the flow impedance is plotted in figure 6.16. Below $Z_f = Z_v/2$ the voltage is negative. The flow impedance predicted by the simulation corresponds with a line voltage of $V_a \simeq 0.67$ MV, which is very close to the peak of the curve.

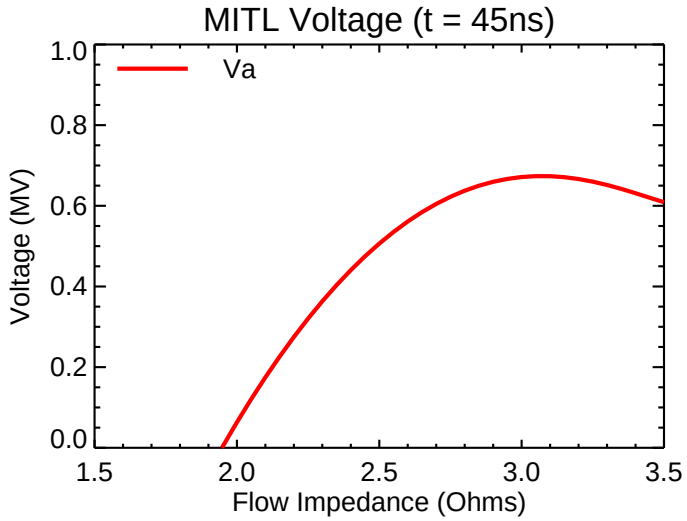

Figure 6.16: Shot559 ($r = 0.185$ m): Line voltage versus flow impedance, Z_f. For this plot, $I_a = 0.421$ MV, $I_c = 0.388$ MA, and $Z_v = 3.97\ \Omega$.

The above analysis also applies to the reducing flow profile used for shot 562. The charge density profile across the MITL's A-K gap is obtained from the simulation's electric field contours and is given in figure 6.17. The theoretically predicted change in the charge per unit length is overlayed against the simulated curve. There appears to be good agreement between the approximately constant change in the charge

density across the gap out to a height of 1.5 mm above the cathode. Because of the very fine meshing used in the simulation, the slight deviation from the theoretical line is most likely due to an increase of turbulence (i.e. vortices) along the line. This increase in turbulence also affects the orbits of the marginally insulated electrons, resulting in a greater number of transitions to the anode. This influences the charge density in the upper 91% of the gap resulting in a gradual increase of charge as opposed to the clearly defined electron sheath edge as seen in shot 559. The electric flow impedance in this case is calculated to be $Z_f \simeq 5.12\ \Omega$. Because the electron sheath is not clearly defined, it is probably more accurate to determine the flow impedance from the position of the charge centroid within the simulation space. In this case the flow impedance is slightly larger and is given by, $Z_f \simeq 5.4\ \Omega$. This corresponds to 88% of the vacuum impedance which is consistent with the lower voltage simulations presented in chapter 5.

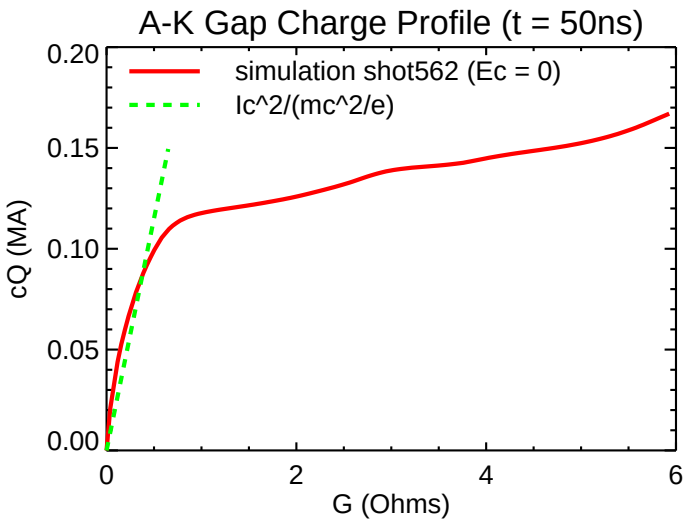

Figure 6.17: Simulation of shot 562. Charge density profile across the A-K gap at $r = 0.18$ m with $I_c = 0.337$ MA.

Because the majority of the charge is located close to the cathode, the flow impedance calculated from the charge centroid will always be less than or equal to the value predicted by the theoretical model. Thus, the model generates the lowest possible flow impedance for the line. Because the time considered here is during peak electron flow (i.e. minimum insulation), the difference between the two measurements should be at a maximum. Later in time, the theoretical value should start to converge toward the flow impedance predicted by the location of the charge centroid. Because the theoretical model was accurate through the majority of the space charge, figure 6.17, it should give a good approximation for the charge density along the cathode.

A plot of the anode and cathode charge density at the location of the inner B-dot probe is given in figure 6.18. The cathode charge density, Q_c, drops below zero for $Z_f \leq 5.83\ \Omega$, which corresponds with 96% of the vacuum impedance. By plotting the charge densities along the anode and cathode versus flow impedance at a larger radius, figure 6.19, we find that the flow impedance model predicts that the amount of negative charge along the cathode is greater towards the load. This makes sense because this model does not account for the additional re-trapping of electrons due to a change in the inductive profile. As these electrons are being returned to the cathode, the model overestimates the amount of negative surface charge at lower radius. The actual charge due to the field reversal is more accurately described at larger radius.

The theoretical line voltage as a function of the flow impedance for shot 562 is plotted in figure 6.20. For $Z_f < Z_v/2$ the voltage is negative. The flow impedance predicted by the simulation corresponds with a line voltage of $V_a \simeq 0.86$ MV. This is significantly higher than the line voltage predicted for shot 559 but is consistent with the lower currents measured experimentally.

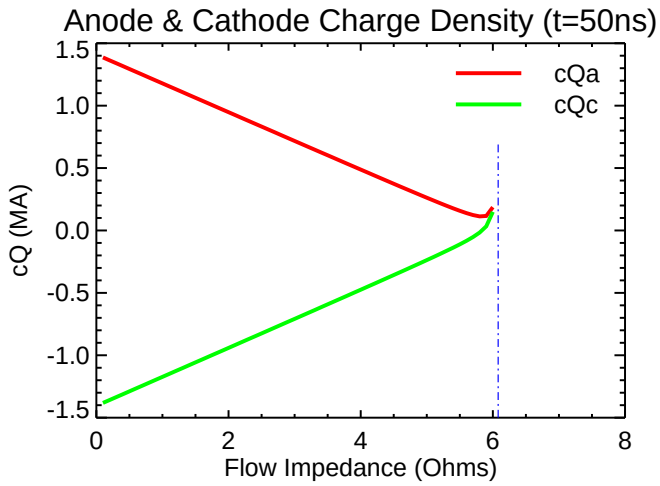

Figure 6.18: Shot562 ($r = 0.185$ m): cQ_a and cQ_c versus flow impedance, Z_f. The experimental line currents are $I_a = 0.362$ MA and $I_c = 0.344$ MA. The vacuum impedance is denoted by the vertically dashed line, $Z_v = 6.08\ \Omega$.

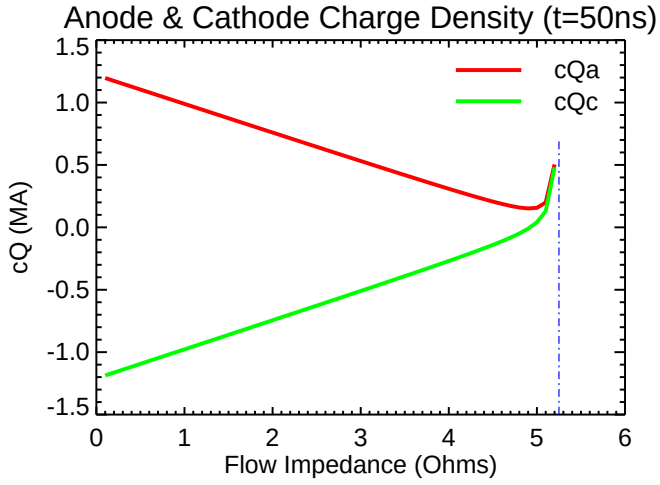

Figure 6.19: Shot562 ($r = 0.298$ m): cQ_a and cQ_c versus flow impedance, Z_f. The experimental line currents are $I_a = 0.365$ MA and $I_c = 0.345$ MA. The vacuum impedance is denoted by the vertically dashed line, $Z_v = 5.25\ \Omega$.

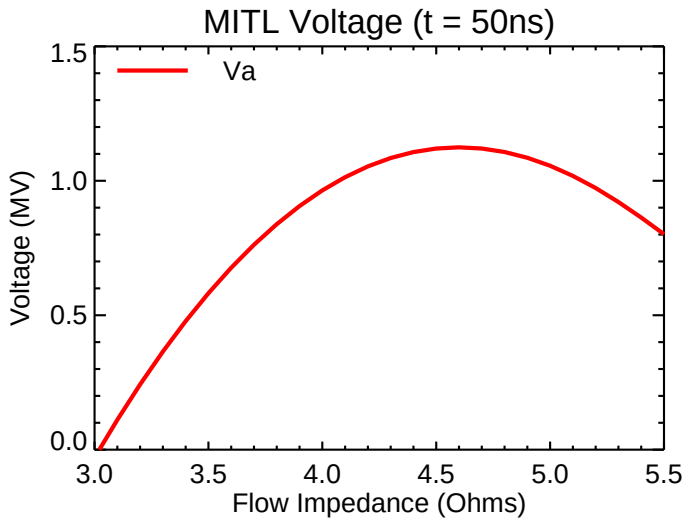

Figure 6.20: Shot562 ($r = 0.185$ m): Line voltage versus flow impedance, Z_f. For this plot, $I_a = 0.365$ MV, $I_c = 0.345$ MA, and $Z_v = 6.08\ \Omega$.

The electron currents measured from shots 559 and 562 are plotted versus radius in figure 6.21. Each shot utilized a unique radial gap profile which resulted in separate voltage and current characteristics. Because the average gap spacing was larger in the reducing flow profile, the voltages were higher due to the increased inductance of the line. It would be expected that this would result in more field emission and thus larger electron currents being measured for shot 562. At larger radius, however, measurements reveal that the differences between the anode and cathode currents were very comparable. This would suggest that a larger number of electrons were being driven back to the cathode within the reducing flow profile. Whether the mechanism for re-trapping the electrons was due to the inductive profile or electric field reversal along the cathode, the radial electron flow for the reducing flow profile is significantly less near the load than the constant flow profile, as was intended.

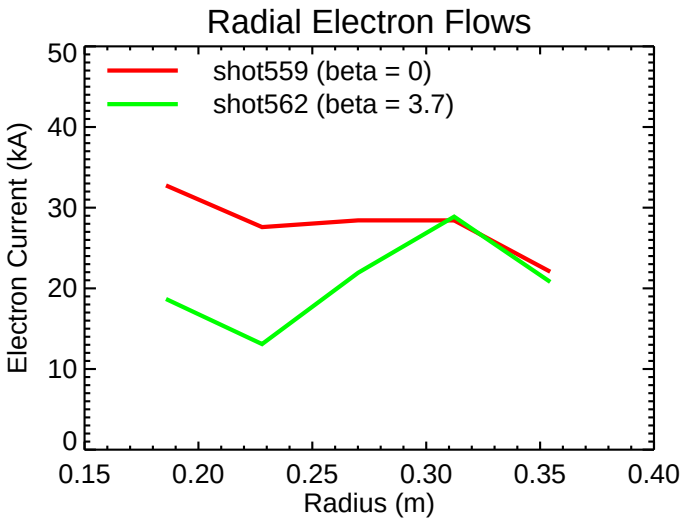

Figure 6.21: Comparison of radial electron flows from experimental shots 559 and 562.

References

[1] W. A. Stygar, R. B. Spielman, G. O. Allshouse, C. Deeney, D. R. Humphreys, H. C. Ives, F. W. Long, T. H. Martin, M. K. Matzen, D. H. McDaniel, C. W. Mendel, L. P. Mix, T. J. Nash, J. W. Poukey, J. J. Ramirez, T. W. L. Sanford, J. F. Seamen, D. B. Seidel, J. W. Smith, D. M. Van De Valde, R. W. Wavrik, P. A. Corcoran, John W. Douglas, I. D. Smith, Michael A. Mostrom, K. W. Struve, Thomas P. Hughes, Robert E. Clark, R. W. Shoup, T. C. Wagoner, T. L. Gilliland, and B. P. Peyton. Design and performance of the Z magnetically-insulated transmission lines. In *Proc. 14th IEEE Pulsed Power Conference, Baltimore, MA*, 1997.

[2] G.A. Mesyats. *Pulsed Power*. Kluwer Academic / Plenum Publishers, 2005.

[3] J.M. Creedon. Relativistic brilloun flow in the high ν/γ diode. *J. Appl. Phys.*, 46:2946–2955, 1975.

[4] C.W. Mendel, D.B. Seidel, and S.E. Rosenthal. A simple theory of magnetic insulation from basic physical principles. *Laser and Part. Beams*, 1:311–320, 1983.

[5] V. I. Sotnikov, R. Presura, B. S. Bauer, and B. V. Oliver. Numerical investigation of plasma evolution in magnetically insulated transmission lines. In *Proc. 14th IEEE Pulsed Power Conference, Dallas, TX*, 2003.

[6] R. W. Stinnett, M. A. Palmer, R. B. Spielman, and R. Bengtson. Small gap experiments in magnetically insulated transmission lines. *IEEE Trans. Plasma Sci.*, PS-11:216–219, 1983.

[7] V. V. Ivanov, P. J. Laca, B. S. Bauer, R. Presura, V. I. Sotnikov, A. L. Astanovitskiy, B. Le Galloudec, J. Glassman, and R. A. Wirtz. Investigation of plasma evolution in a coaxial small-gap magnetically insulated transmission line. *IEEE Trans. Plasma Sci.*, 32:1843–1848, 2004.

[8] P. A. Corcoran, J. W. Douglas, I. D. Smith, P. W. Spence, W. A. Stygar, K. W. Struve, T. H. Martin, R. B. Spielman, and H. C. Ives. PBFA-Z Vacuum section design using TLCODE simulation. In *Proc. 14th IEEE Pulsed Power Conference, Baltimore, MA*, 1997.

[9] T. P. Hughes, R. E. Clark, B. V. Oliver, T. D. Pointon, and W. Stygar. Sheath-current retrapping in the Z MITLs. In *Proc. 14th IEEE Pulsed Power Conference, Dallas, TX*, page 622, 2003.

[10] T. D. Pointon and W. A. Stygar. 3-D PIC Simulations of electron flow in the vacuum power flow section of the Z accelerator. In *Proc. 13th IEEE International Pulsed Power Conference*, page 1696, 2001.

[11] T. D. Pointon and M. E. Savage. 2-D PIC Simulations of electron flow in the magnetically insulated transmission lines of Z and ZR. In *Proc. 15th IEEE International Pulsed Power Conference*, pages 151–154, 2005.

[12] M.E. Savage. Private communication. Sandia National Laboratories LDRD proposal, 2006.

[13] C.W. Mendel and S.E. Rosenthal. Modeling magnetically insulated devices using flow impedance. *Phys. Plasmas*, 2:1332–1342, 1995.

[14] S. Humphries. *Charged Particle Beams*. John Wiley & Sons, 1990.

[15] R. Scarpetti, D. A. Goerz, P. R. Bowen, R. L. Hodgin, K. C. Wong, and P. DD'A. Champney. Electronic emission from conductors subjected to intense short-pulse electric fields. In *IEEE Pulsed Power Conf.*, June 29 - July 1 1987.

[16] R. B. Miller. Mechanism of explosive electron emission for dielectric fiber (velvet) cathodes. *J. Appl. Phys.*, 84:3880–3889, 1998.

[17] R. H. Fowler and L. W. Nordheim. Field emission from metallic surfaces. *Proceedings of the Royal Society A*, 119:173–181, 1928.

[18] G.A. Mesyats and D.I. Proskurovsky. *Pulsed Electrical Discharge in Vacuum*. Springer-Verlag, 1989.

[19] N.S. Xu and R.V. Latham. The application of an energy-selective imaging technique to a study of field-induced hot electrons from broad-area high-voltage electrodes. *Surf-Sci.*, 274:147–160, 1992.

[20] H. Bluhm. *Pulsed Power Systems*. Springer, 2005.

[21] Stephen A. Slutz. Minimum energy principle in magnetic insulation theory. *J. Appl. Phys.*, 61:2087–2089, 1987.

[22] P. F. Ottinger and J. W. Schumer. Rescaling of equilibrium magnetically insulated flow theory based on results from particle-in-cell simulations. *Phys. Plasmas*, 13:063109, June 2006.

[23] J.D. Jackson. *Classical Electrodynamics*. John Wiley & Sons, 1999.

[24] M.E. Savage. *Experimental Studies of Self Magnetically Insulated Relatvistic Flows*. PhD thesis, University of New Mexico, 1989.

[25] R.F. Harrington. *Time-Harmonic Electromagnetic Fields*. McGraw-Hill, 1961.

[26] J.M. Creedon. Magnetic cutoff in high-current diodes. *J. Appl. Phys.*, 48:1070–1077, 1977.

[27] A. Ron, A.A. Mondelli, and N. Rostoker. Equilibria for magnetic insulation. *IEEE Trans. Plasma Sci.*, 1:85–93, 1973.

[28] R.V. Loveless and E. Ott. Theory of magnetic insulation. *Phys. Fluids*, 17:1263, 1974.

[29] K.D. Bergeron. One and two species equilibria for magnetic insulation in coaxial geometry. *Phys. Fluids*, 20:688, 1977.

[30] C.W. Mendel. Planar one-dimensional magnetically insulated electron flow for arbitrary canonical-momentum distribution. *J. Appl. Phys.*, 50:3830, 1979.

[31] P.A. Miller and C.W. Mendel. Analytic model of the applied-B ion diode impedance behavior. *J. Appl. Phys.*, 61:529–539, 1987.

[32] S.E. Rosenthal. Characterization of electron flow in negative- and positive-polarity linear-induction accelerators. *IEEE Trans. Plasma Sci.*, 19:822–830, 1991.

[33] C.W. Mendel and S.E. Rosenthal. Dynamic modeling of magnetically insulated transmission line systems. *Phys. Plasmas*, 3:4207, 1996.

[34] C.W. Mendel and D.B. Seidel. Flow impedance in a uniform magnetically insulated transmission line. *Phys. Plasmas*, 6:4791, 1999.

[35] H.R. Jory and A.W. Trivelpiece. Exact relativistic solution for the one-dimensional diode. *J. Appl. Phys.*, 40:3924, 1969.

[36] J.P. VanDevender. Long self-magnetically insulated power transport experiments. *J. Appl. Phys.*, 50:3928, 1979.

[37] C.W. Mendel, J.A. Swegle, and D.B. Seidel. Stability of magnetically insulated electron flow. *Phys. Rev. A*, 32:1091–1097, 1985.

[38] D. W. Kerst. Acceleration of electrons by magnetic induction. *Phys. Rev.*, 58:841, 1940.

[39] C.W. Mendel, M.E. Savage, D.M. Zagar, W.W. Simpson, T.W. Grasser, and J.P. Quintenz. Experiments on a current-toggled plasma-opening switch. *J. Appl. Phys.*, 71:3731, 1992.

[40] S. Humphries. *Principles of Charged Particle Acceleration*. John Wiley & Sons, 1986.

[41] Matthew N. O. Sadiku. *Numerical Techniques in Electromagnetics*. CRC Press, 2001.

[42] F. H. Harlow. A machine calculation method for hydrodynamic problems. Technical report, Los Alamos Scientific Laboratory, 1956.

[43] Paul M. Bellan. *Fundamentals of Plasma Physics*. Cambridge University Press, 2006.

[44] J. P. Quintenz, D. B. Seidel, M. L Kiefer, T. D. Pointon, R. S. Coats, S. E. Rosenthal, T. A. Mehlhorn, M. P. Desjarlais, and N. A. Krall. Simulation codes for light-ion diode modeling. *Lasers Part. Beams*, 12:283–324, 1994.

[45] Rebecca S. Coats, Mark L. Kiefer, Michael F. Pasik, Timothy D. Pointon, and David B. Seidel. QUICKSILVER User's guide. Technical report, Sandia National Laboratories, July 2002.

[46] L. Paul Mix. PFIDL User's guide: Procedures for the analysis and visualization of data arrays. Technical report, Sanida National Laboratories, January 1996.

[47] Timothy D. Pointon. User's guide for particle models in QUICKSILVER. Technical report, Sandia National Laboratories, July 2002.

[48] Timothy D. Pointon. User's guide for killed particle models in QUICKSILVER. Technical report, Sandia National Laboratories, March 2006.

[49] Timothy D. Pointon. Users guide for QS/ITS coupling models in QUICKSILVER. Technical report, Sandia National Laboratories, July 2006.

[50] A. Thom and C. J. Apelt. *Field Computations in Engineering and Physics*. London: D. Van Nostrand, 1961.

[51] Kane S. Yee. Numerical solution of initial boundary value problems involving maxwell's equations in isotropic media. *IEEE Transactions on Antennas and Propagation*, 14:302, 1966.

[52] D. W. Swain, S. A. Goldstein, L. P. Mix, J. G. Kelly, and G. R. Hadley. The characteristics of a medium current relativistic electron-beam diode. *J. Appl. Phys.*, 48:1085–1093, March 1977.

[53] A. E. Blaugrund, G. Cooperstein, and S. A. Goldstein. Relativistic electron beam pinch formation processes in low impedance diodes. *Phys. Fluids*, 20:1185, 1977.

[54] R. A. Vesey, T. D. Pointon, M. E. Cuneo, T. A. Mehlhorn, J. E. Bailey, D. J. Johnson, and W. A. Stygar. Electron-anode interactions in particle-in-cell simulations of applied-B ion diodes. *Physics of Plasmas*, 6:3369–3387, August 1999.

[55] T. W. L. Sanford, J. A. Halbieib, J. W. Poukey, A. L. Pregenzer, R. C. Pate, C. E. Heath, R. Mock, G. A. Mastin, and D. C. Ghiglia. Measurement of electron energy deposition necessary to form an anode plasma in Ta, Ti, and C for coaxial bremsstrahlung diodes. *J. Appl. Phys*, 66:10–22, July 1989.

[56] A. J. Leadbetter. Anharmonic effects in the thermodynamic properties of solids i. an adiabatic calorimeter for the temperature range 25-500 °C: the heat capcities of Al_2O_3, Al and Pb. *J. Phys. C (Proc. Phys. Soc.)*, 1:1481–1488, 1968.

[57] C.W. Mendel. Private communication. November, 2007.